

# Optical Sampling of High Bit Rate Optical Data Signals

vorgelegt von  
Diplom-Physiker  
Carsten Schmidt-Langhorst  
aus Berlin

Von der Fakultät II - Mathematik und Naturwissenschaften  
der Technischen Universität Berlin  
zur Verleihung des akademischen Grades  
*Doktor der Naturwissenschaften*  
*Dr. rer. nat.*

genehmigte Dissertation

Promotionsausschuss:

Vorsitzender: Prof. Dr. rer. nat. Gebhard von Oppen  
Berichter: Prof. Dr.-Ing. Hans-Joachim Eichler  
Berichter: Prof. Dr. rer. nat. Hans-Georg Weber

Tag der wissenschaftlichen Aussprache: 04. Mai 2004

Berlin 2004  
D 83



# Abstract

The objective of this work was to develop a measurement system which is capable of analyzing optical data signals with high temporal resolution. The particular target was the measurement of eye diagrams of optical data signals at data rates of 160 Gbit/s and above. The aim was to enable the analysis of distortions of such data signals in fiber optic transmission systems using optical eye diagrams.

To reach the goal of high temporal resolution, the optical sampling technique was employed. The optical sampling system is based on five building blocks, namely the clock recovery, clock processing, sampling pulse source, sampling gate and opto/electrical detector. In order to apply the optical sampling system to analyze signal distortions in transmission systems, a complete optical sampling system was developed which includes an optical clock recovery. This is in contrast to most other work in this field. Moreover, the developed system has the highest sampling rate (i.e. the fastest measurement time) achieved in an optical sampling system so far.

Several configurations of the optical sampling system were realized in this work. In particular, different optical sampling gates were investigated since these gates determine the optical bandwidth of the optical sampling system. Two classes of interferometric sampling gates were studied, either based on the nonlinearity of a fiber (nonlinear optical loop mirror (NOLM), Kerr gate) or of a semiconductor optical amplifier (SOA) (gain-transparent ultrafast nonlinear interferometer (GT-UNI)). In this work, the NOLM based optical sampling system yielded the highest temporal resolution of 1.5 ps corresponding to an optical bandwidth of 294 GHz. The GT-UNI based system reached a slightly lower temporal resolution of 1.7 ps corresponding to an optical bandwidth of 257 GHz. The optical bandwidth of the system with the Kerr gate was 210 GHz (2.1 ps), limited by the pulse width of the sampling pulses used in the experiments.

The realized optical sampling system was successfully applied to measure eye diagrams and waveforms of optical data signals at a data rate of 160 Gbit/s and 320 Gbit/s. Before, this was impossible due to the limited bandwidth of conventional electrical sampling systems. The optical sampling system was applied to analyze qualitatively and quantitatively the signal distortions that a 160 Gbit/s optical data signal suffers upon passage through fiber transmission links. For the first time, this was done using eye diagrams that were sampled in the optical domain. As examples of signal distortions, the effect of amplifier noise, the signal degradation due to the nonlinearity of the transmission fiber and the effect of residual chromatic dispersion were investigated in a 160 Gbit/s transmission system. The analysis of the measured eye diagrams was supported by numerical simulations. For the simulations, a split step Fourier algorithm was implemented to solve the nonlinear propagation equation for optical pulses in fibers.

# Zusammenfassung

Das Ziel dieser Arbeit bestand in der Entwicklung eines Messsystems, mit dem optische Datensignale mit hoher zeitlicher Auflösung analysiert werden können. Ein spezielles Ziel war die Messung von Augendiagrammen von optischen Datensignalen bei Datenraten von 160 Gbit/s und darüber hinaus. Ziel war es, die Analyse von Verzerrungen solcher Datensignale in faseroptischen Übertragungstrecken mit Hilfe von optischen Augendiagrammen zu ermöglichen.

Um das Ziel der hohen zeitlichen Auflösung zu erreichen, wurde die optische Abtasttechnik eingesetzt (Optisches Sampling). Das optische Samplingsystem basiert auf den fünf Bausteinen Taktrückgewinnung, Taktverarbeitung, optische Abtast-Pulsquelle, Abtasttor und opto/elektrischer Detektor. Um das System zur Analyse von Verzerrungen in Übertragungssystemen einsetzen zu können, wurde im Gegensatz zu den meisten anderen Arbeiten auf diesem Gebiet ein vollständiges optisches Samplingsystem entwickelt, das eine Taktrückgewinnung enthält. Zusätzlich hat das entwickelte System die höchste Abtastrate (d.h. die kürzeste Messzeit) aller bislang realisierten optischen Samplingsysteme.

Verschiedene Konfigurationen des optischen Samplingsystems wurden im Rahmen dieser Arbeit realisiert. Insbesondere wurden verschiedene optische Abtasttore untersucht, da diese die optische Bandbreite des Samplingsystems bestimmen. Es wurden zwei Klassen von interferometrischen Abtasttoren untersucht, die auf der Nichtlinearität einer Glasfaser (nonlinear optical loop mirror «NOLM», Kerr-Tor) oder eines Halbleiterlaserverstärkers (gain-transparent ultrafast nonlinear interferometer «GT-UNI») beruhen. In der vorliegenden Arbeit zeigte das NOLM-basierte optische Samplingsystem die höchste zeitliche Auflösung mit 1.5 ps. Dies entspricht einer optischen Bandbreite von 294 GHz. Das GT-UNI-basierte System erreichte eine etwas geringere zeitliche Auflösung von 1.7 ps (257 GHz). Die optische Bandbreite des Systems mit dem Kerr-Tor war 210 GHz (begrenzt durch die Pulsbreite der Abtastpulse).

Das optische Samplingsystem wurde erfolgreich eingesetzt, um Augendiagramme und Signalmuster von optischen Datensignalen bei Datenraten von 160 Gbit/s und 320 Gbit/s zu vermessen. Bislang war dies aufgrund der begrenzten Bandbreite konventioneller elektrischer Samplingsysteme nicht möglich. Das optische Samplingsystem wurde verwendet, um qualitativ und quantitativ die Signalverzerrungen von Datensignalen bei einer Datenrate von 160 Gbit/s zu untersuchen. Erstmalig geschah dies unter Verwendung von Augendiagrammen, die im optischen Bereich abgetastet wurden. Als Beispiele für Signalverzerrungen wurden der Einfluss von Verstärkerrauschen, die Verschlechterungen der Datensignale durch die Nichtlinearität der Übertragungsfaser sowie der Einfluss verbleibender chromatischer Dispersion in einem 160 Gbit/s Übertragungssystem untersucht.

Die Auswertung der gemessenen Augendiagramme wurde durch numerische Simulationen unterstützt. Für die Simulationen wurde ein split-step Fourier Algorithmus implementiert, um die nichtlineare Ausbreitungsgleichung für optische Pulse in Glasfasern zu lösen.



# Contents

<b>1</b>	<b>Introduction</b>	<b>1</b>
1.1	Time Resolved Analysis of Optical Signals . . . . .	1
1.2	Principle of Optical Sampling . . . . .	4
1.3	Scientific Background & Motivation for this Work . . . . .	7
<b>2</b>	<b>Fundamentals of Optical Sampling</b>	<b>13</b>
2.1	Description of Optical Sampling Technique . . . . .	13
2.2	Bandwidth of Optical Sampling Technique . . . . .	16
2.3	Construction of the Eye Diagram . . . . .	19
2.4	Evaluation of the Eye Diagram . . . . .	20
2.4.1	Average Properties of the Signal . . . . .	20
2.4.2	Statistical Properties of the Signal . . . . .	22
<b>3</b>	<b>Set-Up of the Optical Sampling System</b>	<b>27</b>
3.1	Sampling Gate . . . . .	27
3.1.1	Gain-Transparent Ultrafast Nonlinear Interferometer . . . . .	29
3.1.2	Nonlinear Optical Loop Mirror . . . . .	35
3.2	Sampling Pulse Source . . . . .	39
3.2.1	Set-up of the TMLL . . . . .	40
3.2.2	Pulse Width and Pulse Compression . . . . .	42
3.2.3	Timing Jitter . . . . .	45
3.2.4	Reduction of Sampling Pulse Repetition Rate . . . . .	47
3.3	Clock Recovery . . . . .	49
3.3.1	Electrical Clock Extraction . . . . .	49
3.3.2	Optical Clock Recovery . . . . .	49
3.4	Clock Processing . . . . .	53
3.4.1	Frequency Shifting . . . . .	54
3.4.2	Frequency Dividers . . . . .	58
3.4.3	Random Optical Sampling . . . . .	58
3.5	Sample Detection . . . . .	59
<b>4</b>	<b>Characterization of the Optical Sampling System</b>	<b>61</b>
4.1	GT-UNI Based System . . . . .	61
4.1.1	Temporal Resolution . . . . .	61
4.1.2	Linearity . . . . .	64
4.1.3	Wavelength Range . . . . .	65

4.2	NOLM Based System . . . . .	67
4.2.1	Temporal Resolution . . . . .	67
4.2.2	Linearity . . . . .	68
4.2.3	Wavelength Range . . . . .	68
<b>5</b>	<b>Applications of the Optical Sampling System</b>	<b>71</b>
5.1	Waveform Measurements . . . . .	71
5.1.1	NOLM Based System . . . . .	71
5.2	Eye Diagram Measurements . . . . .	73
5.2.1	NOLM Based System . . . . .	73
5.2.2	GT-UNI Based System . . . . .	75
5.2.3	Random Sampling System . . . . .	78
5.2.4	Conclusion of Eye Diagram Measurements . . . . .	82
5.3	160 Gbit/s Transmission Experiments . . . . .	82
5.3.1	Signal-to-Noise Ratio . . . . .	82
5.3.2	Fiber Nonlinearity . . . . .	86
5.3.3	Residual Dispersion . . . . .	94
<b>6</b>	<b>Summary and Conclusion</b>	<b>103</b>
	<b>Bibliography</b>	<b>107</b>
<b>A</b>	<b>Appendix</b>	<b>117</b>
A.1	Set-up of the Optical Transmitter . . . . .	117
A.2	Numerical Simulation of Pulse Propagation in an Optical Fiber . . . . .	119
<b>B</b>	<b>List of Symbols and Abbreviations</b>	<b>123</b>
<b>C</b>	<b>Publications by the Author</b>	<b>129</b>
<b>D</b>	<b>Acknowledgements</b>	<b>135</b>
<b>E</b>	<b>Curriculum Vitae</b>	<b>137</b>

# Chapter 1

## Introduction

### 1.1 Time Resolved Analysis of Optical Signals

Today, ultrashort laser pulses with durations of less than  $10^{-13}$  seconds or 100 fs are generated routinely using commercially available pulse lasers. Researchers even have generated pulses as short as a few fs, which included only a few cycles of the optical wave. Short pulses have many applications in physics, chemistry, biology, and engineering. One special application is to use short optical pulses in optical communication systems. Here, they can be used either to transmit information over optical fibers or to control fast optical gates that perform processing functions in the optical network [1]. If the optical pulses are used to transmit information in a fiber optic communication system, an optical bit stream (optical data signal) is formed by concatenation of a number of optical pulses. Each pulse then represents one data bit.

An optical pulse can be described in the time domain by its complex electrical field:

$$E(t) = \sqrt{\eta P(t)} \exp(i\omega_0 t - i\phi(t)) \quad (1.1)$$

Here,  $P(t)$  is the optical power of the pulse as a function of time and  $\phi(t)$  is the optical phase of the pulse as a function of time.  $\eta$  is a proportionality coefficient that relates the optical power to the electrical field.  $\omega_0$  is the angular frequency of the electric field. The time  $t$  is measured in a time frame moving at the group velocity of the pulse (retarded time). The spatial distribution of the pulse perpendicular to its propagation direction as well as the polarization of the pulse are neglected. From Eq. (1.1) it is clear that in this simplified description an optical pulse is fully characterized if its power and phase are known as a function of time.

A number of techniques exist that allow to characterize short optical pulses. Most of the techniques allow to measure the optical power as a function of time. Some techniques additionally allow to measure the optical phase as a function of time. However, in a fiber optic communication system, the target is not only to characterize the optical pulse itself, but rather the optical bit stream.

One way to characterize short optical pulses is to use a streak camera. This instrument is applicable at pulse widths to about 2 ps (e.g. [2]). The main drawback of this technique however is, that it does not provide statistical information about

the optical data signal. The same holds true for autocorrelation or cross-correlation measurements. These are techniques that extend the measurement range to pulse widths below 100 fs (e.g. [3]) and are commonly used to measure  $P(t)$  of pulses including the shortest pulses ever generated.

In order to characterize an optical data signal, the commonly used method is to detect it with a photodetector and then measure the temporal variation of the generated photocurrent as a function of time using an oscilloscope. The shortest pulse width that can be measured using this technique is limited by the response time of the photodetector and the bandwidth of the oscilloscope. Using an electrical sampling oscilloscope and the fastest photodetectors available today, the overall bandwidth of such measurement system is about 65-70 GHz (e.g. [4,5,6]). This bandwidth allows to measure  $P(t)$  of data signals with optical pulses down to a pulse width of about 7 ps.

The bandwidth of this "conventional" sampling technique (photodetector + electrical sampling) can be extended by moving the actual sampling process from the electrical to the optical domain. This technique is called "optical sampling". In an optical sampling system, the optical signal is not converted to an electrical signal first using a fast photodetector and then sampled in the electrical domain. Instead, the optical signal is sampled in the optical domain by an optical sampling gate and afterwards the resulting samples are converted to an electrical signal and detected. In this case the need for high bandwidth electronics is circumvented and the optical bandwidth of the measurement instrument is only limited by the optical sampling gate used.

The **objective of this this work** was to develop a complete optical sampling system, that is capable of analyzing optical data signals with a temporal resolution of less than 5 ps. The target was to enable the measurement of optical eye diagrams (for the definition of the eye diagram see later in this section) in fiber optic communication systems at data rates of 160 Gbit/s and above. The aim was to analyze the distortions of such data signals using optical eye diagrams. In order to apply the optical sampling system to analyze distortions in transmission systems, a complete optical sampling system was developed in this work which includes an optical clock recovery. This is in contrast to most other work in this field. Moreover, the developed system has the highest sampling rate (i.e. the fastest measurement time) achieved in an optical sampling system so far. The optical sampling system allowed the time resolved measurement of the optical power  $P(t)$  as well as a statistical analysis of the optical data signal.

## Data rates in optical communication networks

In optical communication networks the optical fiber is used as transport medium mainly because of its large bandwidth and low loss. There exist two approaches to exploit the large bandwidth of an optical fiber, namely wavelength division multiplexing (WDM) and time division multiplexing (TDM) [1]. Both schemes rely on multiplexing a number of  $d$  individual data channels (sub rate channels), each having a bit rate  $R$ , to a single data stream with the aggregate data rate of  $d \cdot R$ . In WDM systems, each sub rate channel is assigned to a separate wavelength. The spacing of

the wavelengths (wavelength grid) is standardized [7] and is typically 50 or 100 GHz depending on the data rate  $R$  in each wavelength channel. Due to the close spacing of the wavelength channels, the bandwidth in each wavelength channel is rather low ( $< 50$  GHz) and conventional measurement techniques like fast photodetectors in combination with electrical sampling oscilloscopes provide sufficient detection bandwidth.

In TDM systems in contrast, all sub rate channels have the same wavelength but they are multiplexed in the time domain by bitwise interleaving. Consequently, the duration of one bit slot in the aggregate data stream becomes  $T_{bit}/d$  if the duration of one bit slot of the sub rate channel was  $T_{bit} = 1/R$ . Therefore, the bandwidth requirement of the aggregate data channel increases. It is expected that a combination of both TDM and WDM technology will yield the maximum capacity in a fiber transmission system.

Today, optical transmission systems carrying a TDM data rate of 10 Gbit/s per wavelength channel and having up to 128 wavelength channels are commercially available and deployed in the field. At the same time, scientists have already demonstrated single channel, single polarization TDM transmission experiments at data rates up to 640 Gbit/s in a laboratory environment [8,9]. While systems with TDM data rates of 40 Gbit/s are commercially available today, the next evolutionary step will be a TDM data rate of 160 Gbit/s [10]. This is the research activity of a number of laboratories over the world (for an overview see e.g. [11,12]). However, already at a data rate of 160 Gbit/s, conventional measurement techniques do not provide sufficient bandwidth to analyze the data signals.

### Definition of the eye diagram

In general, the most distinct information about the signal quality is given by the signal's bit-error rate (BER). However, there are two drawbacks involved: The bit-error rate cannot be measured on live traffic since the transmitted information is not a priori known. Secondly, in case of a bad BER it is hard to derive any information on the source of the impairment that has caused the BER decrease.

Especially for the optimization of high bit rate transmission links or for debugging in an optical network, a more comprehensive information about the optical data signal is needed. Parameters of the data signal like timing, noise, waveform, power etc. are of interest in that case. All this information can be derived from the so called "eye diagram" of the data signal. An eye diagram is constructed from a data signal as illustrated in Fig.1.1. The figure shows two types of optical data signals that both contain the same logical information as indicated by the "1"'s and "0"'s. In both signals, a logical "1" or "mark" bit is represented by a high optical power, while a logical "0" or "space" bit is represented by a low optical power. In the case shown in the upper part of the figure, the signal power between two consecutive mark bits is kept high while in the lower case the signal power drops to zero in between every two logical bits. Therefore, the lower data format is called "return-to-zero" (RZ) data format, while the upper format is called "non-return-to-zero" (NRZ) data format.

Regardless of the data format, in each optical data signal a logical bit is transmitted within one so called "bit slot". The bit slots are indicated in Fig. 1.1 by the vertical

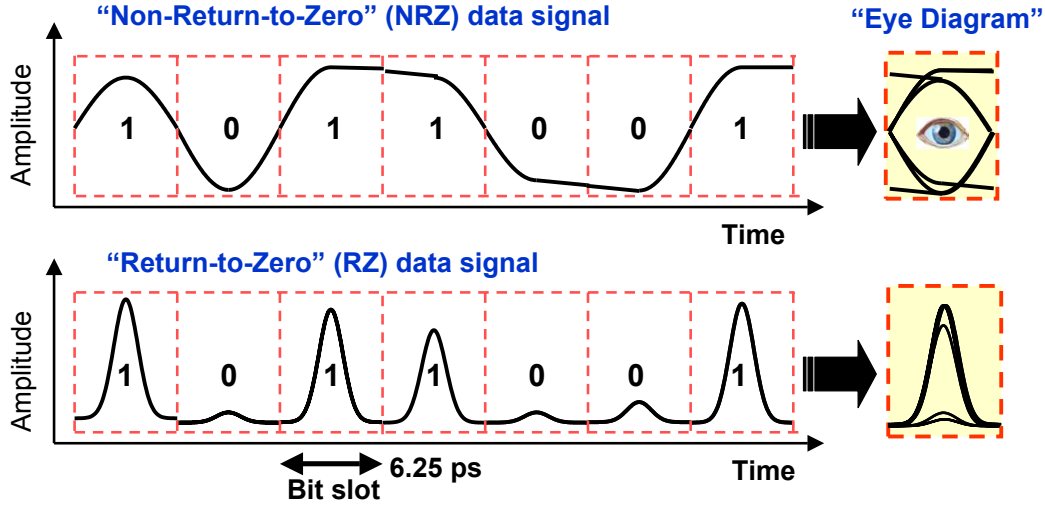


Figure 1.1: Construction of an eye diagram from an NRZ and RZ data signal.

dashed bars. The duration of the bit slot is the bit period  $T_{bit} = 1/R$ , where  $R$  is the data rate of the signal. If the amplitude of the data signal is recorded as a function of time and all recorded amplitude values are plotted as a function of the temporal position within the bit slot, the aggregate diagram shown on the right hand side is obtained. Since in the NRZ case the resulting diagram has the shape of a human eye, such diagram is referred to as an "eye diagram".

From Fig. 1.1 it is evident that the measurement equipment for recording an eye diagram must have a sufficiently large optical bandwidth so that the amplitude variation of the data signal is resolved. For the data rate of  $R = 160$  Gbit/s, corresponding to a bit duration of  $T_{bit} = 6.25$  ps, the flanks of the optical signal have rise and fall times on the order of 2-3 ps.

## 1.2 Principle of Optical Sampling

As discussed before, the optical sampling technique enables an extension of the detection bandwidth of optical data signals by strobing the signal under investigation by an ultrafast optical gate. Fig. 1.2 shows the principle of operation. The upper part shows an optical data signal. In general, the optical sampling technique allows to visualize the eye diagram of any data signal that has been encoded using an amplitude modulation format. In the case of a phase modulation format, it will not be possible to distinguish between logical mark and space levels in the eye diagram. The modulation format of the data signal is RZ in this example. The data signal is a concatenation of optical data bits, each within a bit slot of 6.25 ps corresponding to a data rate of 160 Gbit/s in this example.

This optical data signal is passed through an optical gate. The gate is closed by default, i.e. does not transmit the data signal for most of the time except for ultra short periods of time. The period of time for which the gate transmits the data signal

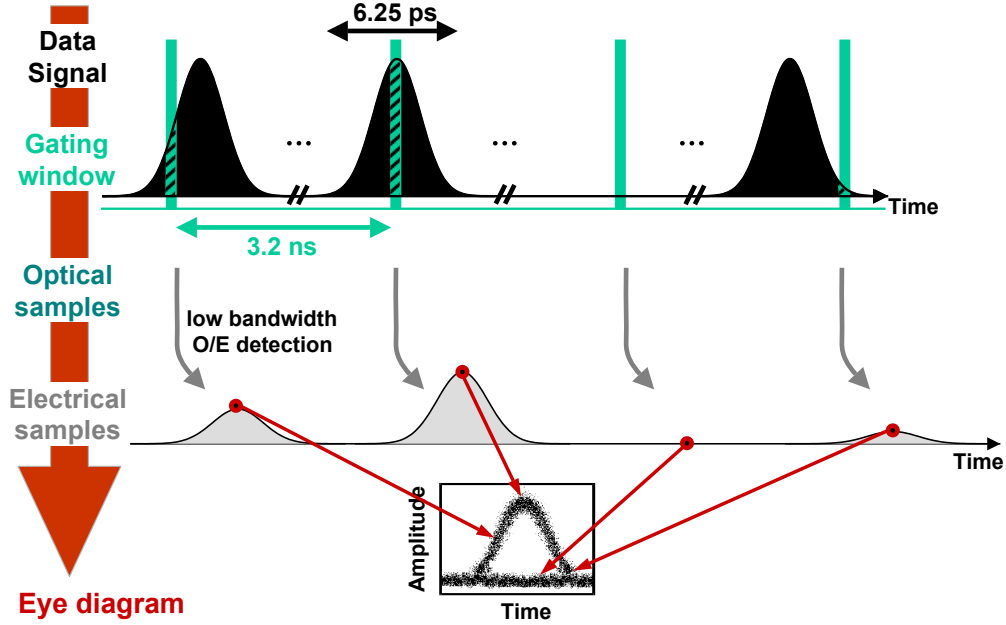


Figure 1.2: Principle of operation of the optical sampling technology.

is called "gating window". If the width of the gating window is shorter than the bit duration as shown in Fig. 1.2, only a fraction of the optical data bit will be sliced out. This fraction is called "optical sample". The optical sample is related to the instantaneous amplitude of the data bit at the sampling time. Ideally, the sampling gate should exhibit a linear transfer function making the amplitude of the optical sample directly proportional to the instantaneous power of the optical data bit.

In order to avoid high speed electronic signal processing for the detection of the optical samples, it is useful to operate the sampling gate with a modest repetition frequency. In Fig. 1.2, the time between two sampling instants was chosen to be 3.2 ns, which corresponds to a sampling frequency of roughly 310 MHz. This frequency is significantly lower (by a factor of 512) than the data rate and thus the sampling process occurs only for every 512th optical data bit. This allows to detect the optical samples with a low bandwidth opto/electrical (O/E) detector. At the output of the detector, the "electrical" sample appears broadened in time due to the low bandwidth of the detector, but still generates a photocurrent that is proportional to the instantaneous optical power of the optical data bit at the sampling time. After a transimpedance amplifier, the peak voltage  $V_p$  of each electrical sample is measured by an analog/digital converter.

The eye diagram of the optical data signal is obtained from the measured  $V_p$ -values if the corresponding sampling times are known. A number of techniques have been proposed to gain this timing information. The commonly used technique is to open the sampling gate synchronous to the optical data signal but with a fixed frequency offset in order to scan over the complete bit slot. Thus a technique for the synchronization of the sampling gate to the optical data signal under investigation is needed. This



function is performed by a clock recovery. The reference signal for such clock recovery is the optical data signal with a bit rate of 160 Gbit/s. Therefore, an all-optical clock recovery had to be developed in this work to extract the electrical clock signal from the optical data signal. A clock processing circuitry is then needed to generate the required frequency offset of the gating window. It provides the timing information for the reconstruction of the eye diagram [13]. This technique was used in the present work. In another approach, the clock processing is omitted and the sampling process is performed at random times [14]. In this case, the sampling times are derived from an arrival time measurement of the sampling pulses themselves. In a third approach, the clock processing unit as well as the clock recovery unit are both omitted and the timing information is reconstructed from the measured sampling data using a special software algorithm [15, 16].

Fig. 1.3 shows the general block diagram of an optical sampling system providing the processing steps depicted in Fig. 1.2. This is also the block diagram of the experimental set-up developed in this work. The optical data signal was tapped from the

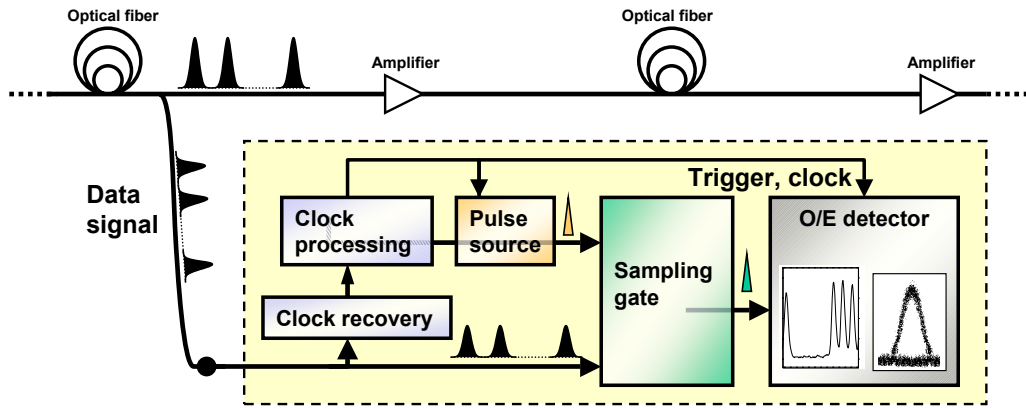


Figure 1.3: Block diagram of a complete optical sampling system.

transmission link and fed into the optical sampling system. Inside the sampling system, part of the signal was used for clock recovery while most of the signal was directly fed to the optical gate (sampling gate). In the clock recovery, an electrical frequency synchronous to the optical data signal was recovered. This recovered clock frequency was then further processed in the clock processing unit. Here, the frequency offset needed to scan the data signal as well as the timing information for the O/E detector were generated. The clock processing unit was used to drive an optical sampling pulse source which emitted short optical pulses (picosecond width). These sampling pulses controlled the optical sampling gate. The optical samples were finally detected by the O/E detector unit and processed by a personal computer.

In general, the optical sampling system displayed the eye diagram of the optical signal under investigation. However under certain circumstances it was also possible to measure the waveform of the optical data signal. This was the case when the data signal was repeating with the extracted clock frequency after the clock recovery, i.e. when the data signal was repeating every 100 ps while the recovered clock frequency



was 10 GHz.

## 1.3 Scientific Background & Motivation for this Work

In this section, the scientific background in the field of optical sampling is reviewed and the motivation for the solutions applied in the present work are given. Finally the structure of the presented work is outlined.

In the literature, the term "optical sampling" is used for a variety of experiments where optical signals are sampled by means of optical or even electrical gates. This section however covers only systems which allow to measure eye diagrams of optical data signals.

Early scientific publications in this field date back to the mid 1990's, when the first optically sampled eye diagrams of 10 Gbit/s optical data signals were published. Since then, there has been growing interest in the optical sampling technique, mainly driven by the increase of data rates in the past 10 years. In the last decade, about 40 publications have been published with a variety of experimental set-up's to achieve high resolution optical sampling. Just recently, the eye diagram of a 640 Gbit/s data signal was successfully measured by an optical sampling system [17].

Fig. 1.4 summarizes the different techniques that have been used in the individual building blocks of optical sampling experiments so far. The O/E detector block is omitted in this overview since it was almost identical in all experiments reported.

**Clock Recovery:** Although a complete optical sampling system requires a clock recovery to synchronize the sampling pulse source to the optical data signal under investigation, it can be seen from Fig. 1.4 that only few realizations of all optical clock recoveries have been demonstrated so far. In most experiments reported, no clock recovery was present and the synchronization signal was directly tapped at the transmitter. These systems are thus only useful in a laboratory environment.

The most important parameter regarding the clock recovery is the timing jitter and the stability of the recovered clock signal. Since the sampling pulse source is synchronized to the recovered clock signal, the jitter of the recovered clock signal should be as low as possible to achieve an overall low jitter sampling system.

All reported clock recovery configurations were based on semiconductor components. Injection locking of a semiconductor mode-locked laser diode (MLLD) was reported at a data rate of 80 and 160 Gb/s [18, 19, 20]. This configuration, however, suffers from stability issues since injection locking is performed at a subharmonic of the MLLD repetition frequency. This leads to the well known "channel hopping" of the recovered clock signal.

A more stable clock recovery can be achieved if feedback loops are used. Therefore, in the work presented here, an optical clock recovery based on an all-optical phase-locked loop (PLL) was developed. The optical phase comparator comprised a semiconductor optical amplifier (SOA) in a Sagnac fiber loop (SLALOM). It was operated at a data rate of 160 Gb/s [13] and showed stable operation with low timing jitter.

Optical Sampling System			
	Clock Recovery	Sampling Pulse Source	Sampling Gate
Semiconductors	<ul style="list-style-type: none"><li>• Injection locked MLLD</li><li>• Optical PLL with SLALOM</li><li>• Electro-optical PLL with EAM</li></ul>	<ul style="list-style-type: none"><li>• TMLL</li><li>• Gain-switched DFB laser</li><li>• cw DFB laser + cascaded EAM's</li></ul>	<ul style="list-style-type: none"><li>• EAM</li><li>• UNI</li><li>• GT-UNI</li><li>• FWM in SOA</li></ul>
		<ul style="list-style-type: none"><li>• Mode-locked EDFL</li></ul>	<ul style="list-style-type: none"><li>• FWM</li><li>• NOLM</li><li>• Kerr gate</li><li>• Parametric amplific.</li><li>• XPM induced wavelength shifting</li></ul>
			<ul style="list-style-type: none"><li>• SFG in KTP, AANP, PPLN</li><li>• DFG in PPLN</li></ul>

Figure 1.4: Overview of the different techniques used in all optical sampling experiments. The grey boxes indicate the techniques that were applied in the present work. The abbreviations are explained in the text.

Finally, an electroabsorption modulator (EAM) was also used in a PLL configuration [21] to measure eye diagrams at a data rate of 160 Gb/s [22].

**Sampling Pulse Source:** Regarding the sampling pulse source, the most important parameters are the timing jitter and the pulse width. The timing jitter determines the timing jitter of the whole sampling system whereas the pulse width limits the temporal resolution of the sampling system. As a rough estimate, a timing jitter of less than 300 fs and a pulse width of about 1 ps is necessary to measure a 160 Gb/s optical eye diagram. Another important parameter is the repetition frequency of the pulse source. Since the O/E detection in the optical sampling systems is typically limited to a few hundred MHz, the sampling pulse rate must not be higher than this frequency. Therefore either sources with low repetition frequency must be used or the repetition frequency must be reduced externally, for instance by gating the pulse train.

In order to generate short pulses at the needed MHz-repetition rates, early reported sampling systems used directly modulated, gain-switched laser diodes (distributed feedback lasers, DFB). [23, 24, 25, 26, 27]. These pulse sources however produced a rather large timing jitter. Therefore, they needed extra stabilization circuitry by

means of optical holding beams. In addition, the generated pulses were rather broad (5-10 ps) so that an additional nonlinear pulse compression was necessary before using them as sampling pulses.

The jitter issue was relieved by driving the DFB lasers in continuous wave mode (cw) and by using cascaded electroabsorption modulators (EAM's) to carve sampling pulses out of this cw signal with the desired repetition frequency [28]. However, due to the limited bandwidth of the available EAM's, the generated pulses were still 12 ps wide, so they had to be compressed in special dispersion decreasing fibers before being useful as sampling pulses. This process required high optical powers which made this configuration unattractive.

Mode-locked Erbium doped fiber lasers (EDFL) became the most widely used sampling pulse sources. They had been developed as pulse sources for 10 Gbit/s based high speed optical laboratory transmitters and exhibited sufficiently low jitter. However, as the lasers were operated at a repetition frequency of 10 GHz, the pulse repetition frequency had to be externally reduced to a few hundred MHz by gating the pulse train with a Lithiumniobate ( $\text{LiNbO}_3$ ) modulator. Such a set-up has been used for example in [29, 30, 31, 32]. These lasers also suffered from a low long term stability as they were operated at a high harmonic of the fundamental resonator mode. Since a low repetition frequency was required anyhow, it was therefore reasonable to operate such lasers directly on their fundamental resonator mode. This has been shown in [33, 34, 35, 17] using a mode-locked Erbium doped fiber laser with 50 MHz repetition rate. However, it is difficult to synchronize a pulse source operating at a low repetition frequency to a reference clock signal at a high frequency with femtosecond timing jitter.

In the work presented here, a passively mode-locked Erbium doped fiber laser (EDFL) with a repetition frequency of 48 MHz was used for some experiments. By using a special sampling set-up (random sampling system, see Sec. 3.4.3), no synchronization of the laser was required.

Most experiments in this work were however performed using a hybridly mode-locked semiconductor laser diode (TMLL). It was operating at a fundamental resonator mode repetition rate of 10 GHz. This pulse source had shown a good long term stability in 160 Gbit/s transmission experiments and has the potential of timing jitter values below 100 fs. Besides it is a compact device and offers the potential of monolithic integration. To accommodate for the low repetition frequency for gating in the optical sampling system, the pulse repetition frequency of the laser was externally reduced to 311 MHz by the use of a  $\text{LiNbO}_3$  amplitude modulator. In this work, two lasers with different emission wavelengths were used. Pulse source #1 had an emission wavelength around 1300 nm [36, 37, 38] while pulse source #2 had an emission wavelength around 1550 nm [13].

A similar type of mode-locked semiconductor laser was also used in [39, 19, 18, 20]. This pulse source however had a fundamental repetition rate of 620 MHz and was directly used without further repetition rate reduction.

**Sampling Gate:** The sampling gate is the central building block of the optical sampling system. Its short gating window enables the high temporal resolution that is needed to measure optical eye diagrams at data rates above 80 Gbit/s, which is

presently the limit of electronic signal processing.

Almost all optical sampling experiments reported so far have used nonlinear optical effects for optical gating. It should be mentioned though that also one linear optical approach was shown [40]. This technique however relied on coherent signal detection and is thus rather wavelength selective since the wavelength of the sampling pulse source must match the wavelength of the data signal under investigation.

The nonlinear optical gates can be classified by the type of process that is used. Among the processes that use the second-order susceptibility  $\chi^{(2)}$  are sum frequency generation (SFG) and difference frequency generation (DFG) in crystals. Examples for processes that use the third-order susceptibility  $\chi^{(3)}$  are four-wave mixing (FWM), cross-phase modulation (XPM), and parametric amplification in fibers. A second classification of the optical gates is by the nonlinear material that is used. This approach was taken in Fig. 1.4.

The most commonly used technique for optical gating in sampling experiments is sum frequency generation (SFG) in nonlinear crystals. These can either be KTP [29, 28, 35] or AANP (being an organic crystal) [30] or periodically poled Lithiumniobate (PPLN) [25, 27, 33, 17]. While these gates provide very short optical gating windows (<1 ps), their main drawback is the required high peak power that is necessary to generate a sufficient amplitude of the frequency converted signal.

Lower optical power requirements for gating are expected from the use of the enhanced resonant nonlinearity of semiconductor optical amplifiers (SOA's). While FWM in SOA's [39, 19] yielded short gating windows comparable to the crystal based gates, the FWM conversion efficiency was still rather low and together with the amplified spontaneous emission (ASE) of the SOA limited the performance of such gates. The switching efficiency can be increased in interferometric configurations where a nonlinear phase change is induced by XPM, which is converted to an amplitude change by the interferometer. A promising type of gate is the so called "ultrafast nonlinear interferometer" (UNI) which was used in [41]. This gate however still suffered from the amplified spontaneous emission (ASE) of the SOA so that an additional EAM with sophisticated synchronization and driving electronics was needed to suppress the ASE after the UNI gate.

The motivation of the work presented here was to combine the superior gating performance of interferometric optical gates with a recently developed operation scheme of an SOA, which is called "gain-transparent" (GT) operation. In this scheme, the data signal is outside the gain bandwidth of the semiconductor material and thus does not suffer from ASE degradation. This configuration was used in the GT-UNI sampling gate [36, 37, 38] in this work.

The third class of nonlinear materials are optical fibers. Recent progress in fiber manufacturing technology allowed to produce special highly nonlinear fibers (HNLF) that have an enhanced nonlinearity coefficient. This reduced the required fiber length for optical switching and made those fibers very attractive, especially since the ultrafast Kerr nonlinearity of the fiber provides short gating windows comparable to the crystal based gates. The exploited nonlinear processes included four-wave mixing [20], parametric amplification [31] and cross-phase modulation induced wavelength shifting [32]. As the conversion efficiency of these processes is rather small, high peak powers are needed to achieve sufficient converted signal power.

In this work two interferometric gates based on highly nonlinear fibers with two types of interferometers were used. One was the nonlinear optical loop mirror (NOLM) [13] while the other one was a so called "Kerr gate".

For the sake of completeness it should be also mentioned that even electroabsorption modulators have been used recently as sampling gates in optical sampling experiments. However, the term "optical sampling" is a little misleading in this case. These systems should rather be referred to as "electro-optical" sampling systems. Since the gating window width that can be achieved with an EAM is comparably large (about 5 ps), these gates could be applied only to data rates up to 40 Gb/s [42, 43, 44]. Recently though, eye diagrams even at a data rate of 160 Gb/s were measured using a double-pass EAM configuration [22].

**O/E detection:** With respect to the O/E detection subsystem, more or less the same set-up was used in all experiments reported. The optical samples after the sampling gate were either amplified by an EDFA and detected by a low speed (few hundred MHz bandwidth) PIN photo diode or were directly detected by a low speed avalanche photo diode (APD). Depending on the nonlinear effect that had been used for gating, the detectors were sensitive at about 1550 nm or at about 780 nm. Finally, the signal was processed by either an A/D conversion board in a personal computer or by a digital oscilloscope. The resulting eye diagram was finally plotted on the personal computer or directly shown on the oscilloscope.

**Structure of this work:** This work is organized as follows. In **chapter 2** the fundamentals of optical sampling are discussed. First, the sampling principle is presented in detail and expressions for the sampling frequency, the number of samples per signal period as well as the sampling time step are derived. Next, the bandwidth of the optical sampling system is discussed. Then the construction of the eye diagrams measured by the optical sampling system is presented. Finally, the algorithm for the evaluation of the eye diagrams is given.

In **chapter 3** the set-up of the complete optical sampling system developed in this work is presented. The chapter is organized into five sections corresponding to the five main building blocks of the sampling system as identified in the previous section (Sec. 1.2). The chapter starts with a description of the two sampling gates used in this work. Then, the sampling pulse source is discussed and the technique used for compression of the sampling pulses as well as the reduction of the pulse repetition rate is presented. Next, the optical clock recovery is described. Finally, the clock processing unit as well as the sample detection unit are discussed briefly.

**Chapter 4** is devoted to the characterization of the developed optical sampling system. Since properties of the sampling system are mainly determined by the optical sampling gate, the chapter is split into two main sections, each dealing with one of the optical sampling gates described in Chap. 3. In the characterization of the sampling systems, the focus is on the temporal resolution as well as the wavelength range and the linearity of the systems.

Finally, applications of the developed sampling system are presented in **chapter 5**. The chapter is organized into three sections. Sec. 5.1 describes waveform measurements, while Sec. 5.2 describes eye diagram measurements. Finally, 160 Gbit/s transmission experiments are presented in Sec. 5.3, where the optical sampling system was used to investigate deteriorating effects like noise accumulation, fiber nonlinearity and residual chromatic dispersion. A summary and conclusion of this work is given in Chap. 6.

The **appendix** includes detailed information about the set-up of the 160 Gbit/s optical transmitter that was used in all experiments (Sec. A.1) as well as the numerical simulations that were performed in conjunction with the transmission experiments (Sec. A.2).

## Chapter 2

# Fundamentals of Optical Sampling

In this chapter the fundamentals of the optical sampling technique are discussed. First, the sampling principle is presented in detail and expressions for the sampling frequency, the number of samples that reproduce one signal period as well as the sampling time step are derived. Next, the bandwidth of the optical sampling system is discussed. It is shown that the bandwidth of the optical sampling gate directly corresponds to the overall bandwidth of the conventional electrical sampling system. Then the construction of the eye diagrams measured by the optical sampling system is presented. Finally, the algorithm for the evaluation of the eye diagrams is given.

## 2.1 Description of Optical Sampling Technique

The sampling technique in general allows to measure fast amplitude variations of a signal as a function of time by generating a time stretched image of the signal under investigation. This is schematically depicted in Fig. 2.1

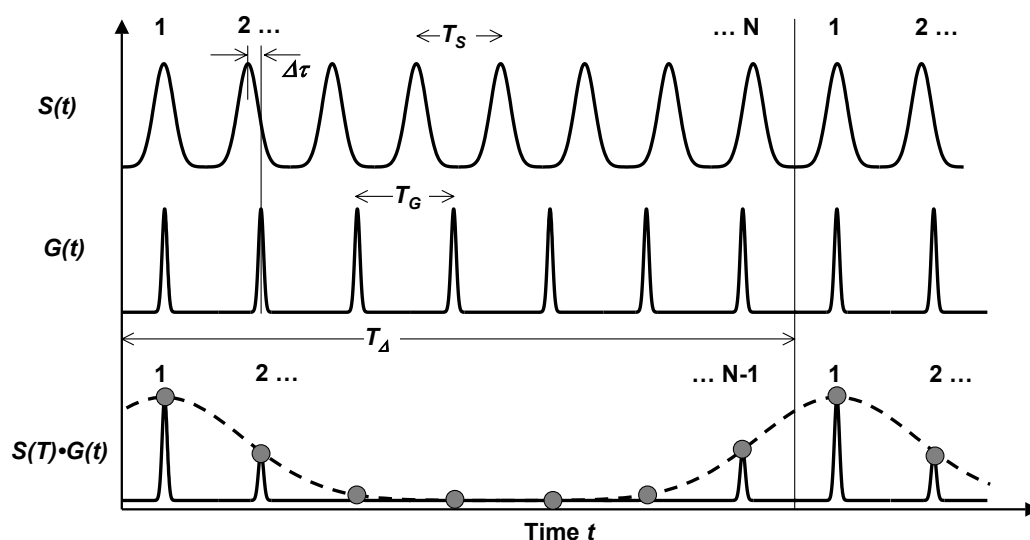


Figure 2.1: Relationship between the signal frequency and the sampling frequency.

The plot shows (from top to bottom) the signal under investigation, the gating function and the gated signal. The signal under investigation is a periodic pulse train in this example. The period  $T_S$  of the signal is the inverse of the repetition frequency  $f_S$  of the signal. The period of the gating function is  $T_G$  corresponds to the gating frequency (sampling frequency)  $f_G$ . In order to scan over the signal under investigation, the gating frequency differs from the signal frequency by a frequency offset  $\Delta f$ :

$$f_G = f_S - \Delta f \quad (2.1)$$

$\Delta f$  describes the frequency, at which the sampled image of the signal is generated. In general,  $\Delta f$  can either be positive or negative. If it is negative, then the time axis of the sampled data will be inverted. Therefore,  $\Delta f$  was chosen to be positive in the example discussed here. The period of the sampled image is given by  $T_\Delta = 1/\Delta f$

The stretch factor  $N$  of the sampled image of the signal under investigation is given by

$$N = \frac{T_\Delta}{T_S} \quad (2.2)$$

This equation can be used to calculate the offset frequency required to stretch the image of the signal by a factor  $N$ :

$$N = \frac{T_\Delta}{T_S} = \frac{f_S}{\Delta f} \quad (2.3)$$

$$\Leftrightarrow \Delta f = \frac{f_S}{N} \quad (2.4)$$

Using Eq. (2.1), the gating frequency thus becomes:

$$f_G = f_S - \frac{f_S}{N} = f_S \left( \frac{N-1}{N} \right) \quad (2.5)$$

This relation can be rewritten as relation between the periods of the signal and the gating function as follows:

$$(N-1) T_G = N T_S \quad (2.6)$$

From Eq. (2.6) it becomes clear that for  $N$  periods of the signal under investigation there are  $(N-1)$  periods of the gating function. In other words, the number of samples  $k$  by which one period of the signal under investigation is sampled in the time  $T_\Delta$  is given by:

$$k = N - 1 \quad (2.7)$$

Finally, the reproduced time step  $\Delta\tau$  between the individual samples can be calculated by:

$$\Delta\tau = \frac{T_S}{k} = \frac{1}{f_S} \frac{1}{N-1} \quad (2.8)$$



The relations derived above describe the situation when one sampling process takes place in each period  $T_S$  of the signal under investigation. This means that the sampling frequency is smaller than the signal frequency but larger than one half of it (see Eq. (2.5)). This is no problem as long as the signal under investigation is repetitive as shown in Fig.2.1. In the case of an optical data signal however, the amplitude of the signal under investigation will be different in each period  $T_S$  (corresponding to the bit-slot  $T_{bit}$ ). Therefore, the time stretched display of the signal cannot be detected by a low bandwidth envelope detector. Instead, each generated sample has to be detected individually by an analog to digital (A/D) converter. Since the acquisition speed of commercially available A/D converters is in the range of kHz to few hundred MHz, this would practically limit the repetition frequency or the bit rate of the signal under investigation to values of a few hundred MHz as well.

To overcome this limitation, the sampling frequency  $f_G$  is reduced in this work by a reduction factor  $M$  so that Eqs. (2.5) and (2.6) now become:

$$f'_G = f_S \left( \frac{N-1}{N} \right) \frac{1}{M} \quad (2.9)$$

$$(N-1) T_G = N (M \cdot T_S) \quad (2.10)$$

Eq. (2.10) shows that now the period  $T_\Delta$ , at which the time stretched replica of the signal is repeating, is increased by the factor  $M$ . The number of samples that are taken within this increased time  $M \cdot T_\Delta$  is still  $k = N - 1$ . However, the signal under investigation is reproduced  $M$  times within the increased time  $M \cdot T_\Delta$ . This can be verified by looking at Fig. 2.1 and considering the case of  $M = 2$  for example. In this case, the signal is reproduced twice within  $2 T_\Delta$ . The first replica of the signal consists of only the samples with odd sample numbers and the second replica consists of the samples with even sample numbers. In order to plot the acquired samples one way is to sort the samples after the acquisition.

Another way is to plot only the samples that are contained in the first of the  $M$  replicas of the signal under investigation. This was done in the work presented here. It means that only the samples within the time interval  $T_\Delta$  are considered even for the reduced sampling rate. In that case Eq. (2.10) can be re-written as

$$\frac{(N-1)}{M} T_G = N T_S \quad (2.11)$$

which shows that the number of samples taken per period  $T_\Delta$  is now reduced by the factor  $M$  to give:

$$k' = \frac{N-1}{M} \quad (2.12)$$

This reveals that the number of samples that reproduce one period of the signal under investigation is not an integer number any more, if the sampling frequency is reduced by the factor  $M$ . At the same time, the reproduced time step  $\Delta\tau$  between the individual samples is increased by the factor  $M$ :

$$\Delta\tau' = \frac{1}{f_S} \frac{M}{N-1} \quad (2.13)$$

## 2.2 Bandwidth of Optical Sampling Technique

In this section the equations that describe the bandwidth of the optical sampling technique are derived and compared to the electrical sampling technique. Please note that the terms bandwidth and temporal resolution are equivalent. The sampling system can either be described in the time domain by its gating function or in the frequency domain by its bandwidth. The bandwidth is the full width at half maximum of the Fourier transform of the time domain gating function. An optical sampling system is typically characterized in the time domain by its temporal resolution or gating function, while an electrical sampling system is often characterized in the frequency domain by its bandwidth.

Fig. 2.2 shows the block diagram for the optical sampling and the conventional electrical sampling of an optical data signal. The optical signal is represented by its complex electrical field  $E(t)$

$$E(t) = \sqrt{\eta P(t)} \exp(i\omega_0 t - i\phi(t)) \quad (2.14)$$

In the case of the conventional electrical sampling technique, the optical signal is first detected by a photodetector. The detected amplitude  $S^{D,el}(t)$  is proportional to the square of the optical field:

$$S^{D,el}(t) = \xi |E(t)|^2 \quad (2.15)$$

$$= \xi \eta P(t) = \eta' P(t) \quad (2.16)$$

Here,  $\xi$  is a conversion factor which includes the responsivity of the photodetector.  $\eta' = \xi \cdot \eta$  is the proportionality factor between the optical power and the generated signal. The limited electrical bandwidth of the photodetector is accounted for by a subsequent electrical low pass filter. The filter is described in the time domain by its filter function  $F^{el}(t)$ . The output signal of the filter is then given by the convolution (denoted by the symbol  $*$ ) of the signal and the filter function:

$$S^{F,el}(t) = S^{D,el}(t) * F^{el}(t) \quad (2.17)$$

$$= \int S^{D,el}(t') F^{el}(t - t') dt' \quad (2.18)$$

$$= \eta' \int P(t') F^{el}(t - t') dt' \quad (2.19)$$

The integration ranges from  $-\infty$  to  $\infty$  for all integrals shown in this section. Then the filtered signal is sampled by an electrical sampling gate inside the electrical sampling oscilloscope. The gating function of the sampling gate is  $G^{el}(t - \tau)$ , where  $\tau$  is the time of the sampling event. The output signal of the electrical sampling gate thus becomes

$$S^{G,el}(t - \tau) = S^{F,el}(t) \cdot G^{el}(t - \tau) \quad (2.20)$$

$$= \eta' G^{el}(t - \tau) \int P(t') F^{el}(t - t') dt' \quad (2.21)$$

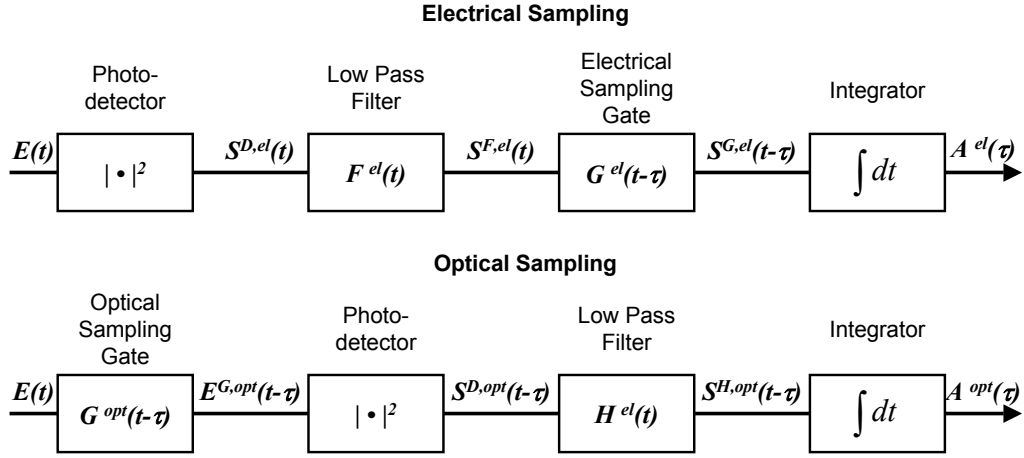


Figure 2.2: Block diagram of the optical sampling technique (top) compared to the conventional electrical sampling technique (bottom).

Finally, the amplitude of the sample is determined by integrating over one sampling period with an electrical integrator inside the electrical sampling oscilloscope:

$$A^{el}(\tau) = \int S^{G,el}(t - \tau) dt \quad (2.22)$$

$$= \eta' \int_t G^{el}(t - \tau) \int_{t'} P(t') F^{el}(t - t') dt' dt \quad (2.23)$$

$$= \eta' G^{el}(t) * (P(t) * F^{el}(t)) \quad (2.24)$$

$$= \eta' P(t) * \underbrace{(G^{el}(t) * F^{el}(t))}_{F'(t)} \quad (2.25)$$

This shows that the amplitude of the sample in the electrical sampling scheme is given by the convolution of the power of the optical signal with the overall filter function  $F'(t)$  of the photodetector and of the electrical sampling gate. This corresponds to the overall bandwidth of the electrical sampling system. Typically, the bandwidths of the photodetector and of the electrical sampling gate are comparable and both are in the order of 50 GHz.

In the case of the optical sampling technique, the input signal is sampled in the optical domain by an optical sampling gate having the gating function  $G^{opt}(t - \tau)$ . The gating function is related to the transmittance of the gate (Eq. (3.4)) by

$$|G^{opt}(t - \tau)|^2 = T(t - \tau) \quad (2.26)$$

The optical field of the gated signal then becomes

$$E^{G,opt}(t - \tau) = E(t) \cdot G^{opt}(t - \tau) \quad (2.27)$$

Then the gated field is detected by a photodetector, which generates the following electrical signal:

$$S^{D,opt}(t - \tau) = \xi |E^{G,opt}(t - \tau)|^2 \quad (2.28)$$

$$= \xi |E(t) \cdot G^{opt}(t - \tau)|^2 \quad (2.29)$$

$$= \xi \eta P(t) \cdot T(t - \tau) = \eta' P(t) \cdot T(t - \tau) \quad (2.30)$$

The bandwidth of the photodetector is again accounted for by a low pass filter with the time domain filter function  $H^{el}(t)$ . By introducing the substitution

$$\tilde{t} = t - \tau \quad (2.31)$$

$$\tilde{t}' = t' - \tau \quad (2.32)$$

the filtered signal is given by

$$S^{H,opt}(\tilde{t}) = S^{D,opt}(\tilde{t}) * H^{el}(\tilde{t}) \quad (2.33)$$

$$= \int S^{D,opt}(\tilde{t}') H^{el}(\tilde{t} - \tilde{t}') d\tilde{t}' \quad (2.34)$$

$$= \eta' \int P(t') T(t' - \tau) H^{el}(t - t') dt' \quad (2.35)$$

Finally, the amplitude of the sample is again yielded by integrating over one sampling period:

$$A^{opt}(\tau) = \int S^{H,opt}(\tilde{t}) dt \quad (2.36)$$

$$= \eta' \int_t \int_{t'} P(t') T(t' - \tau) H^{el}(t - t') dt' dt \quad (2.37)$$

$$= \eta' \int_{t'} P(t') T(t' - \tau) \int_t H^{el}(t - t') dt dt' \quad (2.38)$$

In the optical sampling technique, the optical gating process is taking place at a modest sampling frequency of a few hundred MHz. The bandwidth of the photodetector is chosen such that its bandwidth is significantly larger than the sampling frequency. Thus, its filter function  $H^{el}(t)$  can be considered as  $\delta$ -function. Therefore, Eq. (2.38) can be simplified to

$$A^{opt}(\tau) = \eta \int_{t'} P(t') T(t' - \tau) dt' \quad (2.39)$$

$$= \eta' P(t) * T(t) \quad (2.40)$$

Eq. (2.40) shows that the signal amplitude in the optical sampling scheme is given by the convolution of the signal power with the gating window of the optical sampling gate. Comparison of Eq. (2.39) with Eq. (2.25) reveals that the gating window  $T(t)$  of the optical sampling gate in the optical sampling system is equivalent to the overall

electrical filter function  $F'(t)$  of the photodetector and electrical sampling gate in the conventional electrical sampling system.

In the numerical simulations performed in this work, the optical sampling system was thus modelled as electrical sampling system with an equivalent electrical bandwidth. This bandwidth was given by the full width at half maximum of the Fourier transform of the gating window of the optical sampling gate.

## 2.3 Construction of the Eye Diagram

In an optical sampling system, the signal amplitude  $A$  is measured as a function of the time  $t$ , i.e. a finite number of pairs  $(A, t)$  is collected. Each pair  $(A, t)$  is called measured data point. In order to plot an eye diagram from the measured data points, the following procedure was used:

Let  $A_{min}$  and  $A_{max}$  define the amplitude range  $A_{min} \dots A_{max}$  in which all measured data points fall. The limits shall be chosen such that  $A \in ]A_{min}, A_{max}]$ . In the same way, let  $t_{min} \dots t_{max}$  define the temporal range in which all measured data points fall ( $t \in ]t_{min}, t_{max}]$ ). Then divide both ranges into a finite number of  $M$  and  $N$  adjacent intervals with widths

$$\begin{aligned}\Delta A &= \frac{A_{max} - A_{min}}{M} \\ \Delta t &= \frac{t_{max} - t_{min}}{N}\end{aligned}\tag{2.41}$$

Now generate an  $(M, N)$ -matrix  $\underline{H}$  which shall contain the frequencies of occurrence by which the measured data points fall into a specific amplitude/time interval. For each measured data point, increase the matrix element  $h_{mn}$  by one if

$$\begin{aligned}(m-1)\Delta A + A_{min} &< A \leq m\Delta A + A_{min} \\ \text{AND} \\ (n-1)\Delta t + t_{min} &< t \leq n\Delta t + t_{min}\end{aligned}\tag{2.42}$$

This means that a "hit" is generated in the matrix element  $h_{mn}$  if the measured data point falls into the  $m$ -th amplitude interval and the  $n$ -th time interval.

Fig. 2.3 shows an intensity plot of the resulting matrix  $\underline{H}$ . This type of plot is commonly referred to as eye diagram. It shows the relative probability by which the measured signal appears in the individual intervals given by Eqs. (2.42). The color scale is a measure of the number of hits in a particular interval.

It has been pointed out in Sec. 1.1 that the intention of the optical sampling system is to measure statistical information about the optical data signal. Therefore the measurement of the signal amplitude  $A$  as a function of time  $t$  within the time interval  $\Delta t$  is repeated a certain number of times. This is called **persistence** of the eye diagram. The persistence can either be given as number of acquisition cycles or as absolute time in which all acquisition cycles were performed. Typical eye diagrams have a persistence time on the order of milliseconds to seconds and contain a few ten to hundred acquisition cycles.

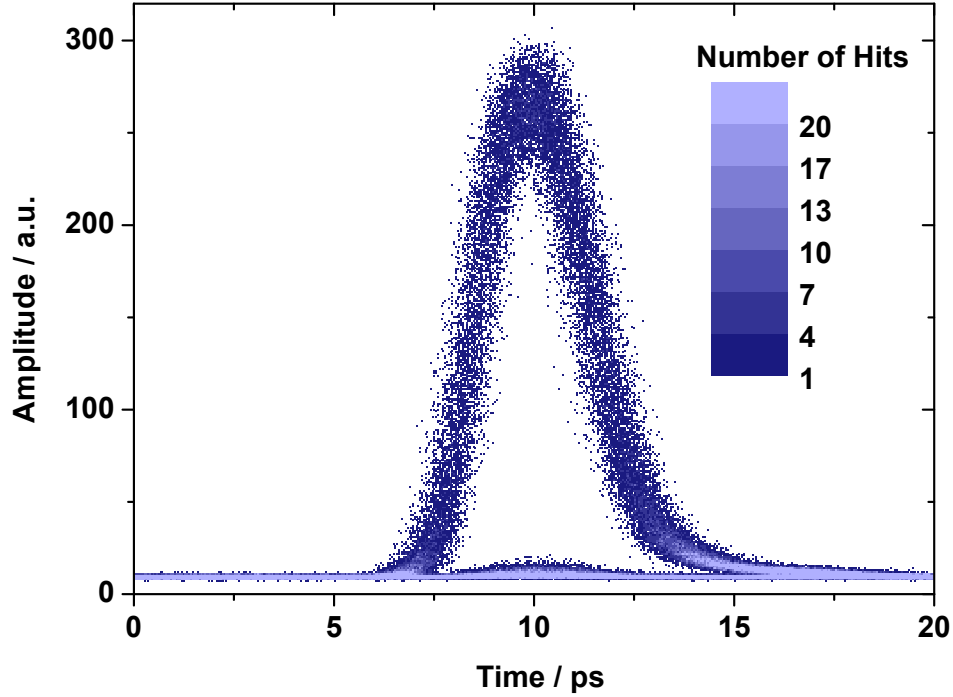


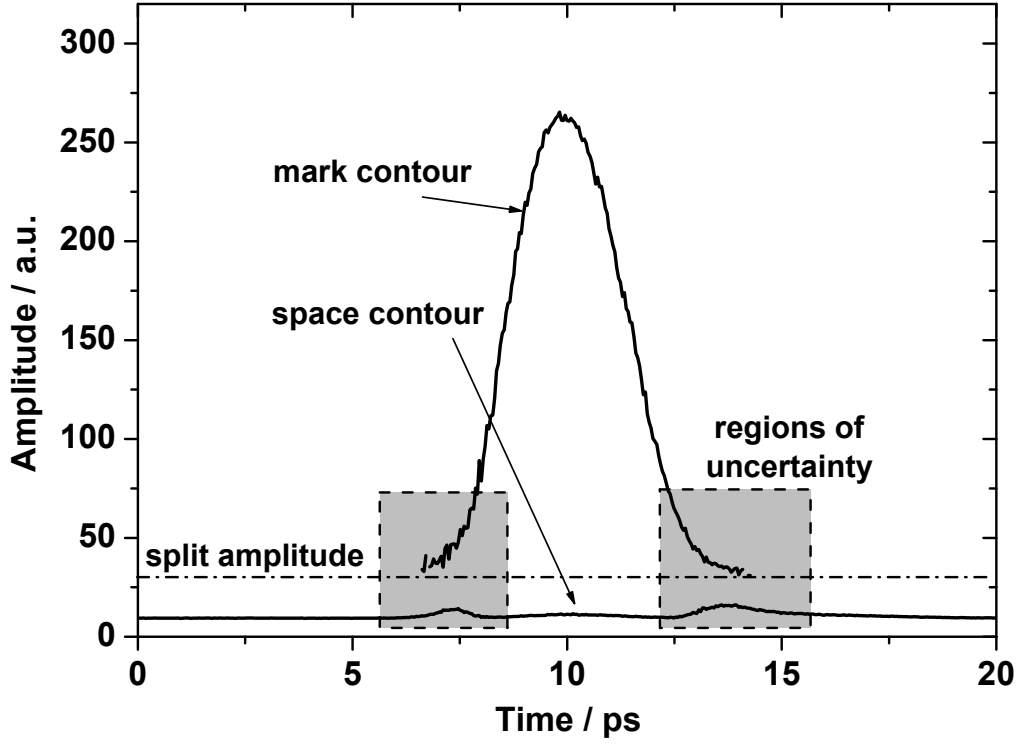
Figure 2.3: Intensity plot of the matrix  $\underline{H}$  showing a measured 10 Gbit/s RZ eye diagram.

## 2.4 Evaluation of the Eye Diagram

Having constructed the eye diagram  $\underline{H}$  in the way described in the previous section, a number of useful quantities are derived from  $\underline{H}$  which describe the properties of the measured data signal. First, it is useful to extract the contour line from the eye diagram in order to derive average quantities that are related to the shape of the eye diagram.

### 2.4.1 Average Properties of the Signal

Since the eye diagram contains measured data points from logical mark levels as well as from logical space levels, it is convenient to split the measured amplitude range. The split amplitude  $A_{split}$  corresponds to an amplitude index  $m_{split}$  at which the eye diagram matrix  $\underline{H}$  is now split into two matrices  $\underline{H}_{mark}$  and  $\underline{H}_{space}$  such that  $\underline{H}_{mark}$  contains all  $h_{mn}$  with  $m \geq m_{split}$  and  $\underline{H}_{space}$  contains all  $h_{mn}$  with  $m < m_{split}$ . This means the following. Ideally, all  $h_{mn}$  are zero in  $\underline{H}_{space}$  if the data signal comprises only "marks". Correspondingly, all  $h_{mn}$  are zero in  $\underline{H}_{mark}$  if the data signal comprises only "spaces". Then the average amplitude  $\bar{A}$  for each time interval  $n$  was calculated for both the mark and space region by

Figure 2.4: *Extracted contour lines from Fig. 2.3.*

$$\bar{A}_{mark}(n) = \frac{1}{M - m_{split} + 1} \sum_{m_{split}}^M h_{mn} \quad (2.43a)$$

$$\bar{A}_{space}(n) = \frac{1}{m_{split} - 1} \sum_{m=1}^{m_{split}-1} h_{mn} \quad (2.43b)$$

Eqs. (2.43) describe the contour lines of the mark and space levels. Fig. 2.4 shows such contour lines for the example of the eye diagram shown in Fig. 2.3. The transitions from the space to the mark level lead to regions of uncertainty where the average amplitude in the mark level is influenced by data points from the space level and vice versa. These regions have to be excluded from any further evaluation.

The choice of the split amplitude  $A_{split}$  must be taken based on the following constraints: The split amplitude must be larger than the largest amplitude in the space level. At the same time it should be as low as possible in order to leave the flanks of the mark contour line uninfluenced by the regions of uncertainty. For a completely automated eye diagram evaluation, the split amplitude has to be determined by an automatic algorithm. Although this is possible in general, it can require rather sophisticated algorithms if the structure of the signal under investigation (i.e. the shape of the eye diagram) is a priori unknown. Therefore in the work presented here, the split amplitude was determined manually.

Having extracted the mark and space contour lines, the following parameters were derived:

**Baseline amplitude:** Any detector produces a certain background signal even in the absence of an input signal. This background signal generates a displayed baseline amplitude which is added to the measured signal amplitude. One way to determine the baseline amplitude would be to block the input of the measurement instrument and measure the displayed average background amplitude. In the special case of the measurement of RZ eye diagrams, the baseline amplitude can however be extracted directly from a region of the measured eye diagram, where the actual signal amplitude has dropped to zero. In Fig. 2.3 this was the case at the left and right border of the measured time interval. Thus for the automatic eye diagram evaluation, the baseline amplitude was assumed to be the leftmost value in the space contour:

$$A_{base} = \bar{A}_{space}(1) \quad (2.44)$$

**Peak amplitude and position:** In order to determine the **peak amplitude**  $A_{peak}$  as well as the **peak position**  $t_{peak}$ , a Gaussian fit was applied to the mark contour.

Using the peak amplitude and the baseline amplitude, the half amplitude level  $A_{1/2}$  was calculated by

$$A_{1/2} = 0.5(A_{peak} - A_{base}) + A_{base} = 0.5(A_{peak} + A_{base}) \quad (2.45)$$

**Width of the eye diagram:** The width of the eye diagram was measured as full-width at half maximum. It was calculated by finding the temporal positions  $t_{1/2,left}$  and  $t_{1/2,right}$ , at which the mark contour dropped below the half amplitude level. The width then was the difference between the two temporal positions:

$$\tau_{Eye} = t_{1/2,right} - t_{1/2,left} \quad (2.46)$$

## 2.4.2 Statistical Properties of the Signal

The quantities derived so far describe the average properties of the measured data signal. Even more interesting however are the statistical properties of the measured data signal. These can be derived by extracting histograms from the eye diagram matrix  $\underline{H}$ .

The commonly used approach is to extract horizontal and vertical histograms. In order to do so, histogram windows have to be defined, which limit the range of measured data points taken into account for the evaluation. Fig. 2.5a) shows two histogram windows. The horizontal histogram window covers the whole measured time range and is centered at the half amplitude level  $A_{1/2}$  which was calculated before (Eq. (2.45)). The vertical histogram window covers the whole measured amplitude range and is centered around the peak position  $t_{peak}$  which also was calculated before. The horizontal histogram window has a height of 2 % of the amplitude of the eye diagram while the vertical histogram has a width of 5 % of the full-width at half



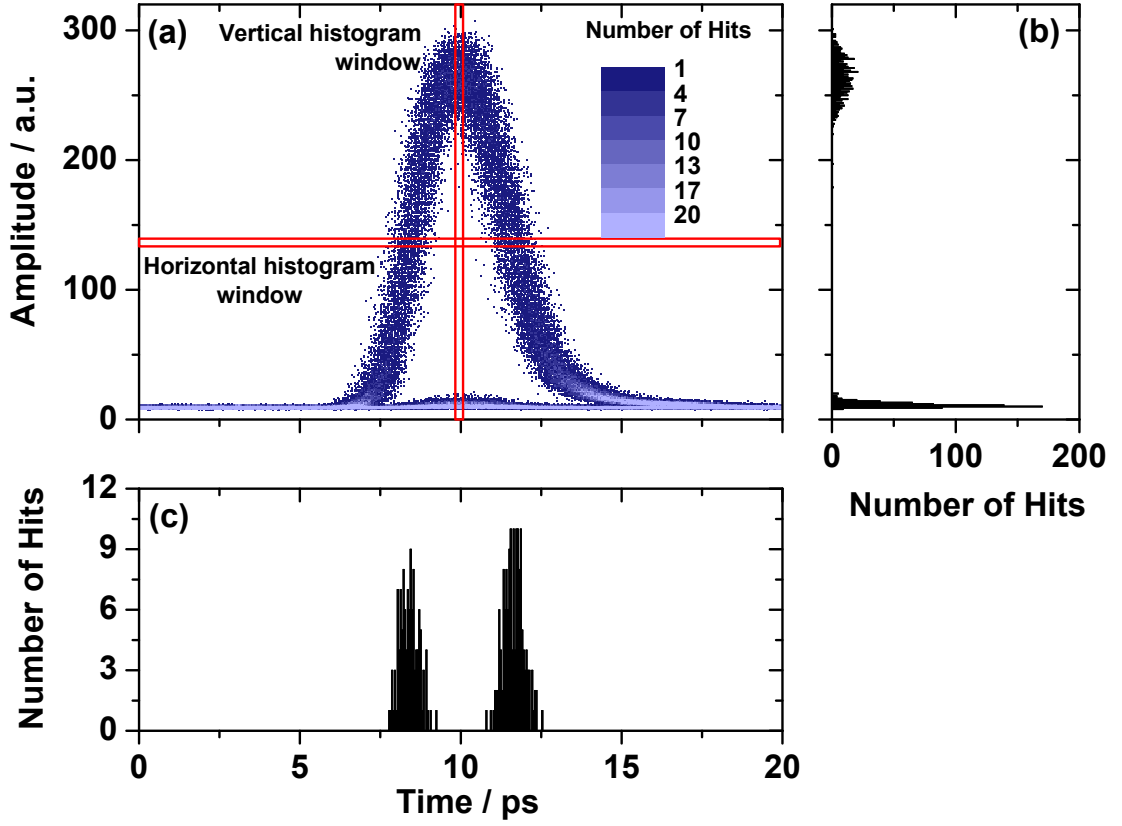


Figure 2.5: Example of a measured 10 Gbit/s RZ eye diagram (a) as well as extracted vertical (b) and horizontal (c) histograms.

maximum of the eye diagram. Two constraints have to be considered when choosing the dimensions of the histogram windows. First, the windows should be as narrow as possible so that inside the window the signal amplitude only varies approximately perpendicular to the histogram direction. On the other hand, the window should contain a sufficient number of hits in order to derive statistical quantities without having to increase the measurement time too much. The dimensions used in this work were chosen as a compromise between these two constraints.

If  $m_{low}$  and  $m_{high}$  denote the indices for the lowest and the highest amplitude level inside the horizontal histogram window, then the horizontal histogram  $H_{(n)}$  is an N-tupel given by

$$H_{(n)} = (h_1, h_2, \dots, h_N) \quad (2.47)$$

$$= \left( \sum_{m_{low}}^{m_{high}} h_{m1}, \sum_{m_{low}}^{m_{high}} h_{m2}, \dots, \sum_{m_{low}}^{m_{high}} h_{mN} \right) \quad (2.48)$$

In the same manner, the vertical histogram  $V_{(m)}$  is an M-tupel given by

$$V_{(m)} = (v_1, v_2, \dots, v_M) \quad (2.49)$$

$$= \left( \sum_{n_{left}}^{n_{right}} h_{1n}, \sum_{n_{left}}^{n_{right}} h_{2n}, \dots, \sum_{n_{left}}^{n_{right}} h_{Mn} \right) \quad (2.50)$$

where  $n_{left}$  and  $n_{right}$  denote the indices for the leftmost and rightmost temporal position inside the vertical histogram window.

Fig. 2.5b) shows the extracted vertical histogram  $V_{(m)}$  while Fig. 2.5c) shows the extracted horizontal histogram  $H_{(n)}$ . Both histograms show two distinct distributions.

### Horizontal Histogram

In the horizontal histogram, the two distributions correspond to the rising and falling flank of the eye diagram. It is useful to split the histogram at a position  $n_c$  in the middle of the two distributions. Then the mean and the standard deviation of the two distributions can be calculated by

$$\mu = \frac{\sum_n h h_n \cdot t_n}{\sum_n h h_n} \quad (2.51)$$

$$\sigma = \sqrt{\frac{\sum_n h h_n (t_n - \mu)^2}{\sum_n h h_n}} \quad (2.52)$$

where the sum is carried out over  $n = 1 \dots n_c - 1$  for the left distribution and  $n = n_c \dots N$  for the right distribution. The time  $t_n$  corresponding to the temporal index  $n$  is given by the middle of the  $n$ -th time interval:

$$t_n = (2n - 1) \frac{\Delta t}{2} + t_{min} \quad (2.53)$$

**Half amplitude positions:** The mean values  $t_{left} = \mu_{left}$  and  $t_{right} = \mu_{right}$  yield the temporal positions of the half amplitude levels at the left and right flank. They can be used to calculate again the width  $\tau_{Eye}$  of the eye diagram in the same manner as described in the previous section.

**RMS timing jitter:** The standard deviations  $\sigma_{left}$  and  $\sigma_{right}$  describe the RMS timing jitter of the data signal. Ideally, both values should be the same. However, due to the finite height of the histogram window, the values will slightly differ if the steepness of the flanks is not equal. Then, the steeper flank will yield a smaller value for the timing jitter than the smoother flank. Since the increase of the derived jitter value for the smoother flank is an artefact of the evaluation procedure which cannot be circumvented, it is however fair to use the lower value yielded by the steeper flank in that case.

### Vertical Histogram

In the vertical histogram, the two distributions correspond to the mark and space level amplitudes of the eye diagram. The vertical histogram is treated analogous to the horizontal histogram by splitting it at an amplitude level  $A_c$  in the middle of the two distributions and then calculating the means  $\mu_{0/1}$  and standard deviations  $\sigma_{0/1}$  for both amplitude distributions.

**Mean amplitudes:** The mean value of the mark distribution  $\mu_1$  corresponds to the mean amplitude of the logical marks in the data signal. It is equal to the peak amplitude of the eye diagram as derived before as one of the average properties of the signal. The mean value of the space distribution  $\mu_0$  yields the mean amplitude level of logical spaces in the data signal. It must not be confused with the baseline amplitude derived earlier. The baseline amplitude is the background amplitude of the optical sampling system in the absence of an input signal. The mean space amplitude however is in practice higher than the baseline amplitude due to the limited extinction ratio of the data transmitter.

**Extinction ratio:** The ratio between the mean mark amplitude  $\mu_1$  and mean space amplitude  $\mu_0$  yields the extinction ratio  $ER$  of the signal. It is expressed in a logarithmic scale and reads as follows:

$$ER[\text{dB}] = 10 \log \frac{\mu_1}{\mu_0} \quad (2.54)$$

The extinction ratio is commonly used to describe the properties of an optical data transmitter rather than the data signal itself.

**Eye opening / eye opening penalty:** Another important parameter that is derived from the mark and space distributions is the eye opening  $EO$ . It is defined as the amplitude difference between the lowest amplitude interval in the mark distribution, which contains at least one hit, and the highest amplitude interval in the space distribution, which contains at least one hit. The eye opening is a measure for the signal quality. A large eye opening corresponds to a high signal quality, since the logical marks and spaces are well separated in amplitude. A low eye opening corresponds to a poor signal quality, as the separation between the marks and spaces is low.

In order to compare different eye diagrams or to investigate the influence of certain effects on the signal quality, it is common to define the eye opening penalty  $EOP$ . The eye opening penalty is a relative quantity and describes the amount by which the eye opening of the particular eye diagram deviates from the the maximum eye opening  $\max(EO)$  of all eye diagrams considered in the particular comparison. The  $EOP$  is expressed in a logarithmic scale and can be written as:

$$EOP [\text{dB}] = -10 \log \frac{EO}{\max(EO)} \quad (2.55)$$

**Amplitude noise:** Analogous to the timing jitter, which was derived from the horizontal histogram, the standard deviations of the vertical histogram yield the amplitude variations of the signal. In particular, the standard deviation  $\sigma_1$  of the mark distribution is called amplitude noise  $AN$  of the data signal.

$$AN = \sigma_1 \quad (2.56)$$

A high amplitude noise indicates a poor signal quality as it degrades the eye opening of the eye diagram. However, the amplitude noise is not directly a measure of the absolute signal quality, since the same data signal will exhibit a large amplitude noise if it has a larger mean amplitude whereas it will exhibit a small amplitude noise if it has a small mean amplitude. Therefore, the amplitude noise has to be considered in combination with the mean signal amplitude to derive an absolute quality indicator for the data signal.

**Q-factor / bit error rate:** As has just been described, the combination of the amplitude noise and the mean signal amplitude can be used to define a quality factor (Q-factor), which describes the quality of the data signal. Since in general both the mark level as well as the space level show an amplitude distribution, the Q-factor includes the standard deviations and mean values of both distributions. It is defined as:

$$Q = \frac{\mu_1 - \mu_0}{\sigma_1 + \sigma_0} \quad (2.57)$$

Under the assumption that the amplitude noise is dominated by Gaussian noise, the Q-factor is related to the bit-error ratio  $BER$  of the data signal by the complementary error function  $\text{erfc}(x)$ :

$$BER = \text{erfc}\left(\frac{Q}{\sqrt{2}}\right) \quad (2.58)$$

with

$$\text{erfc}(x) = 1 - \text{erf}(x) = 1 - \frac{2}{\sqrt{\pi}} \int_{t=0}^x e^{-t^2} dt \quad (2.59)$$

In this work, an evaluation software was implemented using National Instruments' LabVIEW programming language. The software acquired the data points  $(A, t)$  from the A/D converter in the sampling system set-up. Then it automatically performed the data signal evaluation steps described in this section. All calculations were performed in real-time thus allowing to quickly assess the quality of the signal under investigation. All presented eye diagrams in this work were evaluated using the automatic parameter extraction procedure described above.

## Chapter 3

# Set-Up of the Optical Sampling System

The set-up of the optical sampling system can be sub-divided into mainly five building blocks as shown in Fig. 3.1. These building blocks are the sampling pulse source,

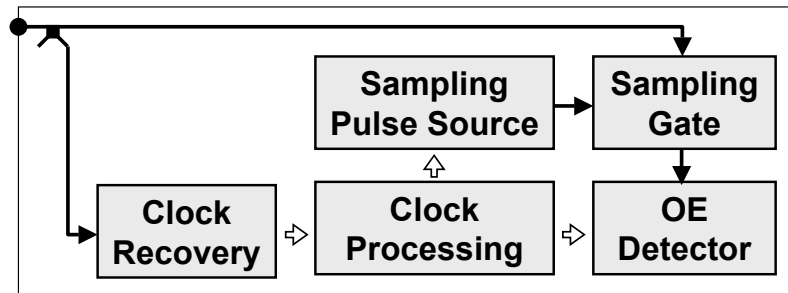


Figure 3.1: *Block diagram of the optical sampling system. Solid lines indicate the optical path. Hollow arrows indicate electrical connections.*

the clock recovery, the clock processing, the sampling gate and the opto/electrical (OE) detector. This chapter describes the set-up of all building blocks of the optical sampling system in detail.

### 3.1 Sampling Gate

As discussed in Sec. 1.2, an optical sampling system differs from an electrical sampling system by the type of sampling gate that is used. The application of an ultrafast all-optical gate instead of an electrical gate provides a significant increase in bandwidth. Several all-optical gates have been used in optical sampling set-up's (see Sec. 1.3). The experiments described in this work were performed using mainly two different optical gates. Both gates were interferometric optical gates. In this type of gate, cross-phase modulation is used in combination with an interferometric set-up to generate gating windows having a width (FWHM) of less than 3 ps.

Fig. 3.2 illustrates the basic principle that applies to both gates. It shows a Mach-

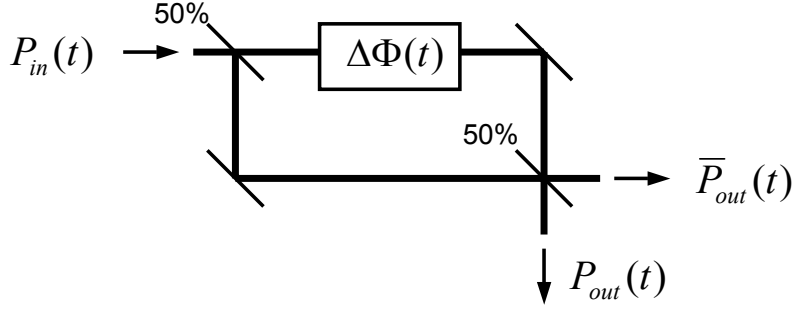


Figure 3.2: Schematic set-up of an interferometric optical gate in a Mach-Zehnder configuration.

Zehnder interferometer (MZI). An optical signal with time dependent power  $P_{in}(t)$  is input. The signal is split by a beam splitter with a splitting ratio of 50 %. The two parts of the signal travel along the two branches of the interferometer and are recombined at a second beam splitter (also 50 % splitting ratio). The optical path length  $\ell_{opt}$  is defined as

$$\ell_{opt} = n \cdot \ell \quad (3.1)$$

where  $n$  is the refractive index of the medium through which the signal propagates and  $\ell$  is its geometrical length. Assuming equal optical path length in both interferometer branches, the optical signal will constructively interfere at the output port  $\bar{P}_{out}(t)$ . However, if the optical path lengths of the two interferometer branches differ, part of the signal will interfere constructively at the output port  $P_{out}(t)$ . The signal will interfere completely to  $P_{out}(t)$  if the path length difference  $\Delta\ell_{opt}$  becomes

$$\Delta\ell_{opt} = \frac{\lambda}{2\pi}(2m - 1)\pi \quad (3.2)$$

$$= \frac{\lambda}{2\pi}\Delta\Phi \quad (3.3)$$

where  $\lambda$  is the wavelength of the signal and  $m = 1, 2, \dots$ . The path length difference can thus be expressed as phase change  $\Delta\Phi$ . The interferometer can be used as an optical gate, if a time dependent optical phase change  $\Delta\Phi(t)$  in one branch of the interferometer is introduced. The dynamics of the induced phase change determine the dynamics of the optical gate. The most important figure of merit of a fast optical gate is its transmittance  $T(t)$  measured from the input port  $P_{in}$  to the output port  $P_{out}$ . It is defined as

$$T(t) = \frac{P_{out}(t)}{P_{in}(t)} \quad (3.4)$$

For the example of a lossless Mach-Zehnder interferometer with 50 % beam split-

ters, the transmittance is given by [45]:

$$T_{\text{MZI}}(t) = \frac{1}{2} [1 - \cos(\Delta\Phi(t))] \quad (3.5)$$

The equation shows that for a phase change of  $\Delta\Phi = 0$  the transmittance becomes zero and the gate is closed. If  $\Delta\Phi > 0$ , the gate opens and for  $\Delta\Phi = \pi$  the transmittance becomes  $T = 1$  which means that the input signal is completely gated to the output port  $P_{\text{out}}$ . From Eq. (3.5) it is clear, that the faster the phase change occurs, the faster the gate opens and closes. The time dependence of the transmittance is also commonly referred to as "gating window" (GW) of the interferometric gate.

The two optical gates studied in this work use cross-phase modulation in two different optical media, in a semiconductor optical amplifier (SOA) and in a highly nonlinear fiber (HNLF). A strong control pulse is injected in both media to cause an optical phase shift  $\Delta\Phi$  by cross-phase modulation. However, the dynamics of the induced phase change were different for the SOA and the HNLF as will be discussed later on.

Moreover, the two sampling gates were based on two different types of interferometers. Both interferometers were set up in a fiber-optic hybrid configuration, which means that the components used in the set-up were interconnected with each other by pieces of optical fibers. For a Mach-Zehnder interferometer this would require an active path length stabilization because the difference of the lengths of the two separated optical paths changes rapidly with temperature. To circumvent this problem, interferometers were used where the two branches of the interferometer were realized using the same optical fiber path. One example of such an interferometer is the Sagnac interferometer, which is also referred to as "nonlinear optical loop mirror" (NOLM) [46, 47, 48]. This type of interferometer was used together with the HNLF as nonlinear medium. Another example is a polarization interferometer where the two optical branches are represented by the two orthogonal states of polarization in one optical fiber. This interferometer is the so called "ultrafast nonlinear interferometer" (UNI) [49] which incorporated an SOA. The choice of the particular type of interferometer was based on the dynamics of the nonlinear medium used as will be discussed in the following sections.

### 3.1.1 Gain-Transparent Ultrafast Nonlinear Interferometer

In the "gain-transparent ultrafast nonlinear interferometer" (GT-UNI), the phase change was induced in a semiconductor optical amplifier (SOA). This medium is of particular interest for all-optical switching applications because of its compactness and potential for future monolithic integration. In the following subsections, the impact of the phase dynamics in SOA's to the application in ultrafast optical gates will be discussed. Subsequently, some design considerations regarding the achievable optical bandwidth will be given. Finally, the experimental set-up will be presented.

#### Phase dynamics and gating window width

Fig. 3.3 shows the simulation of the phase change  $\Delta\Phi(t)$  in an SOA upon injection of a strong optical control pulse (sampling pulse) at  $t = 50 \text{ ps}$  with a width of  $\tau_{\text{SP}} = 1.3 \text{ ps}$ .

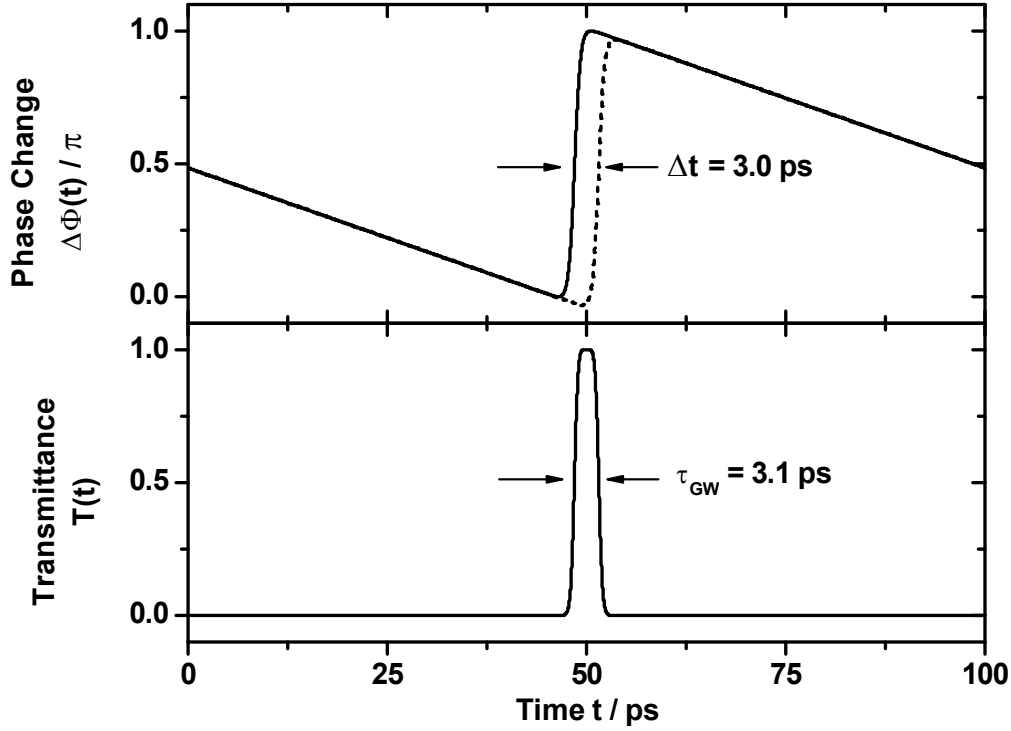


Figure 3.3: Phase change and resulting gating window (transmittance) in a differential SOA-based interferometer for a relative delay of the sampling pulses of  $\Delta t = 3.0$  ps.

It is well known that for sampling pulse widths in the order of few picoseconds, the phase dynamics can be described by an instantaneous increase followed by a slow recovery. The instantaneous phase change induced by the sampling pulse is assumed to be  $\Delta\Phi = \pi$  in this example. The slow recovery is approximated by a linear dependence. In general, the phase recovery actually shows an exponential decay. However, as will be shown later in this section, the shape of the decay mainly influences the contrast of the gate and is of negligible influence to the gating window widths that are achievable.

Considering the saw-tooth shaped phase change in the SOA, this would result in a fast opening of the gating window due to the instantaneous phase change but also a slow closing of the gating window due to the slow linear recovery. This drawback is overcome by a differential operation. This means that a second nonlinear element (not shown in Fig. 3.2), which is identical to the first one, is inserted into the second branch of the interferometer. In that case, the phase change  $\Delta\Phi(t)$  which determines the gating window is given by the difference of the two phase changes  $\Delta\Phi_{1,2}(t)$  in the two interferometer branches:

$$\Delta\Phi(t) = \Delta\Phi_1(t) - \Delta\Phi_2(t) \quad (3.6)$$

Fig. 3.3 shows the phase change  $\Delta\Phi_2(t)$  in the second interferometer branch as dashed line. In this example, the sampling pulse is injected into the second SOA with



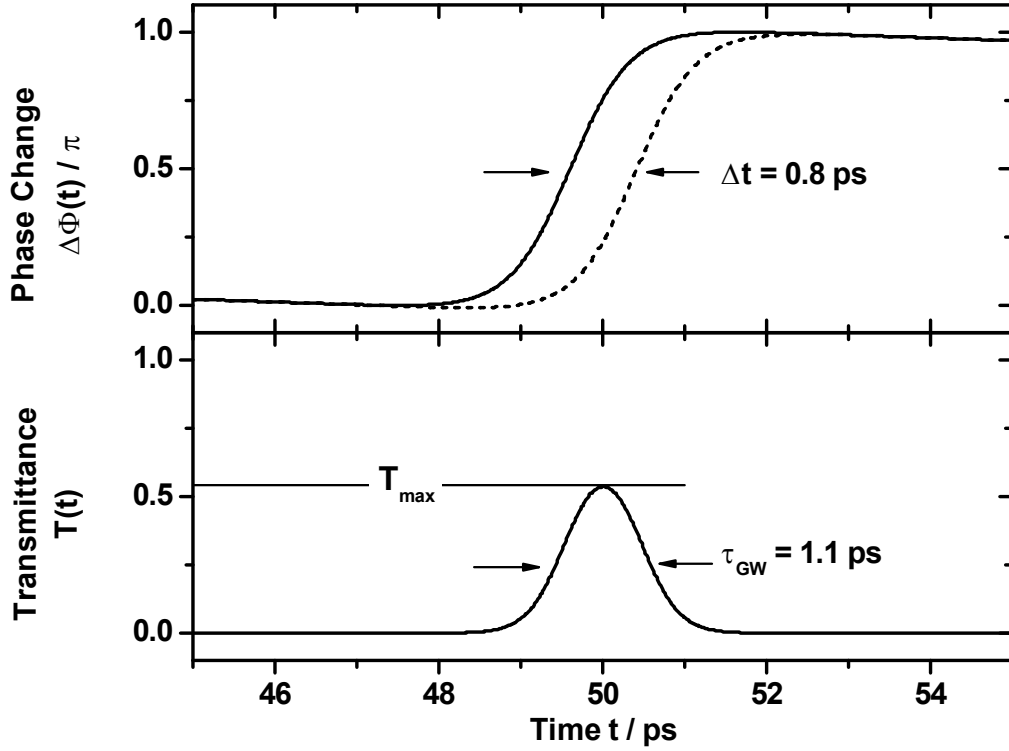


Figure 3.4: Phase change and resulting gating window (transmittance) in a differential SOA-based interferometer for a relative delay of the sampling pulses of  $\Delta t = 0.8$  ps.

a time delay  $\Delta t = 3.0$  ps. By proper adjustment of the two phase changes  $\Delta\Phi_{1,2}$  in the two branches the effect of the slow phase recovery is cancelled and a short gating window is generated. The width of the gating window is determined by the delay  $\Delta t$  between the injection of the sampling pulse into the two interferometer branches. For the example shown here, the gating window has a full width at half maximum (FWHM) of  $\tau_{GW} = 3.1$  ps. If the induced phase change is  $\pi$  as in the depicted example, the maximum transmittance becomes  $T_{max} = 1$ . Please note that the width of the gating window is slightly larger than the delay between the two phase curves. The reason for this is that the phase change induced by the optical sampling pulse is not instantaneous in practice. Instead, the finite width of the sampling pulse smears out the instantaneous phase change, which is taken into account in the simulation by convoluting the saw-tooth shaped phase change with the sampling pulse. This implies that the phase change depends linear on the sampling pulse power.

In an optical sampling system, the gating window width had to be reduced to about 1 ps. In this case, the maximum transmittance of the sampling gate decreases as Fig. 3.4 demonstrates. This figure shows the phase dynamics and transmittance (gating window) for a relative delay of  $\Delta t = 0.8$  ps. In this case it is clearly visible that the finite width of the sampling pulse smears out the instantaneous phase change. As a consequence, the differential phase change is always less than  $\pi$ , even though the sampling pulse introduces a phase change of  $\pi$ . Thus the maximum transmittance

of the gate decreases. This imposes a limit to the actual gating window widths that can practically be used in a sampling system.

### Optical bandwidth

The simulations of the gating window described above have been used to estimate the optical bandwidth that is achievable using an SOA-based interferometric gate. The 3 dB optical bandwidth  $B$ , which is one of the key figures of merit of an optical sampling system, can be calculated from the gating window width (FWHM)  $\tau_{GW}$  under the assumption of a Gaussian shaped gating window. The calculation yields [50]:

$$B = \frac{0.44}{\tau_{GW}} \quad (3.7)$$

To give a few examples, a gating window width of 3 ps roughly yields an optical bandwidth of 150 GHz while a gating window width of 1.5 ps corresponds to an optical bandwidth of 300 GHz.

Fig. 3.5 shows a parametric plot of the maximum transmittance  $T_{max}$  and the corresponding gating window width  $\tau_{GW}$  for the SOA based sampling gate as a function of the sampling pulse delay  $\Delta t$ . The gating window width is related to the optical bandwidth by Eq. (3.7).

Within each plotted line, a few distinct points are marked by symbols. These points represent certain relative delays  $\Delta t$  between the sampling pulses in the differential gating scheme. As expected, the gating window width decreases with decreasing delay  $\Delta t$ . However, the maximum transmittance also decreases when the delay becomes comparable to the width of the sampling pulses.

The width of the sampling pulses is indicated in the plot by different line styles (solid, dashed, dotted). The three line styles represent three different sampling pulse widths of  $\tau_{SP} = 0.9$  ps, 1.3 ps and 1.7 ps. It is interesting to note that a shorter the sampling pulse does not always generate a shorter gating window for a given delay  $\Delta t$ . In particular for maximum phase shifts smaller than  $\pi$  and delays of 3 ps and 4 ps, the situation is inverse. The reason is a change of the shape of the gating window due to the lower phase shift. The sampling pulse width used in this work for the GT-UNI gate was 1.3 ps and is shown as solid line.

Finally, the plot shows four groups of traces. Each group represents a different value of the maximum phase change  $\Delta\Phi_{max}$  that is induced by the sampling pulse. It can be seen that the maximum transmittance decreases when the maximum phase change is decreased.

For the application in a 160 Gb/s system environment, the sampling system should have an optical bandwidth of higher than 160 GHz. Experiments indicated that in a gain-transparent SOA as it was used in this work (see next subsection), a maximum phase shift of  $\Delta\Phi_{max} = 0.5\pi$  is a reasonable value [51, 52]. From Fig. 3.5 it is found that in this case and with a sampling pulse width of  $\tau_{SP} = 1.3$  ps as used in this work, a delay of  $\Delta t = 3.5$  ps would produce sufficiently short gating windows, however associated with a reduction of the maximum transmittance by about 50 %.

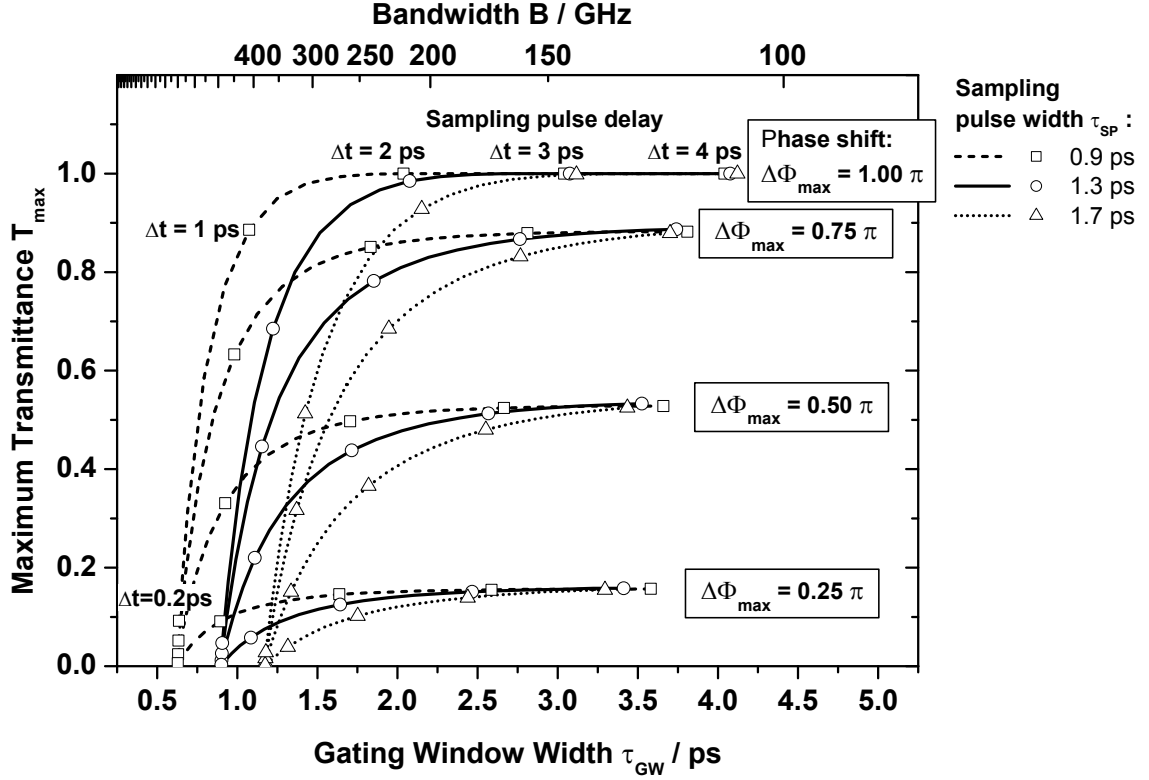


Figure 3.5: Calculated maximum transmittance  $T_{max}$  as a function of the gating window width  $\tau_{GW}$ . The parameters are the sampling pulse width  $\tau_{SP}$ , the maximum induced phase shift  $\Delta\phi_{max}$  and the delay  $\Delta t$  between the phase changes in the two interferometer branches.

A bandwidth of 300 GHz is already associated with a reduction of the maximum transmittance by 60 %.

### Set-up of GT-UNI

The set-up of the GT-UNI sampling gate is shown in Fig. 3.6 [53]. The optical data signal was input (upper right corner in Fig. 3.6) and fed into port 1 of a polarization beam splitter (PBS). The manual polarization controller PC1 in front of the PBS was adjusted to couple the signal completely to port 2 of the PBS. In Fig. 3.6 this corresponds to a linear polarization along the x-axis. Using the polarization controller PC2, the signal was launched into a piece of polarization maintaining fiber (PMF) with equal power in both principal axes of the PMF. At the output of the PMF, the power components along the two principal axes of the PMF were separated in time by the differential group delay (DGD) of the PMF. These two signal components were fed into the SOA via a circulator (CIRC) and a 1.3/1.5  $\mu\text{m}$  wavelength combiner (WDM-coupler). The WDM-coupler was used to insert the control pulses having a wavelength of 1310 nm into the SOA with low loss. In the absence of a control pulse, the two components of the data signal were passing through the SOA and were

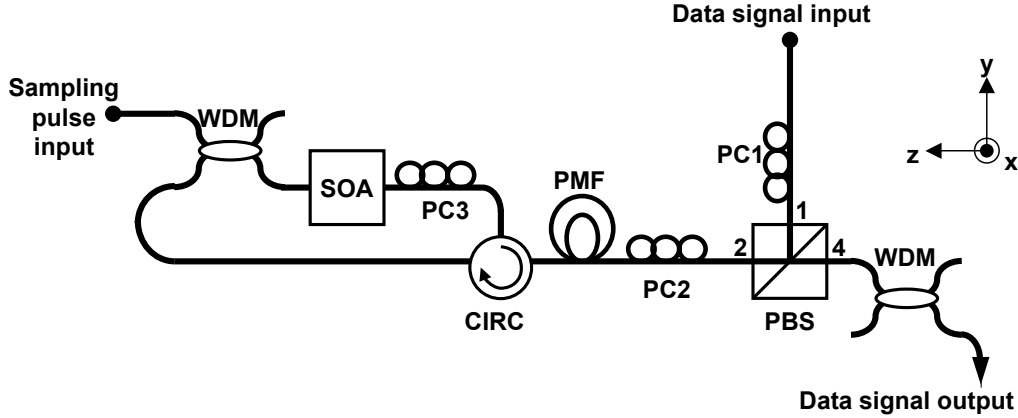


Figure 3.6: Schematic set-up of the GT-UNI sampling gate.

coupled back into the PMF via the circulator. The polarization controller PC3 was adjusted such that the component of the data signal, which had travelled along the fast axis of the PMF before, now was coupled into the slow axis of the PMF and vice versa. Thus the two components were realigned in time on the way back through the PMF and interfered at the PBS. In the absence of a control pulse, the data signal interfered constructively to a linear polarization along the x-axis in Fig. 3.6 and thus the data signal was sent back to the input port 1 of the gate. If a sampling pulse was inserted into the SOA between the slow and fast component of the data signal, the sampling pulse induced a phase difference  $\Delta\Phi$  between the two components. Due to this phase difference, part of the data signal interfered constructively at the PBS with a polarization along the y-axis in Fig. 3.6. This means that part of the data signal was gated to the output port 4. After transmission through the PBS, the control pulses were separated from the gated data signal by another WDM-coupler.

In the described set-up, the two interferometer branches were formed by the two orthogonal states of polarization that exist within an optical fiber. Also only one SOA was used, in which an optical phase change was induced by one sampling pulse. The time delay  $\Delta t$  was introduced by delaying the data signal in the two orthogonal polarization states before they entered the SOA. It can be shown that the operation principle of such polarization interferometer is similar to a Mach-Zehnder interferometer [54].

The SOA in the described sampling gate was operated in the "gain-transparent" (GT) scheme [55,56]. This means that the control pulses had a wavelength within the gain region of the SOA whereas the optical data signal had a wavelength outside the gain region (Fig. 3.7). As the data signal had a wavelength in the C-band (around 1550 nm), an SOA with a gain maximum around 1300 nm was chosen. The sampling pulses were at 1310 nm. The benefit of using the gain-transparent scheme is that the sampling pulses at 1310 nm induce a phase change of the data signal which is associated with a negligible gain change  $\Delta g$  [52]. This results in certain features that make this operation scheme in particular useful for optical sampling. These features will be discussed in detail in Sec. 4.1.

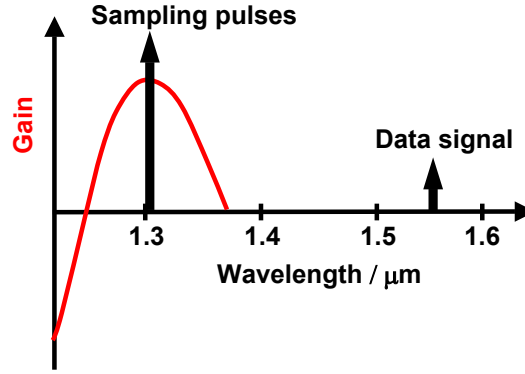


Figure 3.7: Schematic depiction of the wavelength of the sampling pulses and the data signal with respect to the gain curve of the SOA in the gain-transparent scheme.

### 3.1.2 Nonlinear Optical Loop Mirror

The second sampling gate studied in this work was a "Nonlinear Optical Loop Mirror" (NOLM). It has the geometry of a Sagnac interferometer. The nonlinear medium, that was used to induce a phase change, was a specially designed optical fiber with a high nonlinearity coefficient  $\gamma$ . These so called "highly nonlinear fibers" (HNLF) offer a nonlinearity coefficient which can be as much as 10-15 times larger than the nonlinearity coefficient in conventional fibers [57, 58]. The increase in the nonlinearity coefficient is achieved mainly by a much smaller effective area  $A_{eff}$  of the fiber, since

$$\gamma = \frac{n_2 \omega_0}{c A_{eff}} \quad (3.8)$$

Here,  $n_2$  is the nonlinear index coefficient (nonlinear refractive index),  $\omega_0$  is the optical (angular) frequency of the electrical field and  $c$  is the velocity of light.

#### Phase dynamics and gating window width

In the HNLF, a control pulse (sampling pulse) generates a phase shift  $\Delta\Phi(t)$  via cross-phase modulation. This phase shift is experienced by the data signal. Due to the fast Kerr-nonlinearity, the phase change instantaneously follows the power  $P(t)$  of the control pulse. In the case of co-polarized data and control signals, the induced phase change can be written as [59]:

$$\Delta\Phi(t) = 2\gamma L P(t) \quad (3.9)$$

Here,  $L$  is the length of the fiber and  $\gamma$  is the nonlinearity coefficient of the fiber. This simplified equation neglects temporal walk-off between the control and the signal pulses due to dispersion as well as changes in the control pulse shape due to self-phase modulation. Moreover it neglects deteriorating effects of the fiber like chromatic dispersion and polarization mode dispersion.

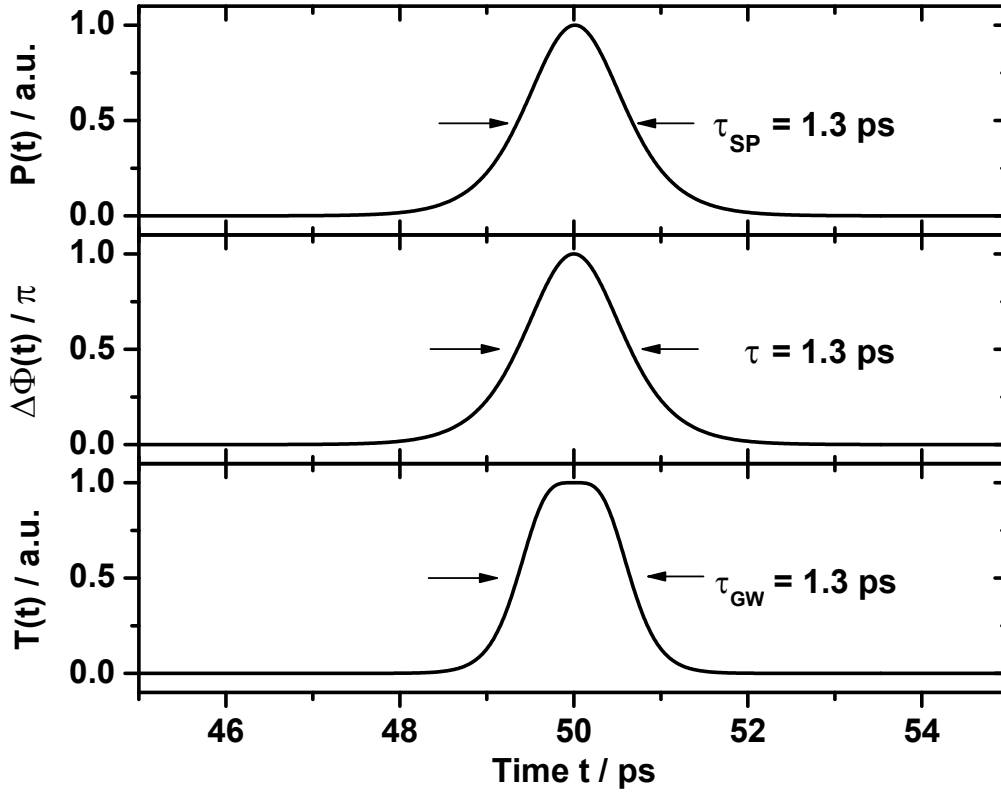


Figure 3.8: From top to bottom: Injected control pulse power  $P$ , induced phase shift  $\Delta\Phi$  and resulting transmittance  $T$  (gating window) as a function of time for the HNLf-based optical gate.

Fig. 3.8 shows the optical power  $P(T)$  of the control pulse (sampling pulse) and the induced phase change  $\Delta\Phi$  as described by Eq. (3.9). The resulting gating window as calculated using Eq. (3.5), which can also be used for the Sagnac interferometer geometry as long as the interaction between the counter-propagating fields can be neglected.

From Fig. 3.8 it is clear that in the case of the HNLf it is not necessary to use the differential scheme discussed in the previous section because the phase change shows no slow recovery. The resulting gating window shows a flattened top because of the cosine function in Eq. (3.5).

### Optical bandwidth

Eq. (3.9) shows that the width of the gating window is only limited by the sampling pulse width and shape. Fig. 3.9 depicts the maximum transmittance  $T_{max}$  (maximum of transmittance  $T$  shown in Fig. 3.8) versus the gating window width for the HNLf-based sampling gate. The traces have been calculated using Eqs. (3.5) and (3.9).

The plot shows four traces corresponding to different amounts of maximum induced phase shift  $\Delta\Phi_{max}$ . According to Eq. (3.9) the amount of phase shift depends

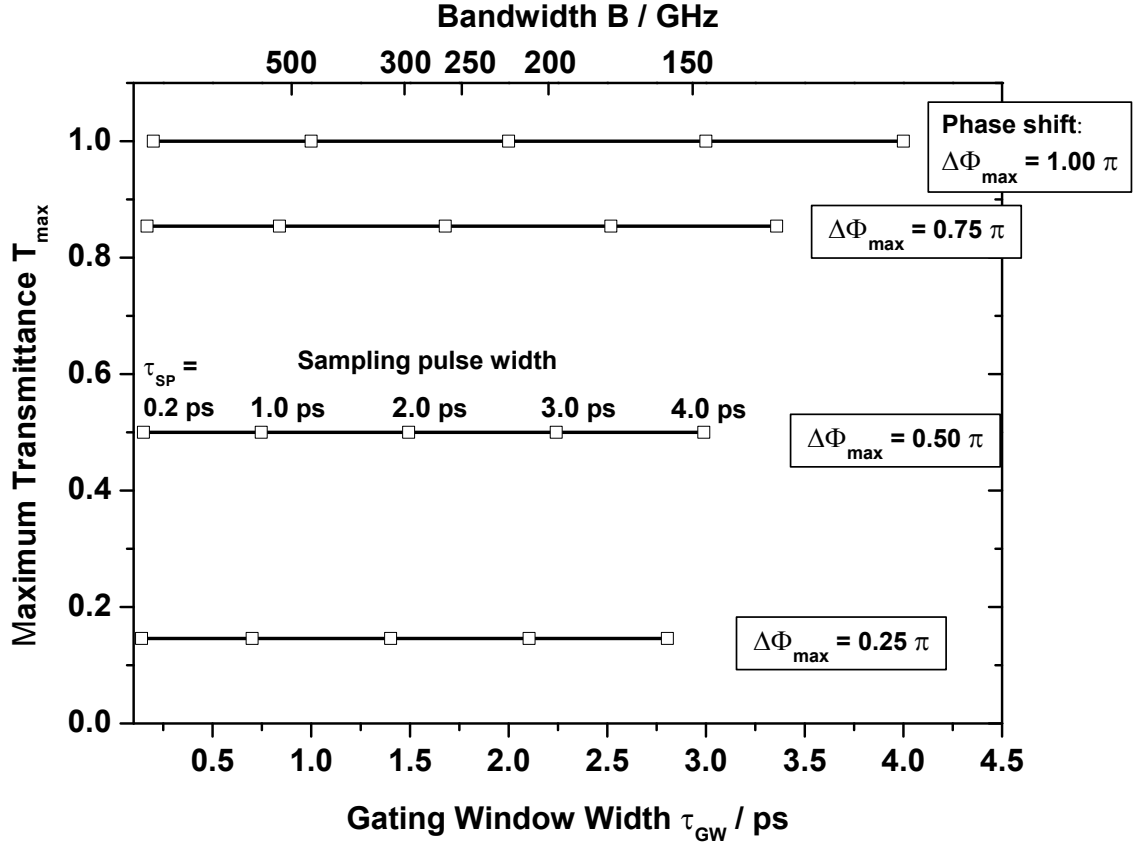


Figure 3.9: Calculated maximum transmittance  $T_{\max}$  as a function of the gating window width  $\tau_{\text{GW}}$  for the fiber based sampling gate. The parameters are the sampling pulse width  $\tau_{\text{SP}}$  and the maximum induced phase shift  $\Delta\phi_{\max}$ .

on the length  $L$  of the HNLF and the optical power  $P(t)$  of the control pulse. In a practical set-up, the fiber length is limited by temporal walk-off between the control and signal pulses due to chromatic dispersion. Therefore the dispersion profile should be flat in order to minimize the walk-off (see next subsection). The limiting factor for the control pulse power is the distortion of the control pulse shape due to self-phase modulation at high control pulse powers. This effect distorts the shape of the gating window via Eq. (3.9). Up to now there are no detailed experimental investigations on the maximum achievable phase shift in HNLF's.

Similar to Fig. 3.5, Fig. 3.9 shows distinct points along the traces. In contrast to the SOA based gate, in the HNLF based gate the gating window width is determined by the width of the sampling pulse itself. This can be seen from the trace for  $\Delta\Phi = \pi$ . In this case, the width of the gating window corresponds to the width of the sampling pulse, i.e.  $\tau_{\text{GW}} = \tau_{\text{SP}}$ . If the induced phase change is less than  $\pi$ , the maximum transmittance decreases and the gating windows are slightly narrower than the sampling pulse widths. The reason is the cosine shaped transfer function of the interferometer (Eq. (3.5)).

Eq. (3.7) and Fig. 3.9 reveal that HNLF based optical gates achieve optical bandwidths well above 500 GHz if sampling pulses with widths below 1 ps are used.

### Set-up of the NOLM

The set-up of the NOLM is schematically depicted in Fig. 3.10. It has the geometry of a Sagnac interferometer. The optical data signal was split into two components by a 50 % fiber coupler C1. The two components travelled along the fiber loop in opposite directions forming the two interferometer branches. After having passed the fiber loop, the two components interfered at the 50 % coupler C1 and because of the inherently equal optical path lengths in both interferometer branches, the data signal interfered constructively at the port from which the light was coupled into the loop. This configuration thus acts as mirror for the data signal. In order to switch the data signal to the output of the gate, another 50 % fiber coupler C2 was used to insert control pulses into the fiber loop. The control pulses were co-propagating with the clockwise propagating component of the data signal. If a control pulse overlapped a data pulse component that was travelling through the loop in the same direction, it induced a phase change in this pulse, whereas the counter clockwise propagating data signal component was almost not effected. Thus a phase difference between the two components of the data signal was realized by the control pulses. For a phase difference of  $\pi$ , the data signal interfered constructively at the data signal output port of the loop. A tunable optical bandpass filter was used at the output to suppress the control pulses. This interferometer is inherently phase stable because both interferometer branches use the same physical fiber but in opposite directions.

The NOLM that was used in the experiments comprised a piece of 320 m of HNLF. The HNLF had a nonlinearity coefficient of  $\gamma = 17 \text{ W}^{-1}\text{km}^{-1}$ . It was a dispersion flattened dispersion shifted fiber. The dispersion profile was not measured for the specific sample used in this work, but was similar to the one shown in Fig. 3.11, which is taken from Ref. [60] where the same type of HNLF was used for other experiments.

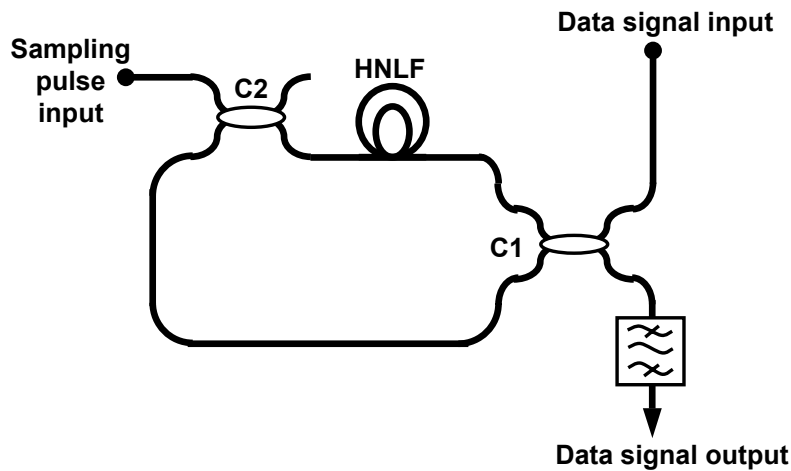


Figure 3.10: Set-up of the NOLM sampling gate.



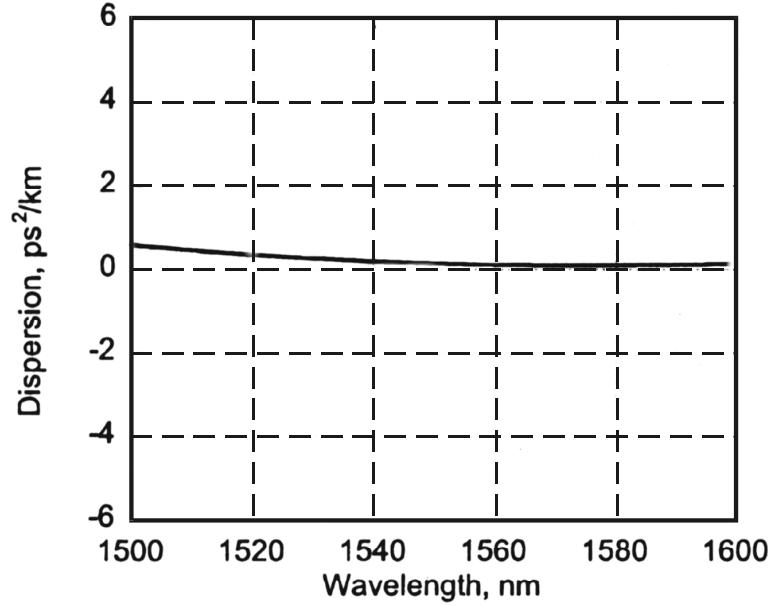


Figure 3.11: Dispersion coefficient  $\beta_2$  as a function of the wavelength for the type of HNLf used (after Ref. [60]).

Fig. 3.11 shows that the dispersion coefficient of the HNLf is almost zero over a wide wavelength range. This reduces the temporal walk-off between the sampling pulses and the data signal that propagate at different wavelengths through the HNLf. The use of such fiber is therefore beneficial in an optical sampling gate as will be discussed in Sec. 4.2. For comparison, the dispersion coefficient of standard single mode fiber is  $\beta_{2,SMF} \approx -21 \text{ ps}^2/\text{km}$ . The figure also reveals that the dispersion coefficient of the HNLf is almost constant over a wide wavelength range. This means that the third order dispersion coefficient  $\beta_3$  (or the dispersion slope  $S$ ) of the fiber is negligible.

## 3.2 Sampling Pulse Source

The all-optical gates described in Sec. 3.1 need short optical sampling (control) pulses. While the bandwidth of the GT-UNI gate was influenced by the flanks of the sampling pulse and the delay  $\Delta t$  between the two phase curves, the gating window in the NOLM gate was mainly determined by the shape and duration of the sampling pulse. As a direct consequence, the sampling pulse source should produce pulses with durations of about 1 ps in order to generate an optical bandwidth of the sampling system of 200-300 GHz.

Another important requirement for the optical pulse source is its phase stability or timing jitter, because the sampling pulse triggers the sampling events and thus determines the phase stability or jitter of the complete sampling system. Last but not least, the pulse source should be a compact device which is easy to handle.

This section describes the optical pulse source which was used in this work. The

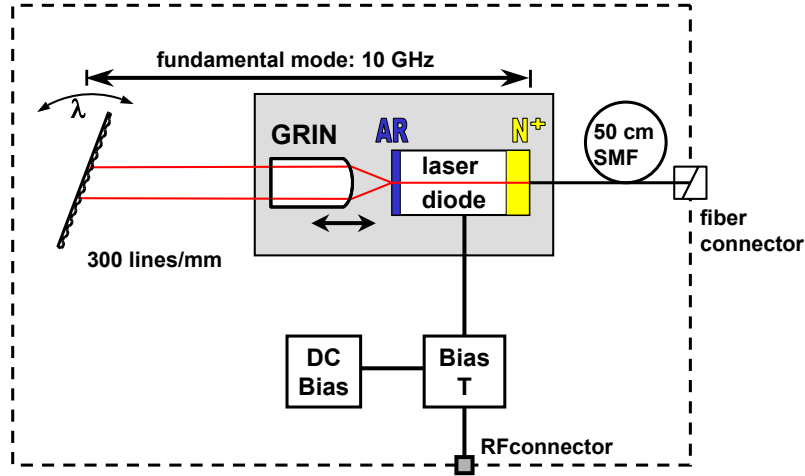


Figure 3.12: Schematic of the set-up of the optical pulse source.

emphasis of the discussion is on the two aforementioned features pulse width and timing jitter.

### 3.2.1 Set-up of the TMLL

The optical sampling system presented in this work uses a semiconductor mode-locked laser with an external cavity. The set-up of the pulse source (tunable mode-locked laser, TMLL) [61, 62] is schematically depicted in Fig. 3.12. The laser is based on a commercially available semiconductor laser diode. One facet of the laser chip was coated with an antireflection coating (AR). The light from this facet was collimated by a micro lens with graded refractive index profile (GRIN). The collimated beam was directed to a surface grating, which acted as cavity mirror. The reflected light from this mirror was coupled back into the laser diode again and was reflected on the second chip facet (right facet in Fig. 3.12). Thus a laser resonator was formed between the grating and the uncoated facet of the laser diode. At this facet a saturable absorber was generated by bombarded with nitrogen ions (N<sup>+</sup>) [63]. The laser radiation of pulse source was coupled from the right chip facet into a short piece (50 cm) of tapered standard single mode fiber (SMF) with a fiber connector at its end. The average output power of the pulse source was about -5 dBm at the output fiber connector.

The laser was operated using hybrid mode-locking in order to synchronize it to an external reference. Therefore, an electrical RF-signal was applied to the laser diode in addition to the DC-current (DC-bias) using a bias-T. If the round trip time in the laser resonator was close to the inverse of the RF-frequency, the generated optical pulses were synchronized to the RF-frequency and showed low timing jitter.

The pulse width of the pulses was determined by the relaxation time of the saturable absorber as well as the spectral selectivity of the surface grating which acted as wavelength selective cavity mirror. A higher spectral selectivity, i.e. a high number of lines per unit length led to a larger pulse width because the fed back optical spectrum was decreased. In this work, a grating with 300 lines/mm was used in the optical

pulse source.

For the measurements reported in this work, two different versions of the optical pulse source were used. One pulse source provided optical pulses at a wavelength near 1300 nm for the GT-UNI gate, while the other one provided optical pulses in the 1550 nm region for the NOLM gate. The wavelength of the TMLL was determined by the laser diode and the grating. Thus the two lasers used different laser diodes with different gain maximums, namely one at 1310 nm and one at 1550 nm wavelength. Within the spectral gain region of the laser diode, which was typically about 60-100 nm wide, the emission wavelength could be tuned by tilting surface grating in the resonator. The following subsections describe the spectral properties of the two pulse sources.

### Pulse Source #1 (1310 nm)

This pulse source was used for the experiments with the GT-UNI sampling gate. Due to the gain-transparent principle of this sampling gate, the pulse source comprises from a 1300 nm laser diode. Fig. 3.13 shows the optical spectrum at the output of the pulse source. The emission wavelength of this pulse source was 1306 nm and the spectral width of the pulses was 2.41 nm which corresponded to an optical bandwidth of 242 GHz. The inset shows a fine structure of the pulse spectrum with 10 GHz (0.06 nm) spacing, which corresponded to the repetition frequency of the laser pulses. The slight undulation which is visible mainly on the short wavelength flank of the envelope of the spectrum had a frequency of 143 GHz (0.81 nm) and was due to an imperfect AR-coating of the left (Fig. 3.12) chip facet. The imperfect coating led to a second reflection point for the light inside the laser resonator which generated a second resonator with a shorter length. The result were trailing pulses which appeared

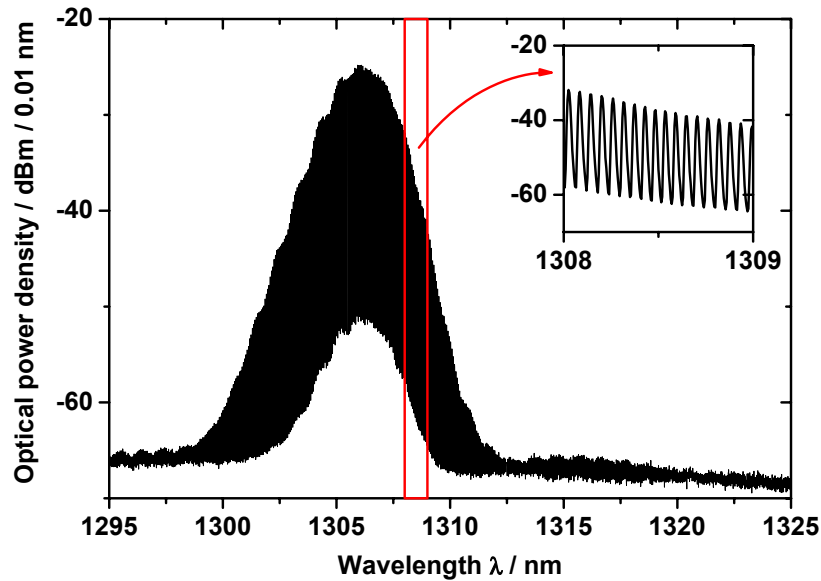


Figure 3.13: Optical spectrum of a 10 GHz pulse train from pulse source #1.

after the main pulses at a distance given by the round-trip time inside this shorter resonator. The undulation frequency on the spectrum corresponds to the inverse of the round-trip time of 7 ps in this shorter resonator, which was formed by the chip facets. The amplitude of the trailing pulses was however more than 20 dB below the main pulse amplitude so that the trailing pulses were negligible in the sampling system.

### Pulse Source #2 (1552 nm)

This pulse source was used for the experiments with the NOLM sampling gate. Due to the wavelength requirements of the NOLM sampling gate, the pulse source comprised a 1550 nm laser diode. The emission wavelength of this laser was set to 1552 nm. The spectral width and trailing pulse suppression of this pulse source was similar to the other pulse source.

### 3.2.2 Pulse Width and Pulse Compression

In order to characterize the pulse shape and width of the generated optical pulses, the autocorrelation trace was measured. The result is shown in Fig. 3.14 for pulse source #1. Assuming a  $\text{sech}^2$  shape of the generated pulses, a fit to the autocorrelation trace yields an almost perfect agreement with the measured data. From the fit, a pulse width of  $\tau_{SP} = 1.2$  ps (FWHM) was found. Looking back to Fig. 3.5 one finds that this pulse width should be sufficient to generate gating windows with widths of  $\tau_{GW} = 1.7$ -2.7 ps which corresponds to a bandwidth of the sampling system of 150-250 GHz.

However, for a target bandwidth of 250-300 GHz, the pulse width should be below 1 ps. In the set-up of the pulse source this would be possible by choosing a grating with less spectral selectivity, i.e. less number of lines per mm. Unfortunately experiments

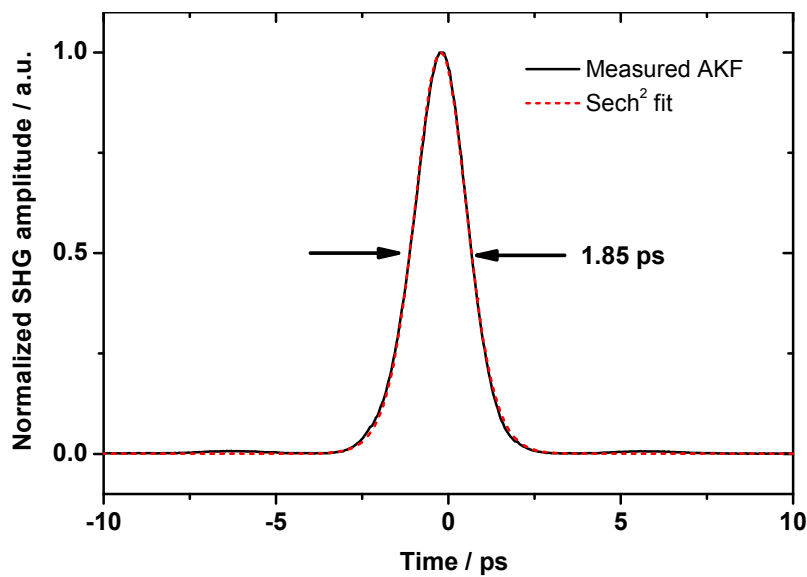


Figure 3.14: Autocorrelation trace of pulses from pulse source #1.

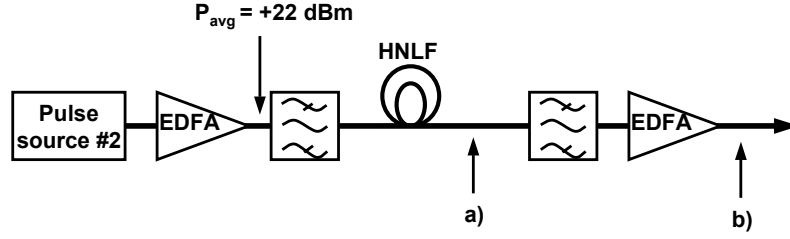


Figure 3.15: *Experimental set-up for the compression of the sampling pulses from pulse source #2.*

showed, that this method leads to a significant increase in timing jitter of the generated pulses [64], which was not tolerable in the optical sampling system.

Another way of generating short pulses is compression of the initially broad pulses by means of nonlinear processes, for example supercontinuum generation [65]. This was adopted in the optical sampling system based on the NOLM gate which was using the 1.5  $\mu\text{m}$  pulse source. Fig. 3.15 shows the experimental set-up for the pulse compression technique. The generated pulses from pulse source #2 were amplified to an average power of +22 dBm using a high power Erbium doped amplifier (EDFA). An optical bandpass filter was used to suppress the amplified spontaneous emission of the EDFA. The amplified pulses were then sent through a highly nonlinear fiber (HNLF). While propagating through the HNLF, the pulse spectrum broadened due to self-phase modulation (SPM). Due to the high nonlinear coefficient of the HNLF, the broadening resulted in a supercontinuous spectrum as shown in Fig. 3.16a. Using a suitable optical bandpass filter, it was possible to filter out a spectrum broader than the input spectrum (Fig. 3.16b), which resulted in a compressed pulse train with a pulse width which was given by the new spectral width of the pulses. Fig. 3.16b shows the optical spectrum for a 6 nm broad bandpass filter. With this filter, the output pulses were compressed to 0.7 ps as measured by autocorrelation measurements (Fig. 3.17).

From Fig. 3.16 it becomes also clear that this pulse compression technique allows for a simultaneous wavelength shifting of the sampling pulses, because the sampling wavelength is given by the wavelength of the bandpass filter which can be placed anywhere within the generated supercontinuum [66]. This feature of the pulse compressor was used for the experiments described in Sec. 5.2, where the sampling pulse wavelength was shifted to 1560 nm. The corresponding pulse spectrum is shown in Fig. 3.16c. In this case, a bandpass filter with 3.2 nm bandwidth was used to generate 1.5 ps wide sampling pulses.

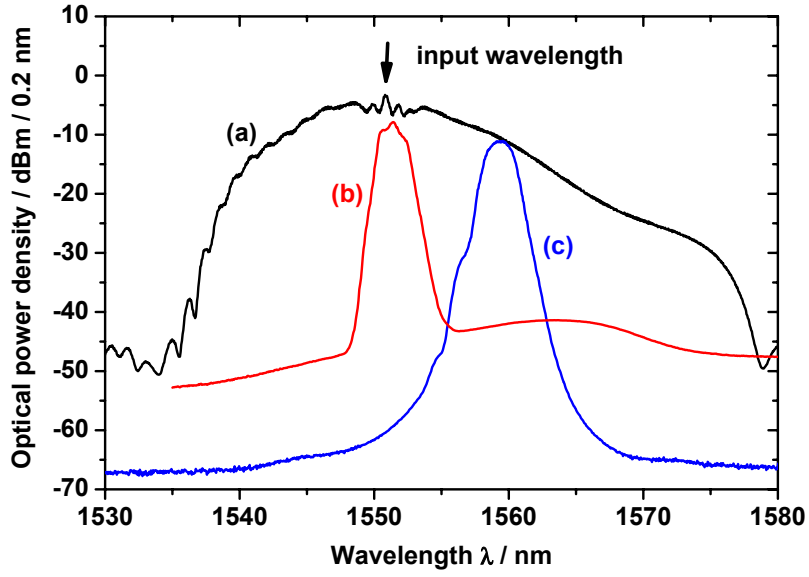


Figure 3.16: Optical spectra in the pulse compressor after the HNLF (a) and after the filter (b) and (c).

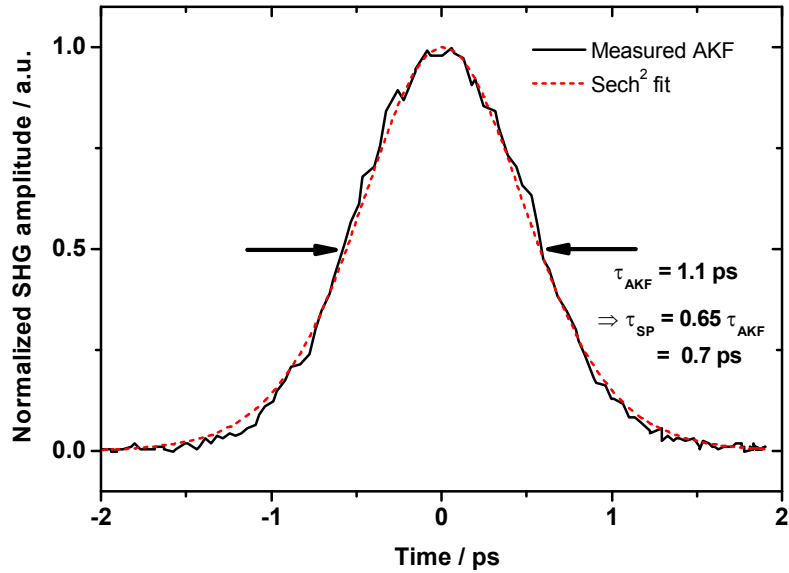


Figure 3.17: Autocorrelation trace of compressed sampling pulses for the case of a 6 nm filter.

### 3.2.3 Timing Jitter

The jitter of an optical sampling system is given by the jitter of the sampling pulse source, since the pulse source determines the temporal precision of the optical sampling process. To measure data signals with a picosecond resolution, a total timing jitter of the sampling system of less than 500 fs is necessary.

Usually, the timing jitter of optical or electrical signals is measured using a digital oscilloscope and by measuring the horizontal histogram on one flank of the signal. The standard deviation of the statistical distribution described by the histogram is the so called RMS timing jitter. This method is however limited by the internal jitter of the oscilloscope time base to about 200 fs [67].

To extend the measurement range to lower jitter values, a measurement technique by von der Linde [68] is well established, especially for mode-locked lasers at telecommunication frequencies of a few GHz up to 40 GHz. With this technique, one measures the so called "single sideband phase noise" (SSB-noise) of the signal around its carrier and calculates the RMS timing jitter from the measured data. The measurement is done using an electrical spectrum analyzer to which a fast photodetector is connected. Since the detection of the signal by a photodetector involves squaring of the optical field, it becomes however impossible to distinguish between amplitude and phase noise in the spectrum. Thus, this method is only valid if amplitude noise contributions can be neglected.

Fig. 3.18 shows the measured single sideband phase noise  $L(f_m)$  of the sampling pulse sources in units of dBc/Hz as a function of the offset frequency  $f_m$  from the repetition frequency  $f_c$  of the laser. The SSB-noise of the driving electrical RF signal is also shown for comparison. One finds three regions in the SSB-noise curves [69]. In region 1, which roughly covers the frequency range from 10 Hz to 1 kHz, the phase

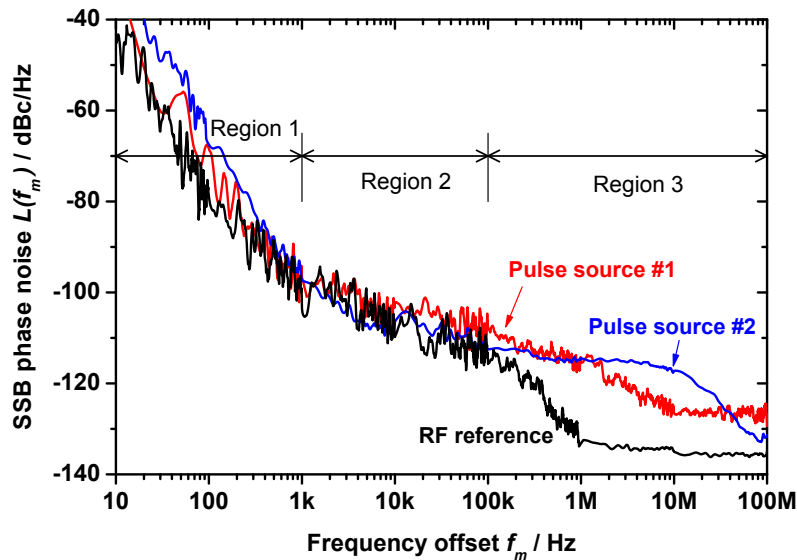


Figure 3.18: Single sideband phase noise of the sampling pulse sources.

noise measurement was limited by the internal phase noise of the electrical spectrum analyzer used. This internal noise varies for different analyzer settings, which is the reason why the three traces are not identical in this region. A second region can be identified from 1 kHz to 100 kHz. In this region, the phase noise of the pulse sources followed the phase noise of the RF reference signal. For offset frequencies  $>100$  kHz (region 3), the phase noise showed an individual behavior for each pulse source and the RF reference signal. Finally, in region 3 the noise floor of the spectrum analyzer is reached. The noise floor depends on the dynamic range of the spectrum analyzer and signal power that is applied. For the measurement of the reference signal, the noise floor of the spectrum analyzer was -135 dBc/Hz and was reached at an offset frequency of 1 MHz. For pulse source #1, the noise floor was reached at 10 MHz with -125 dBc/Hz, because the dynamic range of the spectrum analyzer was not fully used in this measurement. Finally, for pulse source #2 the noise level was reached at an offset frequency of 100 MHz.

From the measured SSB-noise curves, the RMS timing jitter can be calculated using the following equations [70]:

$$\varphi_{RMS} = \sqrt{2} \sqrt{\int_{f_a}^{f_b} L(f_m) df_m} \quad (3.10)$$

$$\tau_{RMS} = \frac{1}{f_c} \frac{\varphi_{RMS}}{2\pi} \quad (3.11)$$

where  $\varphi_{RMS}$  is the RMS timing jitter in units of radians and  $\tau_{RMS}$  is the RMS timing jitter in units of seconds.

Thus the RMS timing jitter is obtained by integrating the single sideband phase noise. Ideally, the integration range should be between  $f_a = 0$  Hz and  $f_b = f_c/2$ . Practically, the lower integration limit is determined by the finite resolution bandwidth of the spectrum analyzer and the upper integration limit is given by the noise floor of the spectrum analyzer. For typical spectrum analyzers, the integration range is between 100 Hz and 10 MHz offset frequency. Please note that one has to be careful when comparing RMS jitter values measured with this technique since the integration might contain areas which are limited by the spectrum analyzer itself. For example, the integration over region 1 in Fig. 3.18 yields different values for the different curves but the result is completely governed by the spectrum analyzer itself. In a similar manner, integration from 1 MHz to 10 MHz for the RF reference curve yields a value which is higher than the actual signal noise because the spectrum analyzer's noise level is already reached. Keeping these limitations in mind, the integration only yields an estimate of the timing jitter of the signal. When comparing two different signals it is more suited to compare the shape of the SSB-noise curves rather than the calculated RMS jitter values.

With an integration range of 100 Hz to 10 MHz the RMS jitter of sampling pulse source #1 becomes  $\tau_{RMS} = 100$  fs. For sampling pulse source #2, the value becomes  $\tau_{RMS} = 140$  fs. For comparison, the jitter of the RF reference signal is  $\tau_{RMS} = 40$  fs.

These jitter values show that the pulse sources used were well suited for the application in the optical sampling system because they can exhibit jitter values of less than 150 fs. It should be noted however, that especially in region 2 of the SSB-noise



curves, the jitter of the pulse source is determined by the jitter of the RF reference signal. In the optical sampling system, this reference signal is generated by the optical clock recovery. Thus if the recovered clock signal contains a larger jitter, then the sampling pulse source will perform accordingly and also show a larger jitter.

### 3.2.4 Reduction of Sampling Pulse Repetition Rate

In the optical sampling system, each individual sampling pulse generates one individual optical sample. Each optical sample in turn is proportional to the signal amplitude at a single time instant. The speed at which the generation of samples takes place is called "sampling frequency". Since the peak value of each individual sample has to be measured by the O/E detection unit, the sampling frequency must not be higher than the acquisition speed of the detection unit. Using commercial A/D converter boards, this limits the sampling frequency to a few tens of Megahertz. In commercial electrical sampling oscilloscopes the sampling frequencies are even lower and are in the order of a few hundred Kilohertz. The A/D converter used in this work had a maximum acquisition speed of 500 MHz (see Sec. 3.5). The optical pulse source described in Sec. 3.2 however had a repetition rate of about 10 GHz. In order to meet the requirements imposed by the A/D converter, a reduction of the repetition rate was necessary.

One way of reducing the repetition rate of the sampling pulse source to a value below 500 MHz is to increase the resonator length of the pulse source by moving the surface grating (see Fig. 3.12) away from the semiconductor chip. The resonator length would have to be increased from about 1 cm for 10 GHz to about 50 cm in that case. Unfortunately, experiments showed that this results in an unstable operation of the pulse source because the larger cavity is more sensitive to environmental changes like temperature and vibration. Also, the pulse sources showed larger jitter at lower repetition rates. Therefore, another solution was applied and the repetition rate was reduced externally.

The external reduction of the repetition rate was achieved by passing the sampling pulses through an optical amplitude modulator. In the modulator, only every  $n$ -th pulse was allowed to pass while all other pulses were suppressed. Fig. 3.19 shows the corresponding set-up including the pulse source and the subsequent amplitude modulator. The pulses from the pulse source were amplified and fed into a Mach-Zehnder LiNbO<sub>3</sub> modulator. A polarization controller was needed to adjust the input polarization into the modulator since the device was polarization dependent. The modulator was operated in push-pull mode, which means that it was driven by two electrical signals (a1) and (a2). These signals were generated in the clock processing block (see Sec. 3.4). Each signal was applied to one electrode of the modulator. Fig. 3.20 shows schematically the modulator signals (a1) and (a2). Both signals were square wave signals with a frequency of 155.53 MHz. The signals were temporally offset with respect to each other by about 70 ps. By applying a DC bias voltage to both modulator electrodes it was possible to bias the modulator such that its optical transmission function (a) was given by the XOR correlation of the two signals (a1) and (a2). The result was a transmission function which had a width of about 70 ps and whose flanks were given by the rise and fall times of the signals (a1) and (a2),

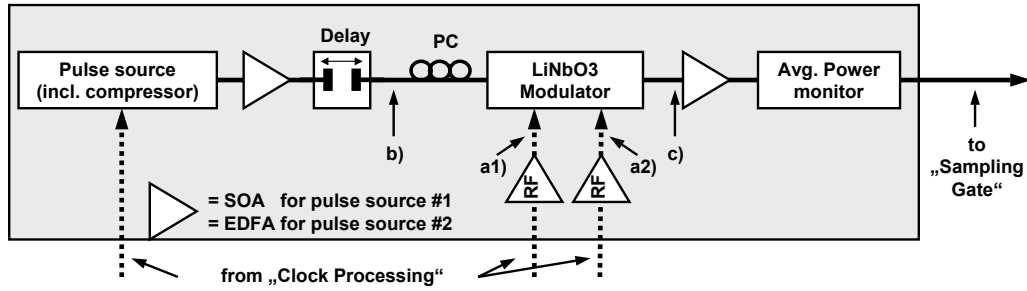


Figure 3.19: Complete set-up of sampling pulse source building block. The compression stage was only included in conjunction with pulse source #2. The different signals at the positions indicated by (a) - (c) are shown in Fig. 3.20.

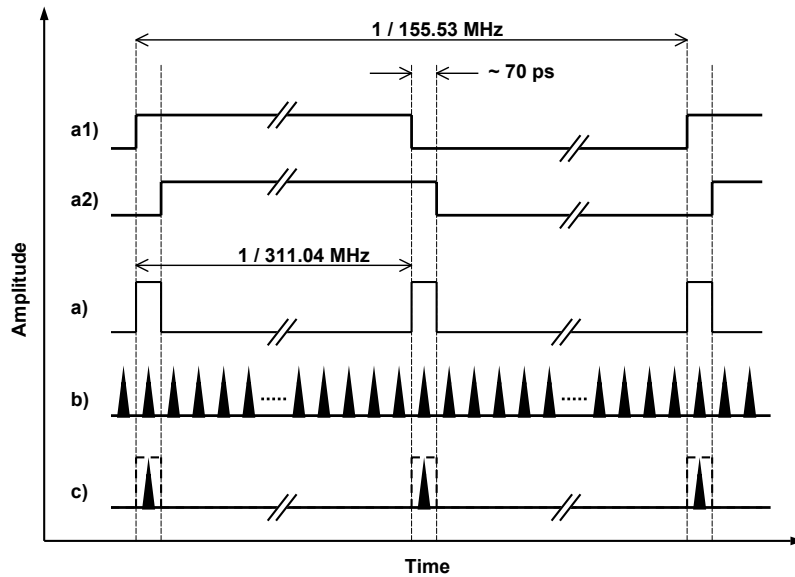


Figure 3.20: Schematic description of the signalling for the external repetition rate reduction. The labels (a) - (c) correspond to different positions in the set-up (see Fig. 3.19).

which were less than 50 ps. Please note that the modulator transmission window was generated for every flank of the signals (a1) and (a2) and thus had twice the frequency of the modulator signals.

The optical delay line shown in Fig. 3.19 was used to align the optical pulses (b) with the transmission window (a) of the modulator such, that only one single pulse from the pulse source was in the transmission window whereas the remaining pulses were suppressed (c). The extinction ratio of the modulator was measured to be 15 dB using cw-light. This was the ratio between the average transmission in the on-state as compared to the average transmission in the off-state.

Finally, the sampling pulses were amplified again to compensate for the loss of

the modulator and the average optical output power was monitored using an inline power meter. The average optical power measured at this point will be referred to as "sampling pulse power"  $P_S$  for the rest of this work.

### 3.3 Clock Recovery

In the previous sections it was assumed that the electrical RF clock signal of the data signal was present and could be used to synchronize the sampling pulse source. While this may be the case in a laboratory environment where the optical sampling system is connected directly to an optical transmitter, it will in general not be the case. Thus in order to use an optical sampling system for practical applications, the system must include a clock recovery that is capable of recovering/extracting the electrical clock signal from the data signal. This section describes the two configurations that were used in this work.

#### 3.3.1 Electrical Clock Extraction

The simplest way to extract the electrical clock signal from the optical data signal is to detect the data signal with a fast photodetector and then send it through an electrical bandpass filter with a high finesse. If the clock line is present in the electrical spectrum of the data signal like in the case of an RZ modulated signal, the filter extracts it from the data signal. This type of clock extraction is schematically shown in Fig. 3.21.

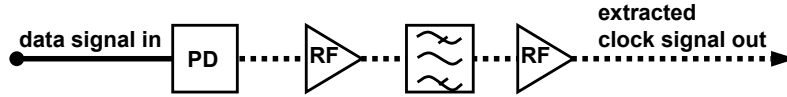


Figure 3.21: Set-up of the clock extraction circuit. The solid line indicates the optical path. The dotted line indicates electrical signal.

This scheme however is limited by the available electronic components, since the bandwidth of the photodetector must be high enough to detect the clock frequency of the signal. Moreover, amplifiers as well as a bandpass filter with high finesse at the clock frequency are needed. For an STM-64 data signal with a clock frequency of 9.95328 GHz, those components were available and the set-up shown in Fig. 3.21 was used. This set-up will be referred to as "clock extraction" circuit later on.

#### 3.3.2 Optical Clock Recovery

For data signals with data rates higher than 40 Gbit/s, it is not possible today to extract the frequency of the signal, since no electronic components like amplifiers and filters are available at such high frequencies. However, by using a prescaled optical clock recovery it is possible to extract a sub-harmonic of the frequency of the data

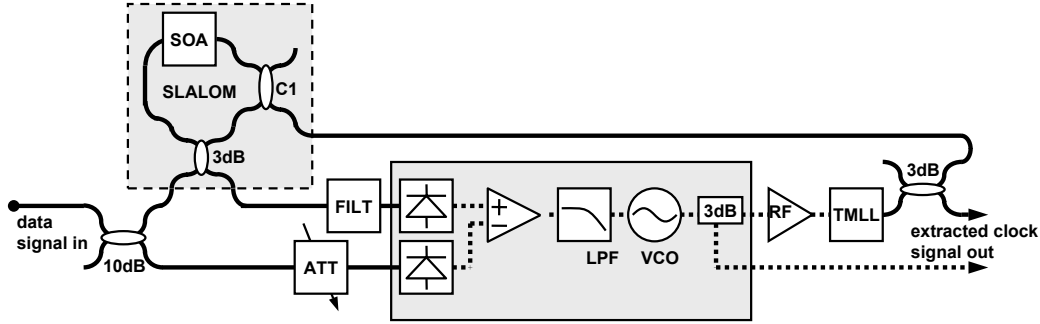


Figure 3.22: Schematic of the set-up of the optical clock recovery.

signal. The extracted subharmonic frequency  $f_{clock}$  is then commonly referred to as "clock frequency" of the data signal. It is related to the data signal frequency  $f_S$  by

$$f_{clock} = \frac{1}{p} f_S \quad (3.12)$$

where  $p$  is the prescaling factor. Such a clock recovery is not only needed in an optical sampling system, but is an essential component in a receiver [71] or 3R-regenerator to realize future optical time-division multiplexed (OTDM) transmission systems. In such systems, the prescaling factor is typically chosen to be  $p = d$ , i.e. it is equal to the multiplexing factor  $d$  of the OTDM data signal.

Among the many methods proposed and demonstrated so far, a phase-locked loop (PLL) with an optical or optoelectrical phase comparator is a promising method especially for subharmonic clock extraction from data signals beyond 100 Gbit/s [72, 73, 74]. In this work, a prescaled clock recovery by an optical phase locked loop using an SOA-based interferometric optical switch was used [75, 76]. The optical phase comparator was a semiconductor laser amplifier in a loop mirror (SLALOM) [77]. The optical clock recovery was designed to extract a subharmonic clock frequency with a frequency of about 10 GHz. Following Eq. (3.12), this means that for a 160 Gbit/s data signal the prescaling factor was  $p = 16$ .

Fig. 3.22 shows the set-up of the clock recovery. The operation principle is as follows: The data signal was coupled into the SLALOM, which was driven by an optical control pulse train generated by a semiconductor mode-locked laser (TMLL). The set-up of the laser was identical to the sampling pulse source described in detail in Sec. 3.2. The repetition frequency of the laser was controlled by a voltage controlled oscillator (VCO) to which the laser was hybridly mode-locked. The output signal of the SLALOM was detected by a slow photodiode having a bandwidth of about 100 MHz. With the repetition rate of the control pulses, parts of the input signal were continuously switched to the SLALOM output. When the frequency of the VCO was equal to the 10 GHz clock frequency of the input signal, the switched parts of the input signal were with constant phase in the time slot. Therefore, the output signal of the slow photodiode (called "error signal" hereafter) became a DC signal in principle with the signal amplitude depending on the phase difference between the

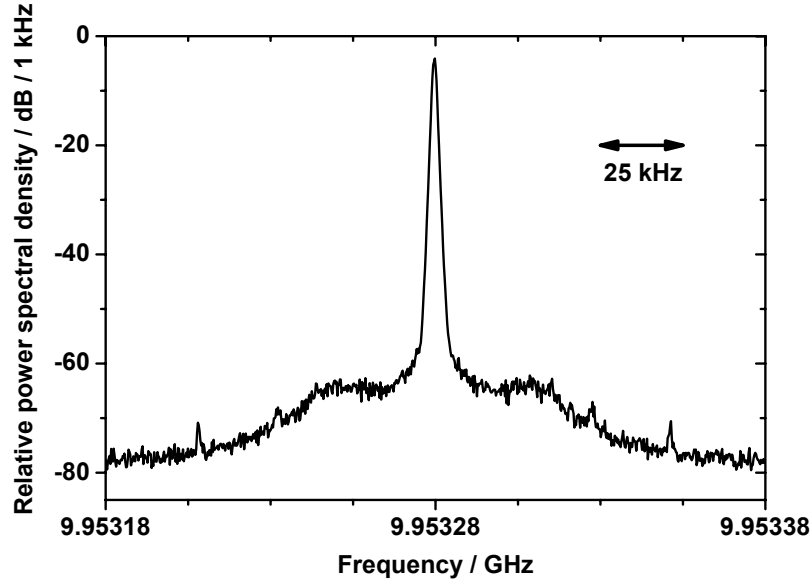


Figure 3.23: *RF spectrum of the recovered electrical 10 GHz clock signal from the optical 160 Gb/s data signal.*

input signal and the train of the control pulses. Thus the optical switch operated as a phase comparator. For an optical or optoelectrical phase comparator however, it is a well-known problem that the error signal has only one polarity due to the squaring O/E detector. To overcome this problem, the input signal was also detected by a second slow photodiode. The output signal of this photodiode was electrically subtracted from the error signal [73]. Then, the signal was supplied to the VCO to control its frequency after low pass filtering (LPF). This closed the loop and locked the frequency of the VCO to the clock frequency of the input data signal. Note that there was no need for any initial phase adjustment as described in [78] for this setup.

The SLALOM was realized in two different ways in this work. In the first version, which will be called "conventional" SLALOM, the SOA in the SLALOM had its gain peak in the 1.55- $\mu\text{m}$ -wavelength range and the emission wavelength of the TMLL was 1540 nm. The input power of the control pulses was about +5 dBm. The filter (FILT) was a bandpass filter which was centered around the wavelength of the data signal. The coupler C1 was a 3dB coupler. In the second version, called the "gain-transparent" SLALOM, the SOA had its gain peak around 1300 nm and a TMLL with an emission wavelength of 1310 nm was used. In that case, the filter "FILT" and the coupler "C1" were WDM-couplers. In both cases, the width of the gating window of the SLALOM was about 11 ps. Although this value was larger than one bit slot of the 160 Gbit/s data signal, it did operate well [79].

After setting the VCO frequency almost equal to the base-rate frequency without a data signal at the input, the OTDM data signal was injected and the attenuator was optimized to get the PLL locked. The locking was stable for input data rates of 40, 80 and 160 Gb/s. Within several hours, no problems in locking were encountered. Fig. 3.23 shows the electrical spectrum around the extracted clock frequency of the

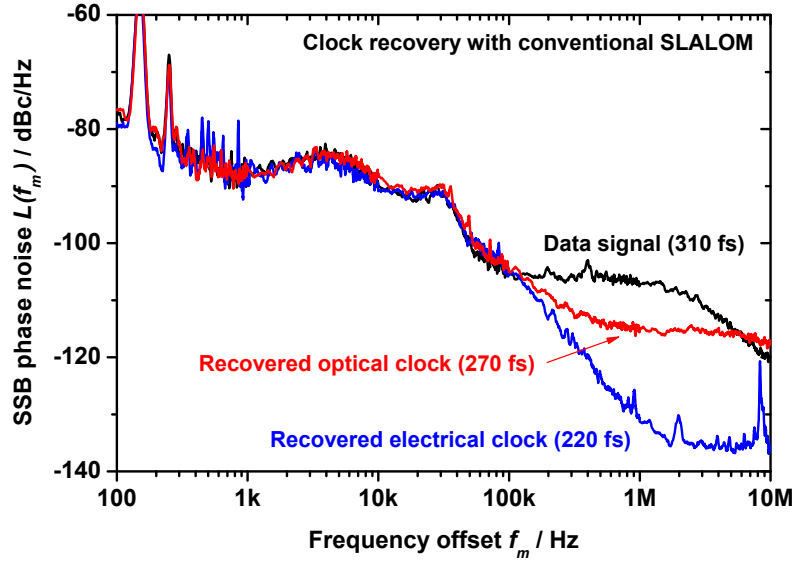


Figure 3.24: SSB-noise of the data signal and the recovered optical and electrical 10 GHz clock signal for the clock recovery with conventional SLALOM.

recovered optical clock pulses for the "conventional" SLALOM. It can be seen that the carrier to noise ratio was below -85 dBc/Hz at 10 kHz frequency offset.

Fig. 3.24 shows the single sideband phase noise for the "conventional" SLALOM. It can be seen that for both the recovered electrical and optical clock signal the phase noise curves followed the curve of the input data signal up to an offset frequency of about 100 kHz. Above 100 kHz the electrical clock signal dropped with 20 dB/decade down to the noise level of the spectrum analyzer of about -135 dBc/Hz. The optical clock signal decreased to -115 dBc/Hz although the data signal had a phase noise of -105 dBc/Hz at 1 MHz offset frequency. Integrating between 100 Hz and 10 MHz (see Sec. 3.2.3), the RMS jitter of the recovered optical clock was 270 fs for an input signal with a PRBS word length of  $2^7 - 1$  and 290 fs for a word length of  $2^{31} - 1$ .

For the experiments in Sec. 5.3.1, the "gain-transparent" version of the clock recovery was used. This was done because in that case the recovered optical clock at 1.3  $\mu\text{m}$  was used directly as control signal for the optical demultiplexer. Fig. 3.25 shows the SSB-noise curves for the recovered optical clock together with the optical data signal for this experiment. Please note that the phase noise of the data signal was significantly lower in this experiment as compared to the data in Fig. 3.24. The reason for this was the use of a different RF source in the 10 Gbit/s transmitter. However, despite the lower phase noise of the data signal, the recovered optical clock signal shows almost the same behavior in this case. This shows that the phase noise of the recovered optical clock was mainly limited by the electrical feedback loop of the clock recovery up to an offset frequency of about 100 kHz. Above 1 MHz the phase noise measurement was again limited by the noise level of the electrical spectrum analyzer, which varied around -115 dBc/Hz for these measurements depending on the input power into the spectrum analyzer (see Sec. 3.2.3). Since the noise level was

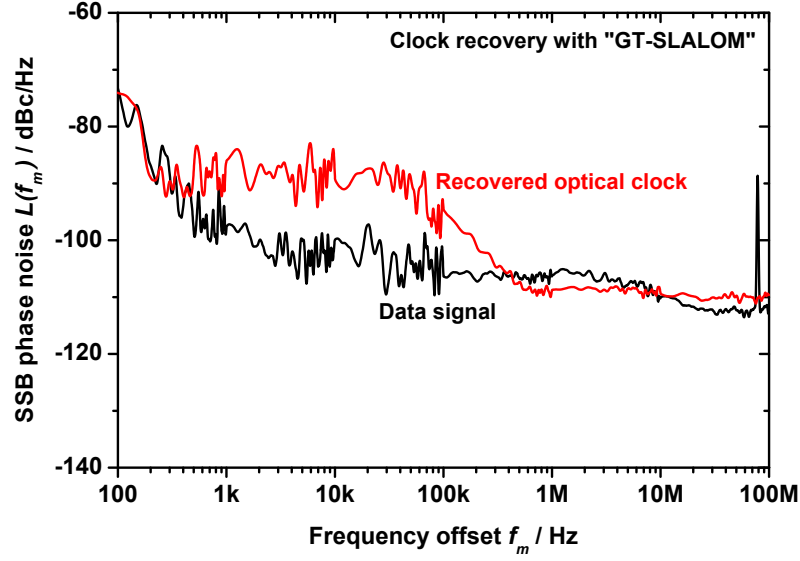


Figure 3.25: SSB-noise of the recovered optical clock and the data signal for the GT-SLALOM clock recovery.

reached already at 1 MHz in these measurement, it did not make sense to integrate up to 10 MHz as usual to derive the timing jitter of the signal. Instead, the roll-off between 100 kHz and 1 MHz was extrapolated which yielded an estimation for the jitter of about 300 fs.

### 3.4 Clock Processing

Using the clock recovery described in the previous section, the (subharmonic) clock frequency  $f_{clock} \approx 10$  GHz of the signal under investigation was extracted. However, in order to scan over the signal under investigation, the optical sampling gate had to be operated at a frequency  $f_G$  which was offset from  $f_S$  (see Sec. 2.1). The purpose of the clock processing unit was to generate the required gating frequency as well as all other timing signals within the optical sampling system.

The block diagram of the clock processing unit is shown in Fig. 3.26. The input signal was an electrical sine wave at the extracted subharmonic signal clock frequency  $f_{Clock} = 9.95328$  GHz. This signal was divided by the factor  $N$  to generate the offset frequency  $\Delta f$ , by which the signal clock frequency was shifted (see Eq. (2.4)). The resulting frequency  $f_{Laser}$  was used to synchronize the laser pulse source in the sampling pulse source unit.

In order to achieve a reduction of the sampling frequency as described in Sec. 2.1, the shifted frequency  $f_{Laser}$  was divided by a factor  $2M$ . This was the driving signal  $f_{MOD}$  for the modulator within the sampling pulse unit that was used for the external sampling pulse rate reduction (see Sec. 3.2.4). Additionally, the frequency  $f_{Laser}$  was divided by a factor  $M$  to generate the clock frequency  $f_{AD-Clock}$  for the A/D-converter

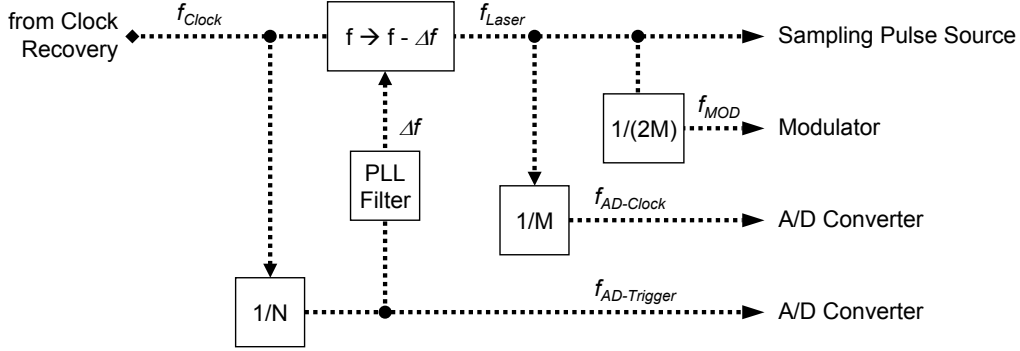


Figure 3.26: Block diagram of clock processing unit.

in the O/E-detection unit. This frequency was the actual gating frequency  $f_G$ .

In this work, the divisors were chosen as  $N = 32^3$  and  $M = 32$ . This yields the following values for the frequencies generated by the clock processing unit:

$$f_{Clock} = 9.953280000 \text{ GHz} \quad (3.13)$$

$$\Delta f = \frac{f_{Clock}}{N} = 303.750 \text{ kHz} \quad (3.14)$$

$$f_{Laser} = f_{Clock} - \Delta f = 9.952976250 \text{ GHz} \quad (3.15)$$

$$f_{AD-clock} = \frac{f_{Laser}}{M} \cong 311.03 \text{ MHz} \quad (3.16)$$

$$f_{AD-Trigger} = \Delta f = 303.750 \text{ kHz} \quad (3.17)$$

$$f_{MOD} = \frac{f_{Laser}}{2M} \cong 155.52 \text{ MHz} \quad (3.18)$$

Following Eq. 2.12, the number of samples  $k$  was

$$k = \frac{N - 1}{M} = \frac{32^3 - 1}{32} \cong 1023.97 \quad (3.19)$$

and the time step between two samples was:

$$\Delta\tau = \frac{1}{f_{clock} \cdot S} \cong 98.1 \text{ fs} \quad (3.20)$$

This value was used to scale the X-axis of the measured eye diagrams.

The following sections describe the frequency shifting unit as well as the generation of the divided signals in more detail.

### 3.4.1 Frequency Shifting

The frequency shifter was needed to shift the extracted clock signal from the clock recovery ( $\sim 10$  GHz) by a small amount  $\Delta f \cong 300$  kHz. This frequency shift was rather small compared to the carrier frequency. To achieve such function, one can



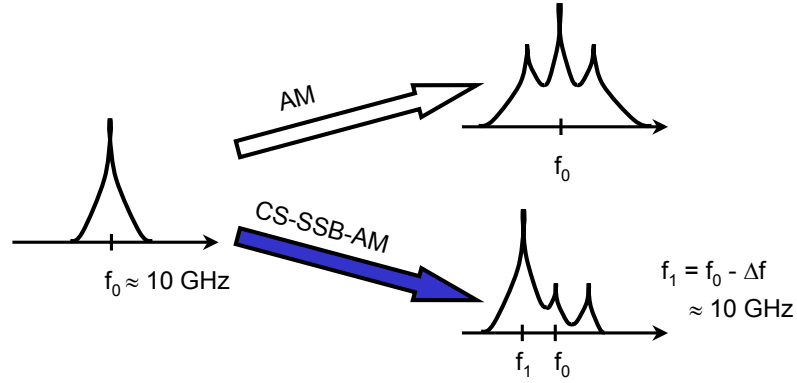


Figure 3.27: Principle of amplitude modulation (AM) and carrier suppressed single sideband amplitude modulation (CS-SSB-AM).

use a PLL-circuit, in which the VCO signal and the reference signal are divided by slightly different ratios and then the phase comparison is performed at a lower frequency. However, such circuit requires a very low jitter VCO, which was hard to realize at 10 GHz.

Therefore, in this work the frequency shifting was realized in a more simple way using a single sideband amplitude modulation technique with suppression of the carrier (Fig. 3.27). This is a standard technique in radio frequency electronics. In the conventional amplitude modulation (AM) technique, a carrier at the frequency  $f_0$  is amplitude modulated with a modulation frequency  $\Delta f$ , which leads to two sidebands around the carrier. The sidebands are separated from the carrier by the modulation frequency  $\Delta f$ . In the carrier suppressed single sideband amplitude modulation technique (CS-SSB-AM), one of the generated sidebands and the carrier itself are suppressed.

One way to realize the CS-SSB-AM is the so called "phase method" [80, 81]. This technique was employed using a commercially available image rejection mixer as shown in the set-up in Fig. 3.28. The image rejection mixer was a Mach-Zehnder-Interferometer for the RF input signal. Since it included a  $90^\circ$  phase shift in one branch, the RF input signal was suppressed at the output. In each interferometer

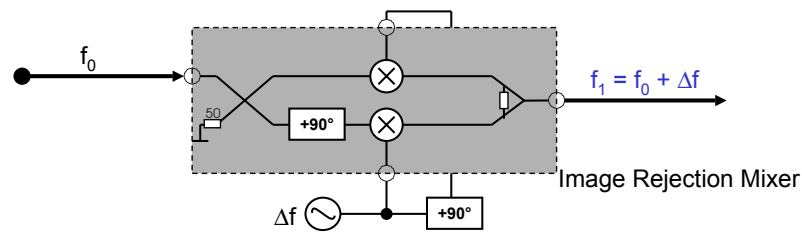


Figure 3.28: Schematic of the electrical circuit used for shifting the clock frequency. The grey box was a commercially available image rejection mixer.

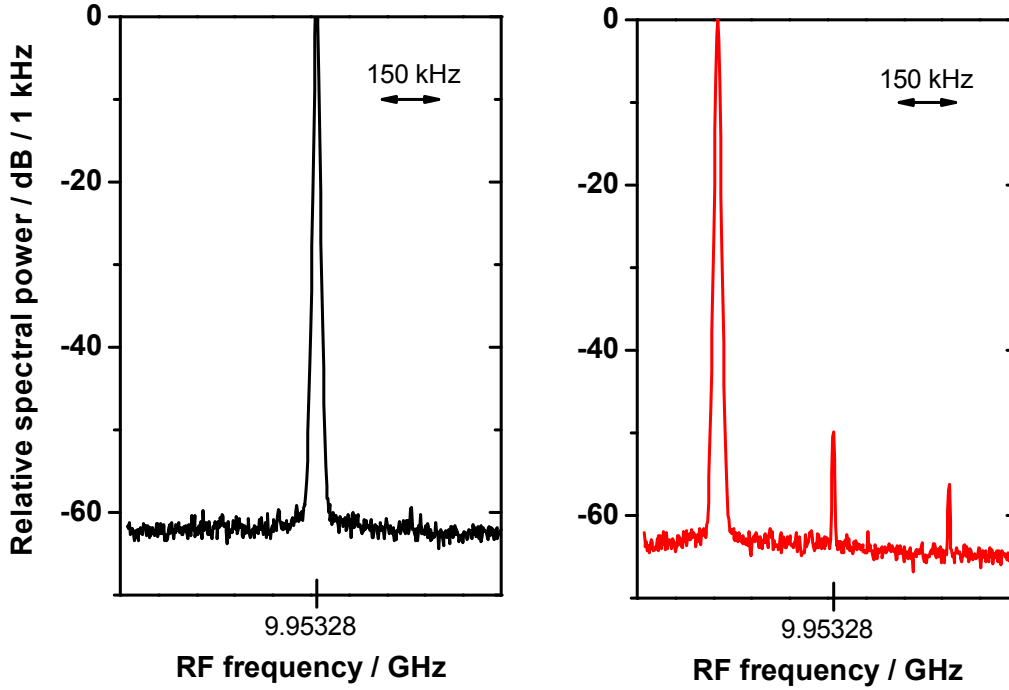


Figure 3.29: *Electrical spectra of the RF clock signal before (left) and after (right) the image rejection mixer. The frequency shift was  $\Delta f = 303$  kHz.*

branch, the RF signal was modulated by a double balanced mixer with the modulation frequency  $\Delta f$ . If the modulation frequency was fed to the two mixers with a  $90^\circ$  phase shift as indicated, one modulation sideband was also suppressed by the interferometer, leaving only the other sideband present at the output of the device.

The amount of suppression of the unwanted sideband is determined by the amplitude and phase accuracy of the modulation frequency. The suppression of the carrier itself depends on the phase difference between the two interferometer arms. By applying an individual DC bias to each double balanced mixer, the suppression of the device could be greatly enhanced to about 50 dB as shown in Fig. 3.29. The left figure shows the electrical spectrum of the extracted clock signal with a frequency of  $f_{\text{clock}} = 9.95328$  GHz. The right figure shows the electrical spectrum at the output of the image rejection mixer. The modulation frequency was  $\Delta f = 303$  kHz in this case. Note that the vertical scale has been normalized in each spectrum. The generated sideband had about 15 dB less peak power than the input signal, but was amplified back to the required level using an octave-band RF amplifier. It can be seen that the carrier was suppressed by about 50 dB with respect to the left sideband. The right sideband was suppressed by 55 dB. Higher harmonics of the modulation frequency were also visible outside the spectral range depicted in Fig. 3.29. They were however more than 55 dB below the used left sideband and thus were negligible.

It should be noted that this technique does in principle not alter the jitter of the clock signal. However, it might add jitter through the modulation frequency.

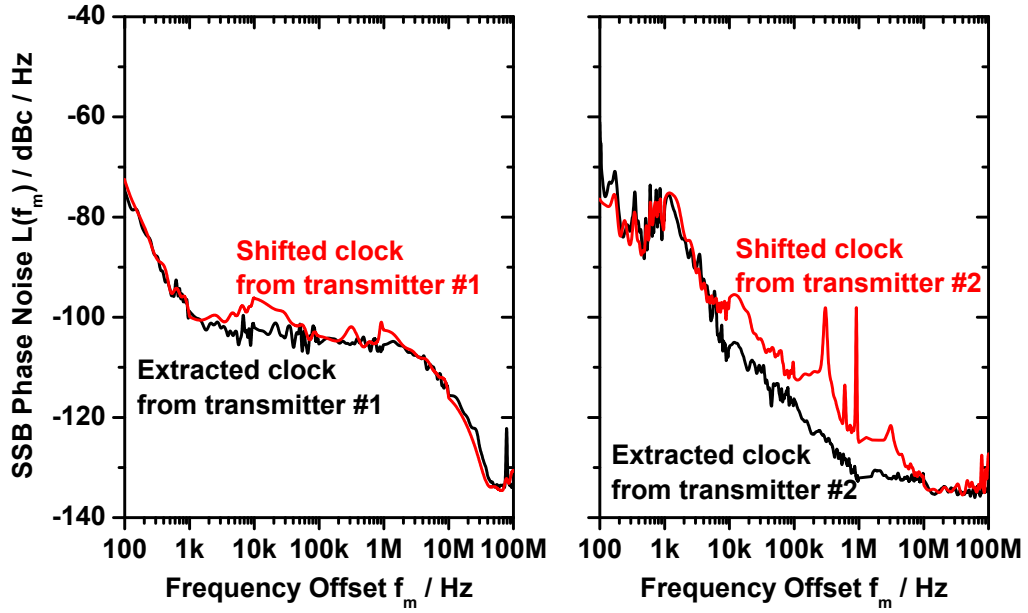


Figure 3.30: SSB noise curves of the extracted electrical clock signal before and after the frequency shifter for two different optical transmitters. The frequency shift was  $\Delta f = 303$  kHz in this case.

To estimate the influence of the frequency shifter on the jitter of the clock signal, the SSB phase noise was measured before and after the frequency shifter (Fig. 3.30). The measurement was repeated for two different optical transmitters which exhibited different phase noise. Thus the extracted electrical clock signals for the two transmitters showed different phase noise curves. In comparison to transmitter #2, the phase noise of transmitter #1 was lower between 100 Hz and 10 kHz and higher for offset frequencies larger than 10 kHz. Altogether, transmitter #2 showed a lower jitter value than transmitter #1. Looking at the shifted clock from transmitter #2, peaks were found around 300 kHz and higher harmonics of it, which were due to the the shift frequency (300 kHz) and higher harmonics of it. Also the frequency shifter added about 5-10 dBc/Hz of phase noise to the clock signal at offset frequencies above 10 kHz. This additional phase noise was not detectable in the measurement with transmitter #1 due to its larger initial phase noise. The residual peaks from the shift frequency were also only hardly detectable. On the other hand, there was increased phase noise between 5 kHz and 50 kHz for this signal, which was also found in the curve for transmitter #1.

Integrating the measured data, a slight increase in phase noise due to the frequency shifter was observed for the low jitter clock signal (transmitter #2) from 130 fs to 160 fs. For the medium jitter clock signal (transmitter #1) the jitter was increased from 270 fs to 300 fs, indicating that the main increase arose from the region between 5 kHz and 50 kHz.

In conclusion, the shifted clock signal showed no significant jitter increase and thus this frequency shifting technique was applied in the optical sampling system.

### 3.4.2 Frequency Dividers

The clock processing unit as depicted in Fig. 3.26 was based on a number of frequency dividers. These dividers were realized by concatenation of a number of commercially available low phase noise GaAs HBT MMIC dividers (Hittite Microwave Corporation, HBT: hetero bipolar transistor, MMIC: monolithic microwave integrated circuit).

The "1/N" division was achieved by a cascade of 4 dividers to achieve the desired division ratio of  $32^3$ . The output of each divider was a square signal with a duty cycle that was dependent on the division ratio. However, as the offset frequency  $\Delta f$  for the frequency shifter unit had to be a sinusoidal signal, a phase locked loop (PLL) circuit was used to filter the output signal of the divider cascade. To relax the requirement on the PLL filter, the last divider in the "1/N" chain was operated in a "divide-by-2" mode, which produced an output signal with a 50 % duty cycle.

The "1/2M" divider cascade was used to generate the signals for the sampling pulse repetition rate reduction, which was described in Sec. 3.2. It was composed of 2 individual dividers, which generated output signals with 50 % duty cycle each. The output of the "1/2M" chain was finally amplified using a wide band (100 kHz-18 GHz) amplifier and split into two signals. The relative phase between the two signals was adjusted using an electrical delay line such that the rising flanks had a relative delay of about 70 ps. These signals were used to generate the modulator window as described in Sec. 3.2.

The "1/M" divider cascade was also composed of 2 individual dividers. It generated the clock signal for the A/D converter inside the digital oscilloscope of the O/E detection unit. A voltage controlled phase shifter (not shown in Fig. 3.26) was used to align the phase of the A/D clock signal with the arrival time of the optical samples.

### 3.4.3 Random Optical Sampling

The clock processing unit described in the previous sections was needed in order to get the information on the time event of the individual optical sampling process. This was achieved by synchronizing the sampling pulse source to the data signal and applying a defined frequency offset such that the timing of each optical sample was known by Eqs. (2.1)ff. A second approach is to omit the clock processing unit and to measure the time events of the individual optical samples directly using the A/D converter in the O/E detection unit [14].

Fig. 3.31 shows the block diagram of such a system with random optical sampling. In comparison to the conventional optical sampling system (see Fig. 3.1) this block diagram does not contain a clock processing unit. Instead the sampling pulses as well as the recovered clock signal are directly fed into the O/E detection unit. The sampling pulse source is thus not synchronized to the optical data signal and the information about the sampling times of the individual optical samples cannot be derived from the offset frequency between the data signal and the sampling pulse source. However, by detecting the recovered clock signal together with the sampling pulses directly in the O/E detection unit, it is possible to measure the sampling time of each optical sample with respect to the reference clock. This procedure is described in detail in [14] and was adopted in the present work for the experiments described

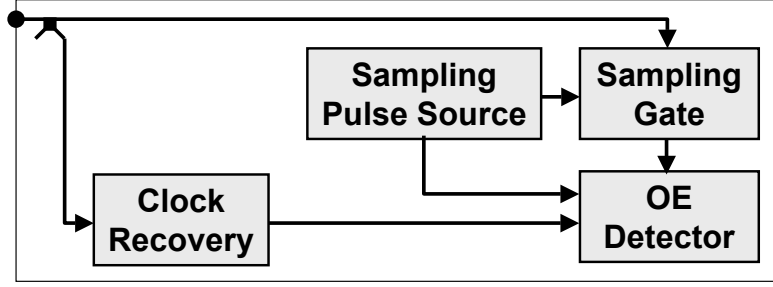


Figure 3.31: Block diagram of the random sampling system.

in Sec. 5.2.3. Since the sampling process is performed at randomly varying sampling times, this type of sampling system will be called "random sampling system". It requires an additional A/D converter channel and a special sampling software which calculates the sampling times from the arrival time of each optical sampling pulse.

### 3.5 Sample Detection

The final unit of the optical sampling system was the sample detection. The function of the sample detection block was to measure the energy of each individual optical sample and to display it versus the temporal sampling position. The set-up of the sample detection is depicted in Fig. 3.32.

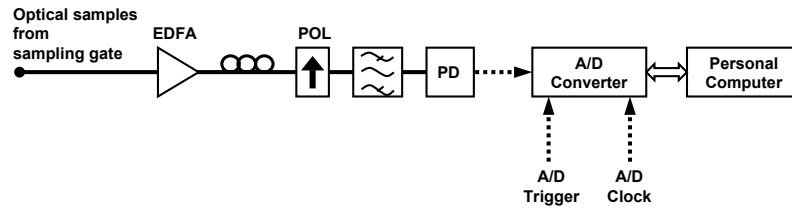


Figure 3.32: Schematic set-up of the sample detection.

The optical samples were pre-amplified using an Erbium doped fiber amplifier (EDFA). Using a polarization controller and a polarizer (POL), about half of the unpolarized amplified spontaneous emission of the EDFA was suppressed. A narrow bandpass filter (1.7 nm FWHM) was used to further suppress the ASE outside the filter bandwidth. At the same time, the filter slightly broadened the optical sample in the time domain. Then the sample was detected using a photodetector (PD). The electrical bandwidth of the detector was about 1 GHz. Thus the resulting electrical sample was significantly broadened in time. However, since the sampling rate was only 311 MHz, there was no temporal overlap of the individual broadened electrical samples. Finally, an analog/digital (A/D) converter was used to measure the peak voltages of the individual samples. The peak voltages were a measure for the energy of

the optical samples since the temporal shape of the electrical samples was independent of their energies.

The A/D converter was a digital oscilloscope with external clock input (LeCroy WavePro 960). The clock signal for the A/D converter in the digital oscilloscope was generated in the clock processing unit (Sec. 3.4) and was a 311 MHz square wave signal which was synchronous to the optical samples. This ensured that for each sample a single A/D conversion was performed. A variable electrical delay line (not shown in Fig. 3.32) was used to adjust the phase of the A/D clock signal such that the A/D conversion was done at the peak of the electrical sample. The trigger signal for the oscilloscope was provided by the clock processing unit as well and was synchronous to the offset frequency by which the extracted 10 GHz clock frequency was shifted. This enabled a real-time display of the optical eye diagram on the screen of the oscilloscope.

The acquired data from the oscilloscope was finally transferred to a personal computer for storage and evaluation.

## Chapter 4

# Characterization of the Optical Sampling System

This chapter deals with the experimental characterization of the optical sampling system which was realized in this work. The chapter is sub-divided into two sections. The first section focusses on the optical sampling system based on the GT-UNI sampling gate. The second section deals with the NOLM based system. The sections will focus on the most important parameters of an optical sampling system, which depend on the optical gate. These parameters are the temporal resolution, the wavelength range and the linearity.

### 4.1 GT-UNI Based System

#### 4.1.1 Temporal Resolution

The temporal resolution of the GT-UNI sampling gate is mainly determined by the differential group delay (DGD) of the polarization maintaining fiber (PMF) in the set-up. The DGD in turn depends on the length and birefringence of the PMF. The longer the PMF, the higher is the DGD. The PMF used in this work was of the type F-SPPC-15 by Newport. It was cut to the desired length and spliced to standard single-mode fiber. The DGD of the prepared PMF piece was then measured with the polarization mode dispersion (PMD) analyzer HP8509 by Agilent Technologies. Since the GT-UNI was assembled as hybrid fiber set-up, it was easily possible to exchange the piece of PMF and thus to change the temporal resolution of the sampling gate. In the experiments, three different PMF lengths were used as listed in Table 4.1.

To characterize the temporal resolution of the sampling gate, the gating window was measured using a static pump-probe configuration (Fig. 4.1). Two tunable mode-locked lasers (TMLL) operating at 10 GHz were used as pulse sources for pump and probe. The pump laser was the device that has been described in Sec. 3.2 and had a wavelength of 1310 nm. The probe laser was similar, except that it was operating near 1550 nm. The probe laser was driven by a 10 GHz electrical signal generator. The pump laser was synchronized to the probe laser by the electrical clock extraction (CE) described in Sec. 3.3.1. An optical delay line (OD) was used to delay the probe pulses with respect to the control pulses. The output signal of the sampling gate was

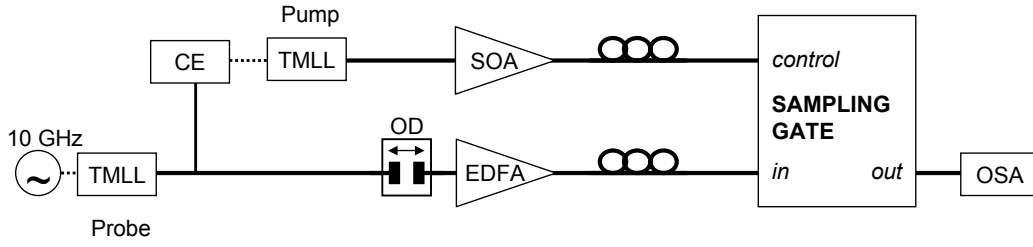


Figure 4.1: *Experimental set-up for the static measurement of the gating window*

detected with an optical spectrum analyzer (OSA). The resolution bandwidth of the OSA was chosen larger than the spectral bandwidth of the probe signal.

Measuring the gated output power versus the optical delay between the control and probe pulses yielded the convolution of the gating window with the probe pulses. By using short probe pulses this technique provides a high temporal resolution as well as a high sensitivity due to the time averaging of the OSA.

Fig. 4.2 shows the measured output power when PMF2 was used in the GT-UNI. The left side depicts the results on a logarithmic scale and the right side on a linear scale. For this experiment the wavelength of the probe laser was set to 1546.5 nm. The measurement with the optical spectrum analyzer yielded the output power in the logarithmic scale. Please note that the transmittance has been normalized in Fig. 4.2.

From the logarithmic plot, a contrast of the gating window of about 20 dB was found. Two additional secondary peaks were identified in the gating window. These resulted from trailing pulses of the pulse sources used in the experiment. They can however be neglected as the sampling system will plot the eye diagrams in a linear scale as shown on the right hand side of Fig. 4.2. The width (FWHM) of the measured trace was  $\tau_{meas} = 2.6$  ps. Taking into account the finite width of the probe pulses of  $\tau_{probe} = 1.5$  ps and assuming a Gaussian shape of the gating window, the gating window width can be calculated using the following relation:

$$\begin{aligned}
 \tau_{GW,GT-UNI} &= \sqrt{\tau_{meas}^2 - \tau_{probe}^2} \\
 &= \sqrt{2.6^2 - 1.5^2} \text{ ps} \\
 &= 2.1 \text{ ps}
 \end{aligned} \tag{4.1}$$

Table 4.1: *Parameters of PMF's used in the GT-UNI sampling gate.*

Fiber	Length (m)	DGD (ps)
PMF1	3.8	6.5
PMF2	1.8	3.1
PMF3	1.2	2.0



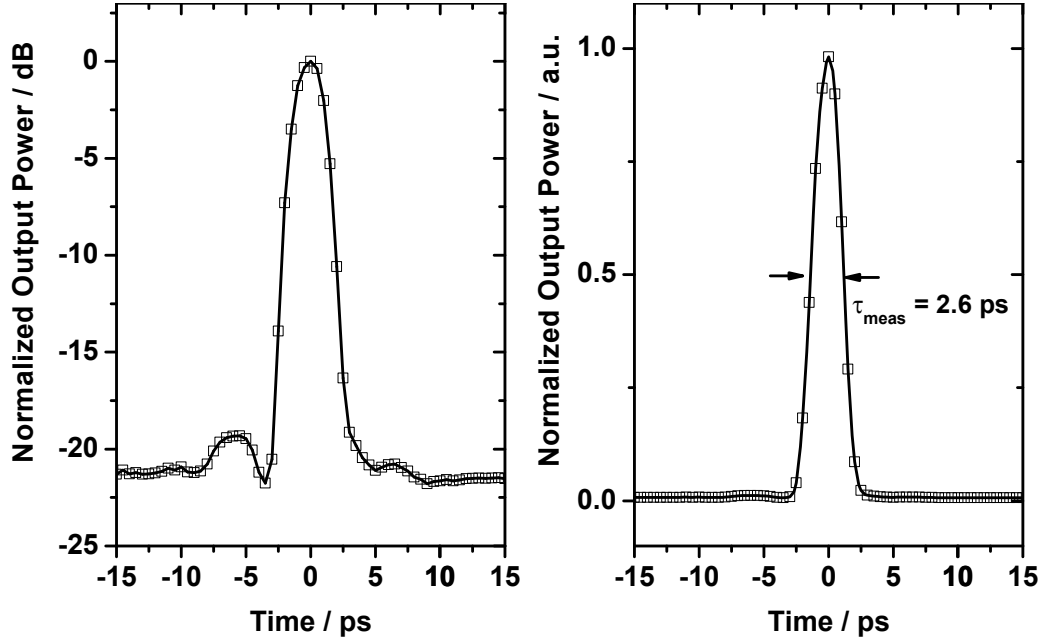


Figure 4.2: Measured output power for GT-UNI with PMF2. The left plot shows the normalized trace on a logarithmic scale. The right plot shows the same data on a linear scale. The wavelength of the probe signal was  $\lambda_{Probe} = 1546.5$  nm.

The deconvolution thus yields a gating window width of 2.1 ps for the GT-UNI with the PMF2. This corresponds to an optical bandwidth of 210 GHz.

Next, the optical bandwidth of the GT-UNI was investigated for all three PMF samples. For these measurements, the complete sampling system was used to measure the eye diagrams of a 160 Gbit/s data signal. These measurements are described in detail in Sec. 5.2.2. The gating window width was calculated from the measured width of the eye diagrams using Eq. (4.1).

Fig. 4.3 shows the results for the three PMF samples listed in Table 4.1. The solid line shows a simulation using the model described in Sec. 3.1.1. Here, a sampling pulse width of  $\tau_{SP} = 1.3$  ps and a maximum phase shift of  $\Delta\Phi = 0.5\pi$  was assumed.

The measured gating window widths agree well with the values expected from the simulation using the simple model of the phase dynamics of the SOA presented in Sec. 3.1.1. Please note that the gating window width is slightly smaller than the DGD of the PMF for all three PMF samples. This is due to the finite width of the sampling pulse as well as the limited phase shift that is induced as was discussed in Sec. 3.1.1.

Following Eq. (3.7), the GT-UNI gate with PMF1 had an optical bandwidth of  $B = 73$  GHz, while in the configuration with PMF3 an optical bandwidth of  $B = 257$  GHz was reached. Such a high bandwidth was obtained even in an SOA based sampling gate because the differential gating scheme was applied.

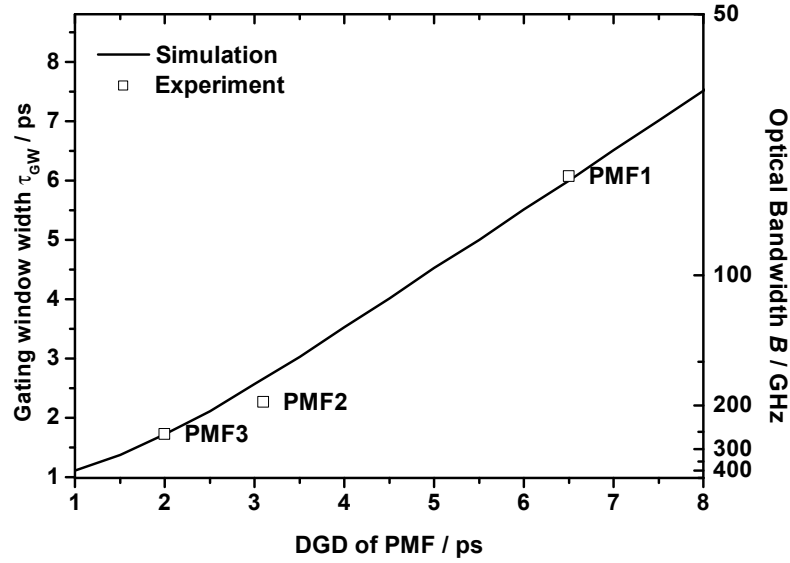


Figure 4.3: Measured gating window width of the GT-UNI gate for the three PMF fibers used. The solid line shows a simulation using the model described in Sec. 3.1.1 for a sampling pulse width of  $\tau_{SP} = 1.3$  ps and a maximum phase shift of  $\Delta\Phi = 0.5\pi$ . The optical bandwidth is related to the gating window width by Eq. (3.7).

### 4.1.2 Linearity

A high linearity is mandatory for any sampling gate. The term "linearity" should however not be mistaken for a description of the exploited physical process in the sampling gate. All sampling gates used in this work are based on nonlinear optical processes. "Linearity" in the way it is meant here, describes the relation between the gated signal power and the input signal power of the sampling gate. In this respect, a "linear" gate is mandatory for an optical sampling system since a nonlinearity would consequently lead to an amplitude distortion in the reproduction of the waveform under test.

The linearity was measured using the set-up depicted in Fig. 4.1. The optical delay was adjusted to the maximum of the gating window. Using an additional variable attenuator in the probe branch (not shown), the probe input power was varied. The energy of the sampling pulses was 20 pJ at the control input of the GT-UNI. Fig. 4.4 shows the measured maximum output power as a function of the signal input power. A strictly linear dependence over a range of 50 dB was observed [36]. This result was due to the gain-transparent operation of the SOA in the sampling gate [82]. In conventional SOA based gates, the maximum output power saturates with increasing signal input power because the signal itself saturates the gain of the SOA. Gain-transparent SOA based gates however show a strictly linear performance because the signal wavelength is outside the gain region of the SOA.

However, Fig. 4.4 indicates an insertion loss of the GT-UNI of about 30 dB. This fairly high value results mainly from losses in the 1300 nm SOA (about 17 dB) and

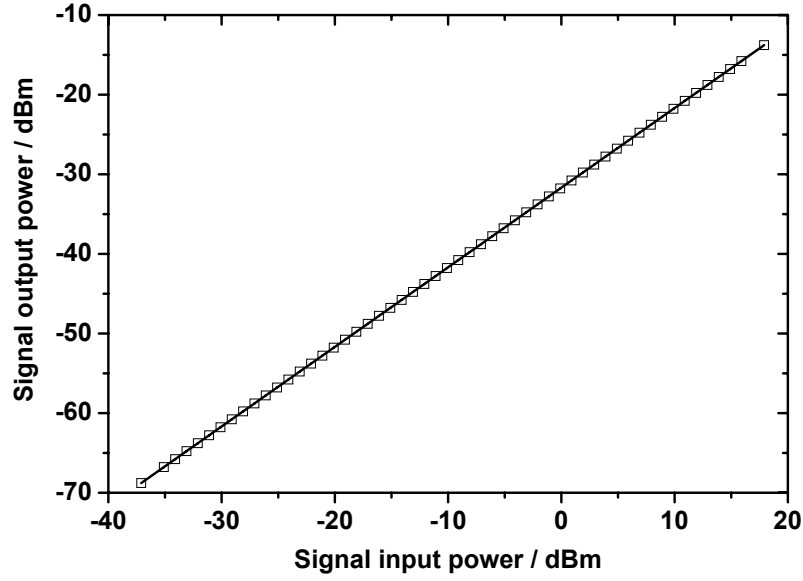


Figure 4.4: *Output power versus input power for GT-UNI*

from losses in the hybrid setup. These losses must be compensated in the sampling system by amplifying the signal under investigation before it enters the sampling gate.

### 4.1.3 Wavelength Range

It has been shown that a gain-transparent optical gate can be operated over a wide wavelength range of 160 nm from 1430-1590 nm [83]. This makes this type of gate especially suited for optical sampling of data signals in the communication windows of the fiber, namely the S-, C- and L-band. Fig. 4.5 shows schematically the wavelength allocation of the sampling pulses with respect to the acceptable wavelength range for the data signal. The sampling pulses at 1310 nm were separated from the data signal in the sampling gate using a WDM coupler, which acts as edge filter (see Fig. 3.6). The wavelength acceptance range (shaded region in Fig. 4.5) thus covered in principle the S-, C-, and L-band without changing the set-up of the GT-UNI or exchanging the

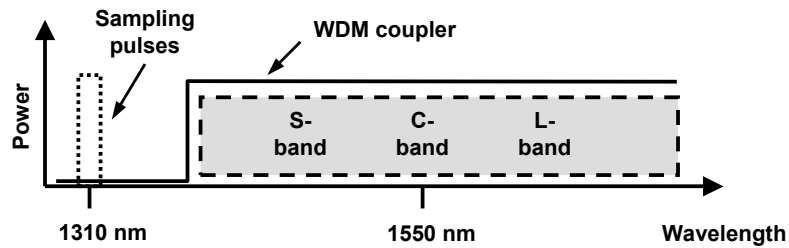


Figure 4.5: *Wavelength allocation for the GT-UNI sampling gate.*

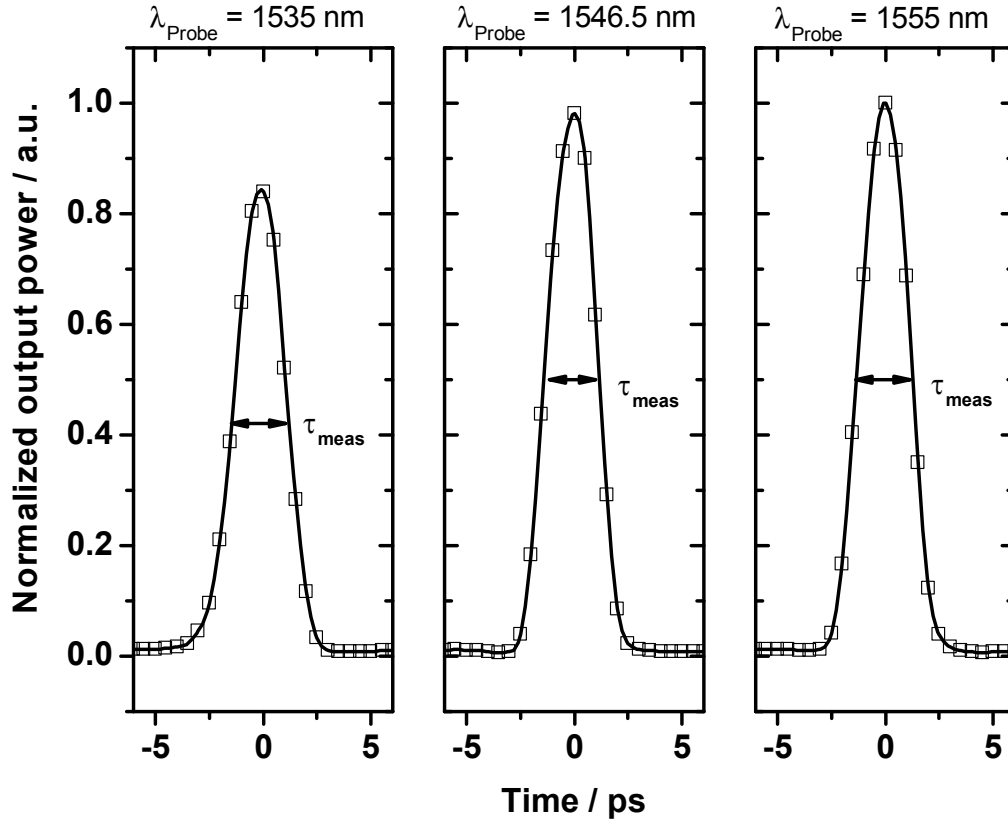


Figure 4.6: Measured gating windows at different signal wavelengths for the GT-UNI sampling gate.

components.

Unfortunately, there were no pulse sources and amplifiers available outside the C-band at the time of the measurements in this work. Thus it was only possible to characterize the gating window within the C-band [36]. Fig. 4.6 shows as an example the gated output power  $P_{out}(t)$  for three different probe signal wavelengths in the C-band. The measurements were performed as described in Sec. 4.1.1. The energy of the pump and probe pulses was kept constant at 0.5 pJ and 20 pJ, respectively (measured at the input ports of the GT-UNI). The corresponding pulse widths were 1.5 ps and 0.8 ps, respectively. The probe signal input power was kept constant for all three measurements. The measured gated power was normalized to the maximum gated power of the measurement at 1555 nm. It can be seen from Fig. 4.6 that the maximum gated power decreased slightly for lower wavelengths. This is attributed to a slight misalignment of the sampling gate and is no general result.

It can be seen, that the shape of the gating windows was not dependent on the probe signal wavelength. A width (FWHM) of  $\tau_{GW} = 2.1$  ps (after deconvolution with the probe pulse width) and a contrast of 20 dB was obtained for all three wavelengths shown.

Fig. 4.6 shows the gating window over a wavelength range of 18 nm. This is

only a fraction of the wavelength acceptance range of the GT-UNI sampling gate. The choice of the lowest wavelength was limited in the experiment by the gain of the EDFA which was used to amplify the probe pulses in the set-up. The highest wavelength was limited in the experiment by the tuning range of the TMLL which was used as probe pulse source.

## 4.2 NOLM Based System

### 4.2.1 Temporal Resolution

In contrast to the GT-UNI sampling gate, the temporal resolution of the NOLM sampling gate is mainly determined by the width of the sampling pulses, since the NOLM gate relies on the fast Kerr nonlinearity of the optical fiber (see Sec. 3.1.2). In order to measure the temporal resolution of the NOLM gate, a different approach was taken as compared to Sec. 4.1.1, where the gating window was measured using a static pump-probe set-up. In this section, the complete sampling system was used to measure the waveform of a probe pulse of which the pulse width was known. Then the gating window width can be deduced from the displayed pulse width.

The probe pulses had a repetition rate of 10 GHz which allowed to average the measured data from the sampling system in order to eliminate noise and jitter. Fig. 4.7 shows the measured waveform of the probe pulse measured by the sampling system. The displayed pulse had a measured pulse width of  $\tau_{meas} = 1.8$  ps. Taking into

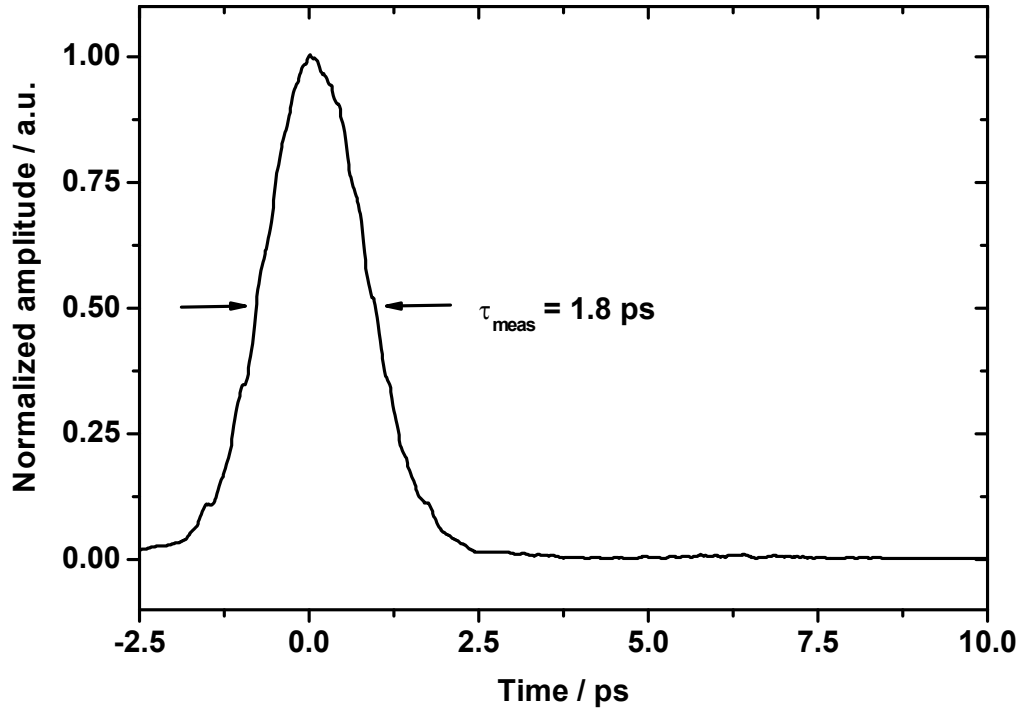


Figure 4.7: Measured gating window for the NOLM sampling gate.

account the actual pulse width of the input pulses of  $\tau_{probe} = 1.0$  ps as measured by an autocorrelator, the temporal resolution of the sampling system becomes

$$\begin{aligned}\tau_{GW,NOLM} &= \sqrt{\tau_{meas}^2 - \tau_{probe}^2} \\ &= \sqrt{1.8^2 - 1.0^2} \text{ ps} \\ &= 1.5 \text{ ps}\end{aligned}\tag{4.2}$$

Using Eq. (3.7), this corresponds to an optical bandwidth of about 295 GHz.

This experiment was performed at a signal wavelength of 1542 nm. It will be shown in a later section that the actual temporal resolution of the NOLM sampling gate was slightly dependent on the data wavelength.

### 4.2.2 Linearity

In contrast to the GT-UNI sampling gate, the NOLM sampling gate uses a passive element (HNLF) as nonlinear medium inside the fiber loop. Thus a high signal power cannot saturate the nonlinear medium and cause a nonlinear gating characteristic of the NOLM gate. On the other hand, a signal which is input into the NOLM gate with high power will experience self-phase modulation upon passage through the fiber loop. However, the phase shifts of the clockwise and anti-clockwise travelling signal component will cancel each other when the two signal components interfere at the coupler C1 (see Fig. 3.10). This holds true as long as the coupler C1 has a coupling ratio of 50 % and as long as there is no dispersion inside the loop. In this case the gate is "balanced" even for high signal input powers and shows a strictly linear characteristic [84].

In practice, the coupling ratio of the coupler C1 is not perfectly 50 %. Also the losses inside the fiber loop are asymmetric due to the second coupler C2, which will limit the linear regime of the NOLM gate. Even more severe is the combined effect of self-phase modulation of the signal components and the residual dispersion of the fiber loop, which will distort the shape of the signal components for high signal input powers. This effect is the dominant limitation of the maximum signal input power.

For the NOLM gate used in this work, experiments showed that the signal became distorted starting at an average signal power of +10 dBm for a 10 Gbit/s data signal. Compared to the measurements for the GT-UNI gate (Fig. 4.4) this value is almost 15 dB lower than the maximum applied input power in that case. On the other hand, the NOLM gate exhibited a total insertion loss of only about 10 dB, which was 20 dB lower than the insertion loss of the GT-UNI gate. Therefore, the usable dynamic range of the NOLM gate was extended by 20 dB to lower input signal powers as compared to the GT-UNI gate.

### 4.2.3 Wavelength Range

The wavelength allocation for the NOLM gate is different from the wavelength allocation in the GT-UNI gate. As depicted in Fig. 4.8, the sampling pulses had a

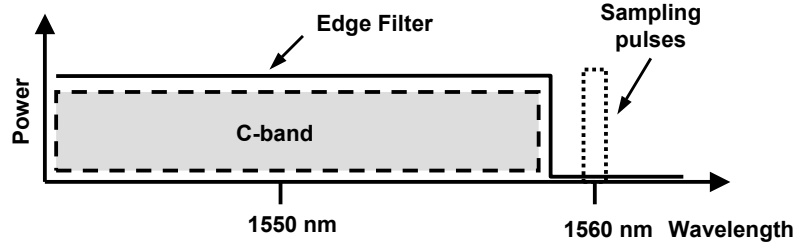


Figure 4.8: Wavelength allocation for the NOLM sampling gate.

wavelength, which was longer than the wavelength of the data signal under investigation.

In the experiments, a sampling pulse wavelength of 1560 nm was chosen because the sampling pulse source #2 could not be tuned to higher wavelengths. In general, a longer sampling pulse wavelength would have been desirable in order to increase the wavelength range of the sampling system. As shown in Fig. 4.8, the sampling pulses can be separated from the data signal at the output of the NOLM gate using an edge filter. However, in the experiments presented here, a tunable bandpass filter was used to filter out the data wavelength because an edge filter was not available at the time of the experiments.

The wavelength range of the NOLM sampling gate is mainly determined by the temporal walk-off between the signal and the sampling pulses in the HNLF. In order to evaluate the wavelength range of the NOLM gate, the NOLM based sampling system

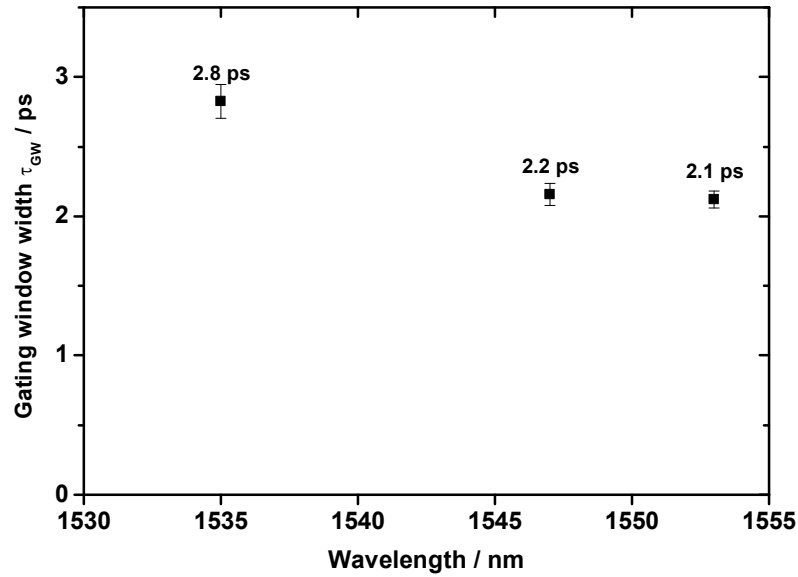


Figure 4.9: Average gating window  $\tau_{GW}$  for different signal wavelengths. The error bars indicate the standard deviation of all measured values for a specific wavelength.

was used to measure eye diagrams of 160 Gbit/s data signals at different wavelengths. These measurements are described in more detail in Sec. 5.2.1. To derive the gating window width from the measured eye diagrams, the eye diagrams were evaluated using the procedure described in Sec. 2.4. Then the gating window width was calculated from the measured eye diagram width using Eq. (4.2). The data pulse width used for the deconvolution was measured independently using an autocorrelator. Fig. 4.9 shows the results for probe wavelengths of 1535 nm, 1547 nm and 1553 nm.

Since each eye diagram measurement covered a number of individual eye diagrams, the plot shows the mean value for each probe wavelength. The error bars depict the standard deviation of the values for each wavelength. It can be seen that the gating window width increased with decreasing data wavelength. This can be attributed to the increasing walk-off between the data signal and the sampling pulses at 1560 nm. The gating window width ranges from 2.1 ps (209 GHz bandwidth) at 1553 nm to 2.8 ps (157 GHz bandwidth) at 1535 nm. These values are somewhat higher than the value shown in Sec. 4.2.1. The reason is that for the experiment discussed here, sampling pulses with the larger pulse width of  $\tau_{SP} = 1.7$  ps were used.



## Chapter 5

# Applications of the Optical Sampling System

This chapter deals with the application of the optical sampling system. The chapter is divided into three sections, each section dealing with experiments that were performed in a particular mode of operation of the sampling system. The first section describes waveform measurements where the optical sampling system was operated in an averaging mode. The second section describes eye diagram measurements using different set-up's of the optical sampling system. The third section finally describes 160 Gbit/s transmission experiments in which the optical sampling system was used to analyze signal distortions. The 160 Gbit/s (320 Gbit/s) transmitter that was used in all experiments, is described in detail in Appendix A.1.

### 5.1 Waveform Measurements

#### 5.1.1 NOLM Based System

This section describes the monitoring of RZ bit patterns at a data rate of 160 Gbit/s and 320 Gbit/s [13]. For these experiments, the NOLM based optical sampling system was used.

The experimental set-up is shown in Fig. 5.1. For this experiment, a pulse compressor was inserted into the data transmitter after the modulator. (The compressor is not shown in Fig. A.1). The pulse compressor was set up in a similar way as described in Sec. 3.2.2 by exploiting supercontinuum generation in a highly nonlinear fiber and subsequent bandpass filtering. The wavelength of the data signal was 1542 nm and

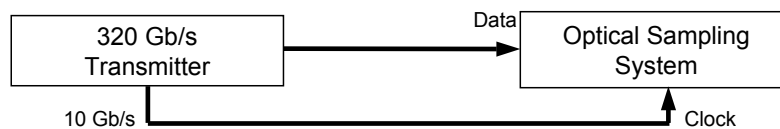


Figure 5.1: Schematic set-up of bit pattern monitoring experiment.

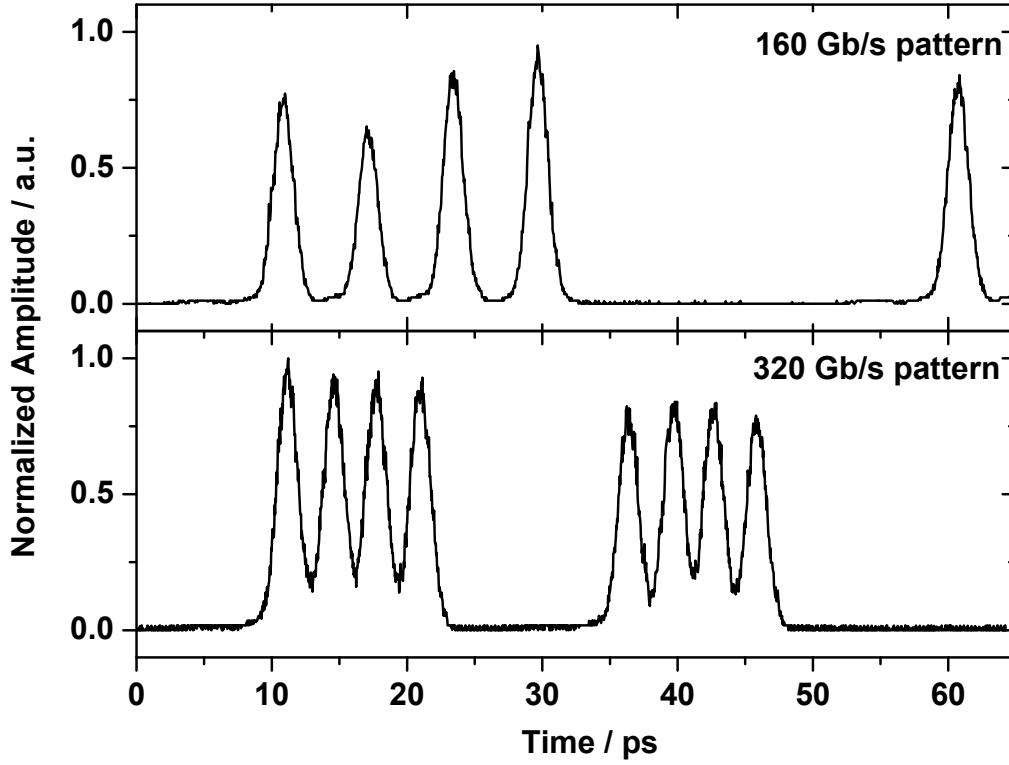


Figure 5.2: 160 Gbit/s and 320 Gbit/s bit patterns recorded with the NOLM based optical sampling system.

the pulses had a width of 1 ps as measured by an autocorrelator. The transmitter was set to "U10110" to generate a 160 Gbit/s pattern consisting of four logical "1" bits, followed by four logical "0" bits. This pattern was repeating every 50 ps, so that it was possible to average the measured data from the sampling system in order to eliminate noise and jitter. In order to generate the 320 Gbit/s bit pattern, the transmitter was set to "U11011" which produced the same logical pattern as before, however this time at a bit rate of 320 Gbit/s. The sampling pulses had a wavelength of 1551 nm and a pulse width (FWHM) of  $\tau_{SP} = 1.0$  ps.

As this set-up did not include any fiber transmission, the clock signal was directly taken from the transmitter for convenience. Inside the optical sampling system, the clock extraction scheme was applied as described in Sec. 3.3.1 to synchronize the optical sampling system to the transmitter.

Fig. 5.2 shows the experimental results. It can be seen that due to the short sampling pulse width and the small walk-off in the NOLM, the optical sampling system was capable of resolving the individual bits of the data pattern up to a bit rate of 320 Gbit/s. The pulse width (FWHM) of the displayed pulses was 1.5 ps for both traces.

Both data patterns were generated using the same transmitter with a pulse width of  $\tau_{probe} = 1.0$  ps. The 160 Gbit/s trace shows a clear gap between the individual bits since the spacing of the data bits is 6.25 ps. No ringing between the sequences

of marks occurs in both traces. This is due to the optical sampling process which – in contrast to electrical sampling systems – involves no electrical high frequency components that might suffer from electrical reflections.

The optical sampling system allows also to detect a small amplitude modulation which was present in the 160 Gbit/s pattern and which was due to a minor misalignment in the multiplexer that generated the pattern.

## 5.2 Eye Diagram Measurements

### 5.2.1 NOLM Based System

The set-up for this experiment was the same as depicted in Fig. 5.1. As this set-up did not include any fiber transmission, the clock signal was again directly taken from the transmitter for convenience. Inside the optical sampling system, the clock extraction scheme was applied as described in Sec.3.3.1 to synchronize the optical sampling system to the transmitter.

Fig. 5.3 shows measured eye diagrams at a data wavelength of 1535 nm that were recorded with a persistence of about 100 traces. The left figure shows a time span of more than 100 ps, which allows to see all 16 OTDM channels at a time. It can be seen that due to a slight misalignment in the multiplexer of the transmitter, the individual eye diagrams have slightly different peak powers. Since the transmitter was operated on a base data rate of 10 Gbit/s, this pattern repeats after 16 channels. An enlarged detail of the eye diagram is shown on the right hand side of Fig. 5.3. It can be seen that the eyes of all channels are clearly open and that no ringing occurs.

In order to demonstrate the broad wavelength range of the NOLM based sampling

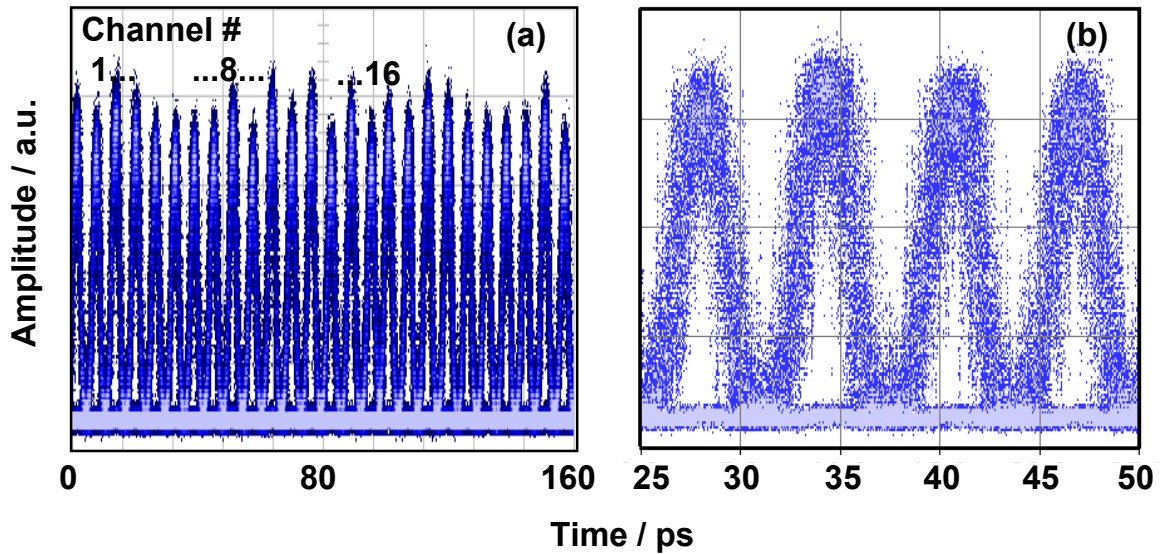


Figure 5.3: 160 Gbit/s eye diagrams at 1535 nm measured using the NOLM based sampling system showing all 16 OTDM channels (a) and as enlarged detail (b).

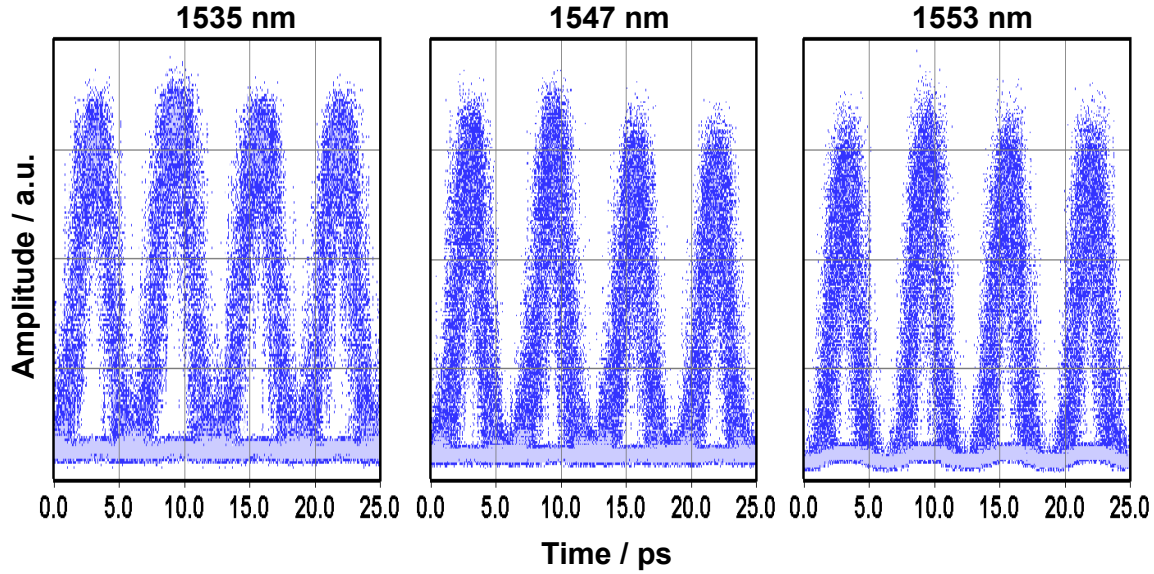


Figure 5.4: 160 Gbit/s eye diagrams for different wavelengths measured using the NOLM based sampling system.

system, the transmitter was now set to "M00110". In this mode, it generated a pseudo 160 Gbit/s OTDM signal which consisted of four adjacent 10 Gbit/s OTDM channels. Then the wavelength of the pulse source inside the transmitter was tuned and eye diagrams were recorded for different wavelengths of the data signal. Instead of tuning the pulse source directly, supercontinuum generation in a highly nonlinear fiber was used with a second set-up similar to the one depicted in Fig. 3.15. By that, the wavelength of the data signal could easily be varied by tuning the optical bandpass filter after the HNLF.

Fig. 5.4 shows the measured eye diagrams for three different wavelengths (1535 nm, 1547 nm and 1553 nm) in the C-band [13]. The wavelength of the sampling pulse source was kept at 1560 nm for all measurements. These particular data wavelengths were chosen to investigate the performance of the NOLM based sampling system at the limits of the experimentally accessible wavelength range. The wavelength range was limited at the short wavelength side at 1535 nm due to the limitation in the gain bandwidth of the available EDFA. The limit of 1553 nm at the long wavelength side was due to the given wavelength of the sampling pulses of 1560 nm. Since bandpass filtering was needed to separate the sampled signal from the sampling pulses at the output of the NOLM and since the short sampling and data pulses had a relatively broad optical spectrum, it was not possible to place both signals closer than 7 nm. The third wavelength of 1547 nm was chosen because this wavelength was the zero dispersion wavelength of the HNLF used in the NOLM sampling gate. Thus it could be expected that the walk-off between the data signal and the sampling pulses was maximum in that case resulting in the maximum gating window width, i.e. lowest timing resolution.

From Fig. 5.4 it can clearly be seen that open eye diagrams were measured over the

whole wavelength range under investigation. For the evaluation of the measured eye diagrams, first the widths (FWHM) of the eye diagrams at the different wavelengths were compared. The result was already shown in Sec. 4.2.3, Fig. 4.9. It is interesting to note that the maximum FWHM did not occur at the data wavelength of 1547 nm but at the data wavelength of 1535 nm. However, looking at the shape of the measured eyes reveals that the eyes at 1547 nm exhibited a slightly different shape than those at the other wavelengths. They appeared compressed in the high amplitude region and showed broad tails (pedestals) in the low amplitude region. This is attributed to a nonlinear change of the pulse shape of the data signal while travelling through the HNLF. This effect is most prominent when the data signal is at the zero dispersion wavelength of the HNLF. Therefore, the width of this eye diagram is not directly comparable to the other eye diagrams.

Secondly, the measured eye diagrams were evaluated with respect to the RMS timing jitter. Since each measured eye diagram covers four separate eyes, the timing jitter was calculated from the horizontal histograms for each of the eight flanks. Then the mean value and its standard deviation was computed. RMS timing jitter values of  $523 \pm 51$  fs,  $502 \pm 24$  fs and  $503 \pm 31$  fs were obtained for the eye diagrams at 1535 nm, 1547 nm and 1553 nm, respectively. This shows that within the accuracy of the measurement (5-10 %), the timing jitter was the same for all wavelengths under investigation.

### 5.2.2 GT-UNI Based System

For these experiments, the set-up shown in Fig. 5.1 was used again. The transmitter was set to "M00110" to generate a quasi 160 Gbit/s data signal. In contrast to the previous section, the supercontinuum generation stage was removed from the transmitter and the TMLL was used directly. The output wavelength of the TMLL was varied by tilting the surface grating inside the laser cavity. The clock signal was directly taken from the transmitter for convenience and the clock extraction scheme described in Sec. 3.3.1 was used to synchronize the optical sampling system to the transmitter. The GT-UNI was operated using PMF2 with a DGD of 3.3 ps.

Fig. 5.5 shows measured eye diagrams for the three data signal wavelengths of 1535 nm, 1545 nm and 1555 nm with a persistence of 200 traces [36]. These wavelengths were the same as those used in the experiments described before on the characterization of the wavelength range of the GT-UNI based sampling system (Sec. 4.1.3). As discussed there, they were limited by the tuning range of the TMLL inside the data transmitter and the by the gain bandwidth of the available EDFA. The GT-UNI based sampling system provided clear open eyes with no ringing over the entire wavelength range of 18 nm similar to the NOLM based sampling system described in the previous section.

The evaluation of the measured eye diagrams yielded FWHM values of  $2.72 \pm 0.06$  ps,  $2.502 \pm 0.012$  ps and  $2.7 \pm 0.3$  ps for the data signal wavelengths of 1535 nm, 1545 nm and 1555 nm, respectively. Thus the high timing resolution of the GT-UNI sampling gate generated well separated eye diagrams with an average width of 2.6 ps over the entire wavelength range. The fact that this value was slightly smaller than the DGD of the PMF used in the GT-UNI sampling gate, is attributed



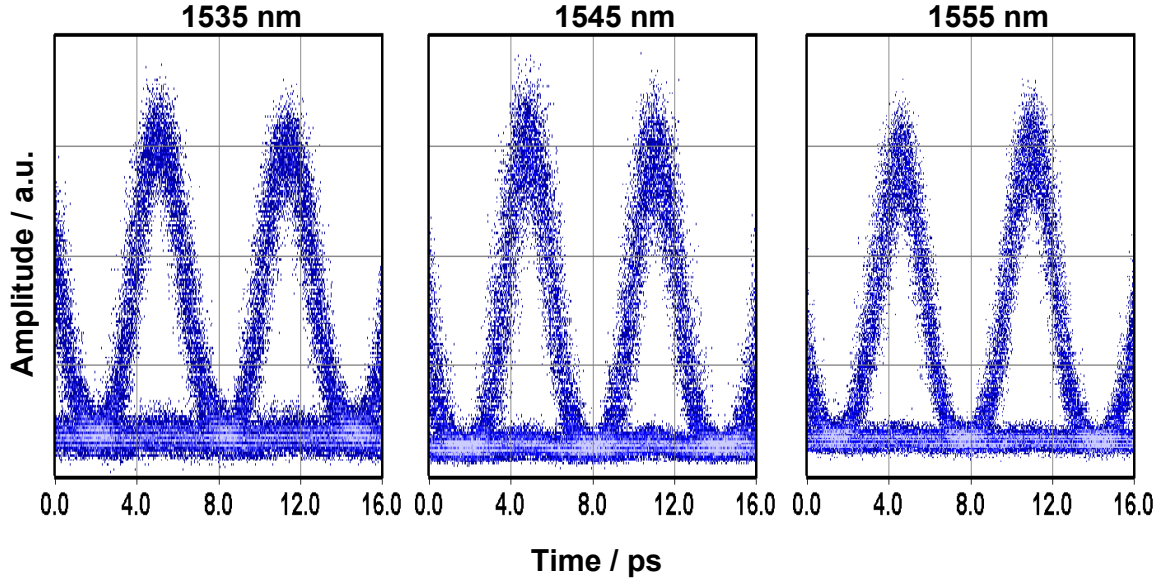


Figure 5.5: 160 Gbit/s eye diagrams at three different data signal wavelengths measured with the GT-UNI based sampling system.

to a phase shift of less than  $\pi$  inside the SOA of the sampling gate as discussed in Sec. 3.1.1. The shapes of the different eye diagrams revealed, that the data signal was not disturbed by the sampling gate in the GT-UNI based sampling system and thus all eye diagrams had equal shapes.

Regarding the RMS timing jitter, values of  $318 \pm 35$  fs,  $346 \pm 48$  fs and  $260 \pm 62$  fs were derived for the three wavelengths, respectively. These values differ slightly from wavelength to wavelength which was due to the variation of the timing jitter of the pulse source inside the transmitter as was confirmed by SSB noise measurements. However, in comparison to the measured jitter values using the NOLM based sampling system, the GT-UNI based sampling system yielded significantly lower jitter values. This was due to the lower timing jitter of the sampling pulse source #1 which was used in conjunction with the GT-UNI sampling gate.

Next, the length of the PMF fiber inside the GT-UNI sampling gate was varied. Fig. 5.6 shows measurements of 160 Gbit/s eye diagrams for three PMF samples having the DGD values of 6.5 ps, 3.3 ps and 2.0 ps. As expected, the FWHM of the eye diagrams decreases with decreasing length of the PMF fiber. It should be noted that the actual pulse width of the data signal under investigation was less than 1.5 ps in all three cases and thus the FWHM of the eye diagrams was limited by the timing resolution of the optical sampling system. Using the longest PMF fiber (left figure), the sampling system achieves a timing resolution for which the adjacent 160 Gbit/s eye diagrams just start to overlap. The measurements with PMF2 and PMF3 yield well separated eyes. The evaluation of the FWHM of the measured eye diagrams was already presented in Sec. 4.1.1. It was shown that the bandwidth of the optical sampling system increased from about 73 GHz for PMF1 to about 257 GHz for PMF3. At the same time, the jitter measured from all three eye diagrams yielded

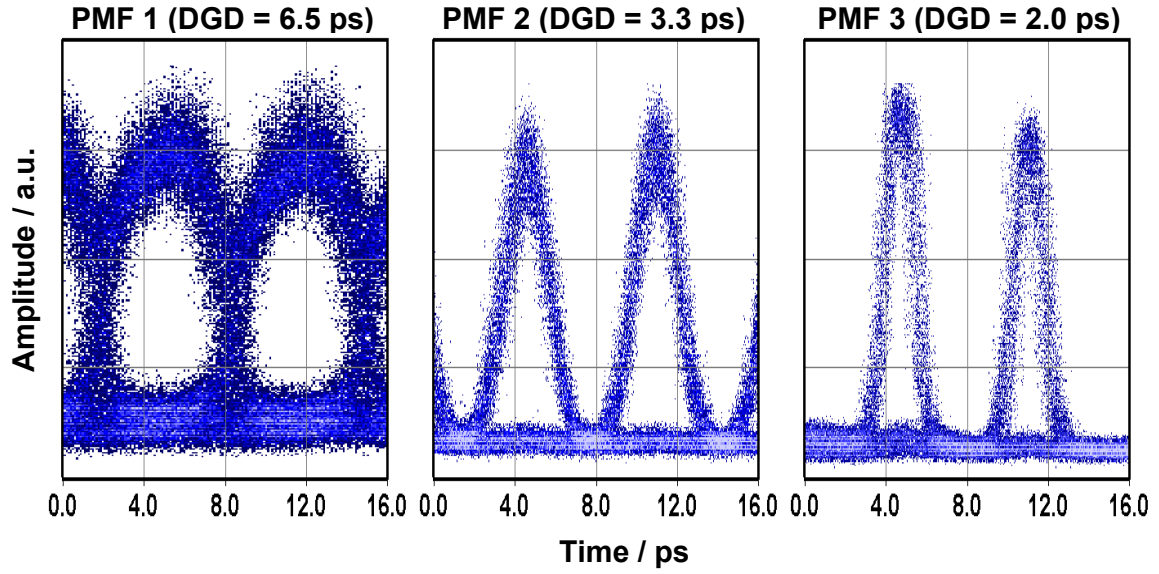


Figure 5.6: 160 Gbit/s eye diagrams measured with the GT-UNI based sampling system with different PMF fibers inside the sampling gate.

about the same value. Averaging over all measurements, a mean value of  $285 \pm 28$  fs was found.

The combination of high temporal resolution and low timing jitter of the optical sampling system allowed to visualize for the first time the eye diagram of a quasi 320 Gbit/s optical data signal using a semiconductor based optical sampling system [37]. In this experiment, a pulse compression stage was inserted in the optical

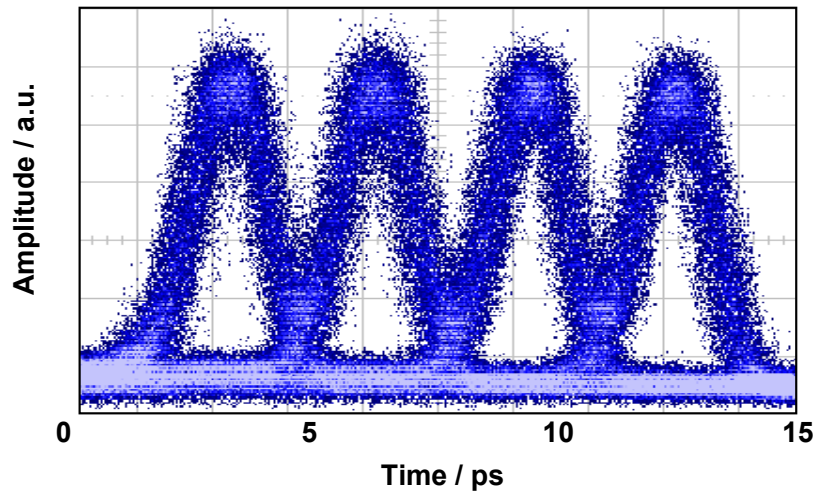


Figure 5.7: 320 Gbit/s eye diagram measured with the GT-UNI based sampling system with PMF3.

data transmitter after the modulator. The compressor exploited supercontinuum generation in a HNLF as described in Sec. 3.2.2. The TMLL inside the transmitter was set to 1552 nm and a roughly 15 nm wide supercontinuum was generated, from which the compressed data signal was filtered out by a 5 nm bandpass filter at 1550 nm. The FWHM of the compressed data pulses was measured by autocorrelation to be 600 fs. Then the transmitter was set to "M00011" to generate a 4-channel pseudo 320 Gbit/s data signal. The average input power of the data signal was +23 dBm at the input of the GT-UNI sampling gate.

Fig. 5.7 shows the measured eye diagram. Again, all eyes are clearly open and no ringing occurs. The RMS timing jitter is equal to the values just derived from the measurement at 160 Gbit/s. The adjacent eyes slightly start to overlap because the width of the eyes (see Fig. 5.6 for PMF3) is slightly larger than half of the bit period of 3.125 ps. So far, this represents the eye diagram measured at the highest data rate using a semiconductor based optical sampling system.

### 5.2.3 Random Sampling System

As discussed in Sec. 3.4.3 it is possible to construct an optical sampling system without synchronization of the sampling pulse source. This type of random sampling system was used in combination with a fiber laser as pulse source and a special fiber based sampling gate (Kerr gate) to measure 160 Gbit/s eye diagrams. This will be described in the present section.

**Set-up:** The detailed set-up of the experiment is depicted in Fig. 5.8. The sampling pulse source was a mode-locked Erbium doped fiber laser (ML EDFL, "Femtolite 780" by IMRA America Inc.). It emitted optical pulses with 48 MHz repetition rate

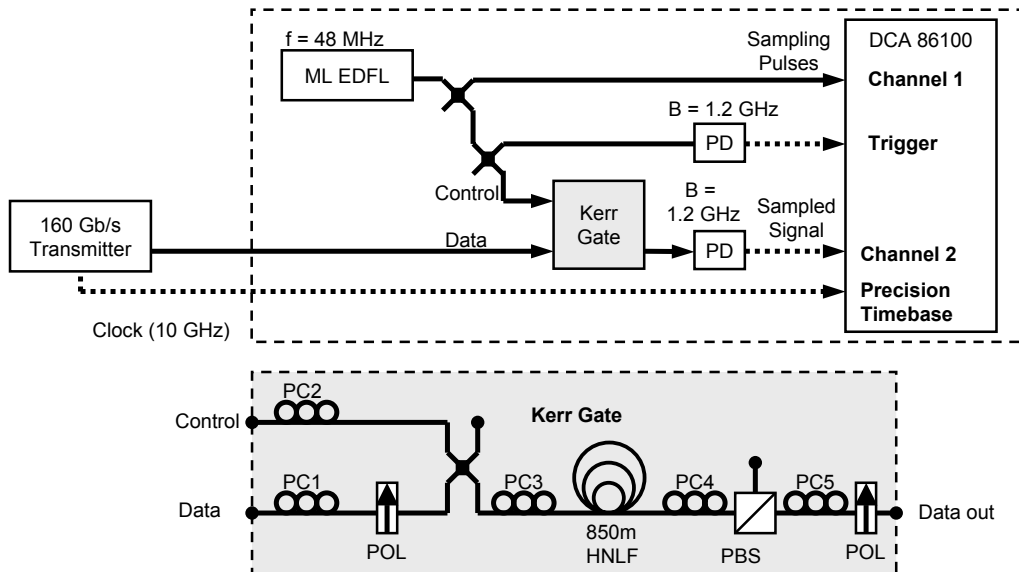


Figure 5.8: Set-up for the measurements using the random sampling set-up.



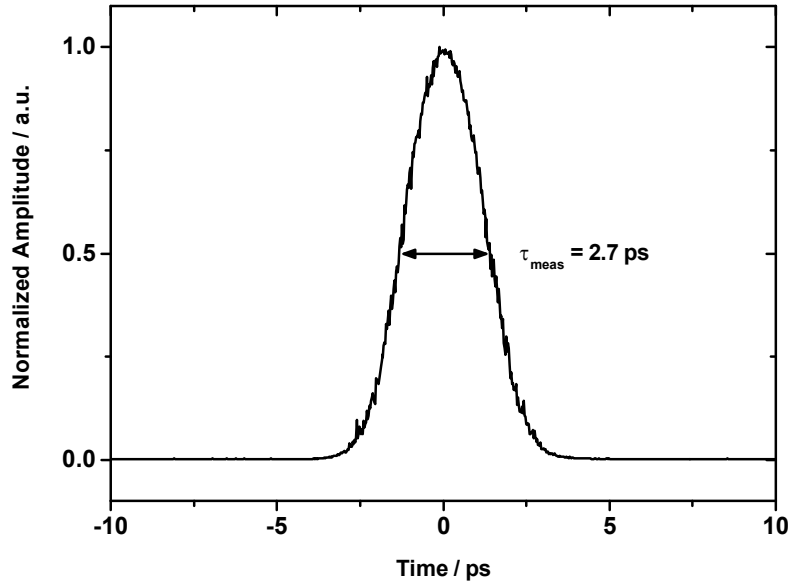


Figure 5.9: Waveform of a 1.7 ps pulse as measured by the Kerr sampling gate.

at a wavelength of 1560 nm. The sampling pulses were split using a 3 dB coupler and one part of the sampling pulses was fed into channel 1 of a 4-channel electrical sampling oscilloscope ("Infinium DCA86100" by Agilent). The second part of the sampling pulses was split again using another 3 dB coupler and was partly detected by a photodetector with 1.2 GHz electrical bandwidth. This signal was used as trigger for the electrical sampling oscilloscope. The remaining part of the sampling pulses was finally used as control signal for the optical sampling gate. The sampling gate was a Kerr gate which is depicted in detail in the lower part of Fig. 5.8. The output of the sampling gate was detected by another photodetector with 1.2 GHz electrical bandwidth and finally fed into channel 2 of the electrical sampling oscilloscope. The reference clock for the precision timebase of the sampling oscilloscope was an electrical 10 GHz signal which was directly taken from the data transmitter. An optical clock recovery was omitted in this experiment for convenience.

The Kerr gate is based on cross-phase modulation (XPM) induced polarization rotation in 850 m of highly nonlinear fiber (HNLF) [85]. The data signal passed a polarizer (POL) to ensure a single polarization. Next, the data signal was coupled into the HNLF and the polarization controller PC4 was adjusted such that the data signal was completely reflected at the polarization beam splitter (PBS). Then the sampling pulses, i.e. the control signal, was fed into the HNLF using a 3 dB coupler. The polarization of the control signal was adjusted using PC2 such that optimum XPM occurred. Thus in the presence of a sampling pulse, the polarization of the data signal was rotated and the signal passed the PBS. The extinction of the Kerr gate was further improved by adding a second polarizer/analyzer at the output of the set-up.

**Measurements:** First, the temporal resolution of the Kerr gate was measured. For this experiment, the transmitter was set to "U0000", i.e. a 10 GHz pulse train

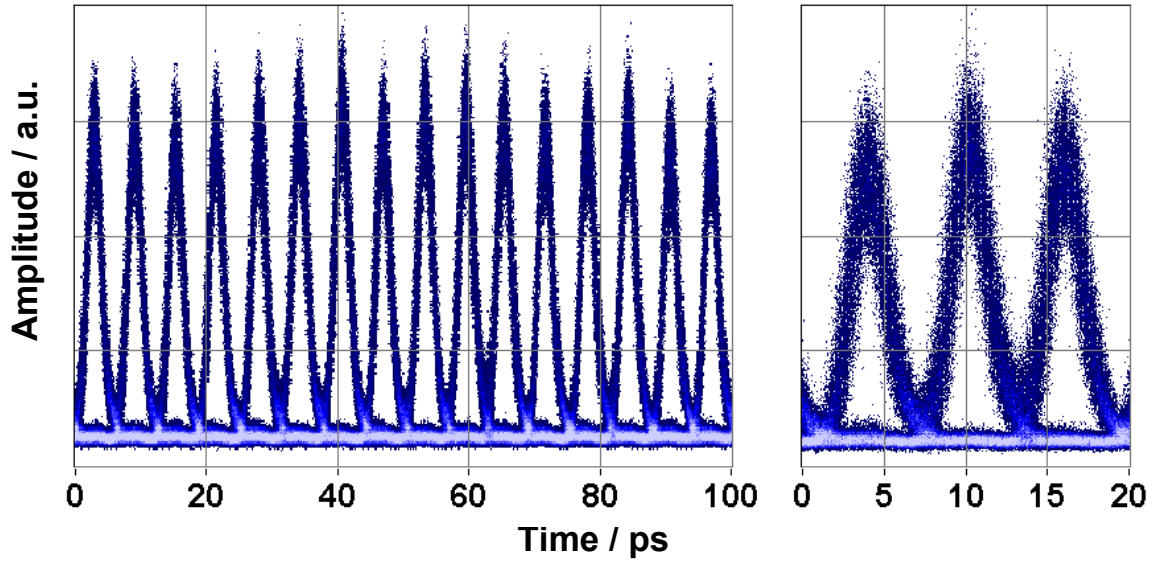


Figure 5.10: 160 Gbit/s eye diagram measured with the random optical sampling system. The right figure shows an enlarged detail.

was measured using the random sampling system. The normalized trace is shown in Fig. 5.9. Here, the sampling system was operated in the averaging mode. A width (FWHM) of  $\tau_{meas} = 2.7$  ps was obtained. Considering the finite pulse width of the signal pulses of  $\tau_{SP} = 1.7$  ps at the input of the HNLF (measured by an autocorrelator), the gating window width of the Kerr gate was calculated to be  $\tau_{GW,Kerr} = 2.1$  ps which corresponds to an optical bandwidth of 210 GHz.

Next, the transmitter was set to "M1111" and the sampling system was used to record the eye diagram of a 160 Gbit/s data signal. The result is shown in Fig. 5.10. The enlarged detail on the right hand side of the figure shows that all eyes were clearly open. The eyes showed a slight asymmetry in the steepness of the flanks which indicates that the data signal pulses had a steeper rising edge than falling edge. Also, the eyes from adjacent channels slightly overlapped. The average FWHM of the measured eyes was  $2.63 \pm 0.04$  ps. The average timing jitter of the measured eyes was  $337 \pm 24$  fs. Due to the random sampling principle, this timing jitter is not limited by the jitter of the sampling pulse source as in the conventional optical sampling set-up. Instead it is limited by the jitter of the oscilloscope timebase which is used to measure the arrival times of the optical sampling pulses. The jitter of the timebase was measured to be about 200 fs so that the jitter of the data signal was calculated to be about 270 fs.

Finally, the random sampling set-up was used to compare the performance of two different optical pulse sources inside the 160 Gbit/s data transmitter. Both pulse sources were tunable mode locked semiconductor lasers. Fig. 5.11 shows the measured eye diagrams of both pulse sources when the transmitter was set to "M0000", i.e. it produced a 10 Gbit/s data signal. From the measured eye diagrams it is obvious that transmitter #1 exhibited significantly larger timing jitter than transmitter #2.

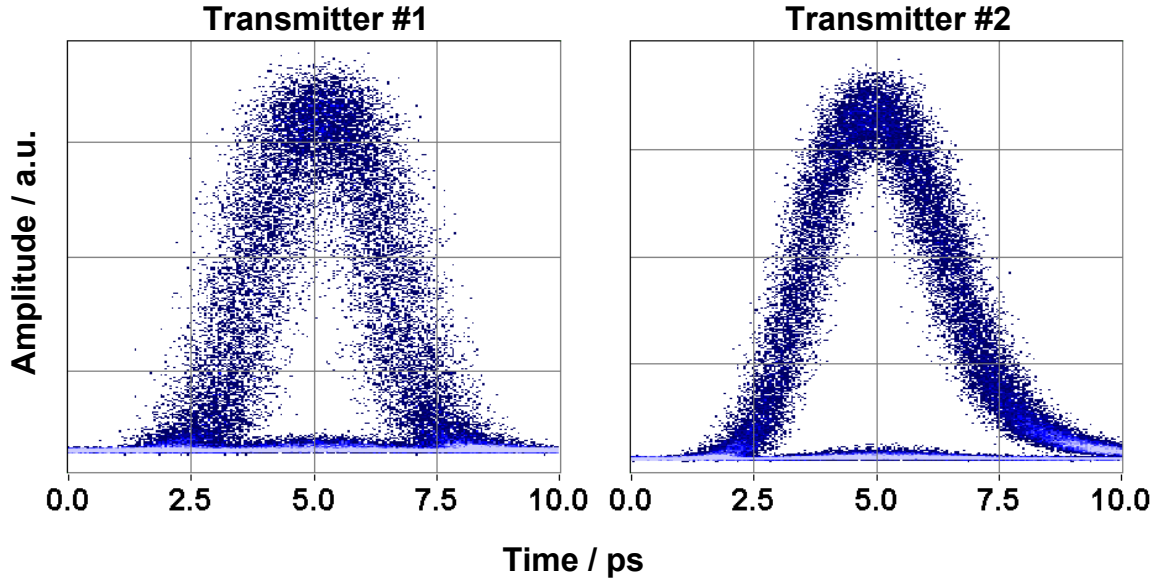


Figure 5.11: 10 Gbit/s eye diagrams of two different transmitters measured with the random optical sampling system.

The horizontal histograms yielded a value of 503 fs for transmitter #1 and 306 fs for transmitter #2. Considering the jitter of the sampling system (200 fs) this yielded jitter values of 460 fs and 230 fs for the two transmitters, i.e. transmitter #1 had about twice the jitter as transmitter #2.

Due to the high temporal resolution of the random sampling set-up with the KERR gate it is also possible to detect a significant difference in the pulse shape of the two transmitters. , Fig. 5.11 reveals that transmitter #1 shows an almost symmetric pulse shape whereas the pulses from transmitter #2 are asymmetric and exhibit a steeper rising than falling edge.

Using a vertical histogram in the center of the eye, the extinction ratio was measured from the eye diagram. It was found to be 21 dB for both transmitters. As this value was limited by the extinction of the  $\text{LiNbO}_3$  modulator inside the transmitter, it was the same for both configurations.

It should be noted however, that in the histogram evaluation of the eye diagram it is not possible to distinguish between timing jitter and amplitude noise. In the example of Fig. 5.11 the vertical histogram yielded a Q-value of 7.6 for transmitter #1 while the Q-value for transmitter #2 was 14.0. When comparing the Q-values one could thus argue that transmitter #1 had a worse signal to noise ratio instead of or in addition to a larger timing jitter. This ambiguity generally can only be solved by conducting additional independent measurements that are sensitive to one of the quantities only, like for example SSB noise measurements for the timing jitter.

### 5.2.4 Conclusion of Eye Diagram Measurements

In conclusion, all three sampling systems allowed the measurement of eye diagrams at least up to a data rate of 160 Gbit/s.

The NOLM gate had the highest temporal resolution of 1.5 ps corresponding to an optical bandwidth of 294 GHz. The GT-UNI based system had a slightly lower optical bandwidth of 257 GHz when using PMF3. Due to the low timing jitter of the sampling pulse source #1 used to control the GT-UNI gate it was possible to measure the eye diagram of a 320 Gbit/s data signal for the first time with a semiconductor based optical sampling system.

The optical bandwidth of the random sampling system with the Kerr gate was 210 GHz. This value was limited by the pulse width of the sampling pulses used. It can be expected that an optical bandwidth similar to the bandwidth of the NOLM gate is achieved if the same short sampling pulse width is used. In that case it can be expected that the measurement of a 320 Gbit/s eye diagram will be possible with this system since the timing jitter of the random sampling system was only 200 fs (limited by the timing jitter of the oscilloscope timebase).

Both, the NOLM and the GT-UNI sampling gate were operated over a wavelength range of about 20 nm. The wavelength range of the Kerr sampling gate was not explicitly investigated but it can be assumed that it is similar to the NOLM gate because the same nonlinear medium and nonlinear effect was used.

Additionally, Fig. 5.11 shows that the amplitude variation in the baseline of the measured eye diagrams was significantly lower in the case of the random sampling system as compared to the conventional sampling system (see Fig. 5.5 for example). This improvement is attributed to the fact that the sampling pulse source was directly operated at 48 MHz and no external sampling pulse suppression was necessary. In the conventional set-up, the imperfect pulse suppression broadens the baseline because the amplitude of each individual optical sample is superimposed by some part of the signal that is unintentionally gated by the suppressed sampling pulses.

## 5.3 160 Gbit/s Transmission Experiments

This section describes 160 Gbit/s transmission experiments in which the optical sampling system was used to analyze certain distortions of the data signal. This is done by evaluating the measured eye diagrams after the fiber transmission. The investigated effects are the signal-to-noise ratio (SNR) reduction, the effect of the fiber nonlinearity and the effect of residual chromatic dispersion of the fiber. The analysis of the signal distortions due to the nonlinearity and the residual chromatic dispersion of the fiber are supported by numerical simulations. The algorithm used in the numerical simulations is described in detail in Appendix A.2.

### 5.3.1 Signal-to-Noise Ratio

It has been addressed that in-service quality monitoring of high bit rate optical transmission systems can be achieved at the full line rate by using an optical sampling

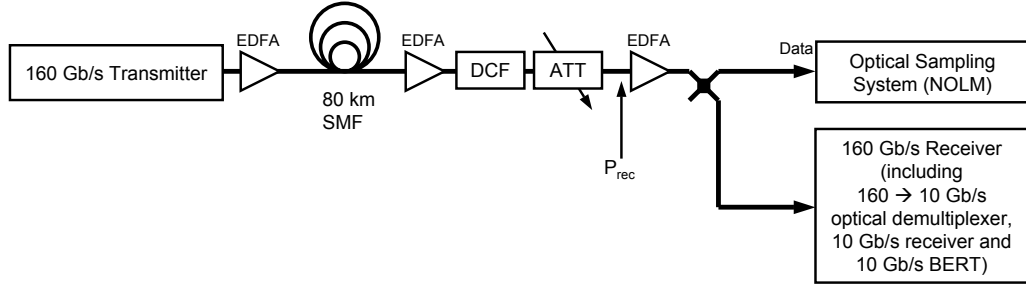


Figure 5.12: Schematic set-up of the Q-factor evaluation in a 160 Gbit/s transmission experiment using the NOLM based sampling system.

system. Although a number of experiments have been published so far which emphasize the high temporal resolution and low timing jitter of such systems, only few work was reported so far on a quantitative analysis of those eye diagrams [86]. In addition, this evaluation was only based on asynchronous histograms [87, 88, 89, 90]. This section presents a quantitative evaluation of synchronously measured 160 Gbit/s eye diagrams [13, 91]. The eye diagrams were measured after transmission over 80 km of standard single mode fiber (SMF).

**Set-up:** The experimental set-up is shown in Fig. 5.12. The 160 Gbit/s optical transmitter is described in detail in the Appendix (Sec. A.1). The signal was amplified and launched into the fiber link which consisted of 80 km of standard single mode fiber (SMF). After the SMF, the signal was amplified to compensate for the losses of the SMF link. Then it was fed into a dispersion compensating fiber module (DCF) to compensate for the accumulated chromatic dispersion of the SMF. After the DCF, the signal-to-noise ratio (SNR) of the optical data signal was degraded by a variable attenuator and a subsequent EDFA.

After the EDFA, the signal was split using a 3 dB-coupler. One part of the signal was fed into the NOLM based optical sampling system. The other part of the signal was fed into a 160 Gbit/s receiver, which comprised an optical demultiplexer from 160 Gbit/s to 10 Gbit/s [53], a 10 Gbit/s opto/electrical receiver and a 10 Gbit/s bit-error rate test set (BERT). The BERT was used to measure the bit-error rate (BER) of the data signal as a function of the received optical power  $P_{rec}$  (average power), which was measured after the attenuator. Please note that in order to synchronize both the optical sampling system and the 160 Gbit/s receiver, the optical clock recovery in the gain-transparent configuration as described in Sec. 3.3.2 was used. This means that the optical sampling system was operated as a complete system with only a single optical input, namely the 160 Gbit/s data signal. To synchronize the 160 Gbit/s receiver, the recovered 10 GHz clock signal from the optical sampling system was shared with the 160 Gbit/s receiver.

**Results:** The BER curve for the transmission experiment is shown in Fig. 5.13. The plot shows two sets of data. The triangular symbols show the BER performance in the

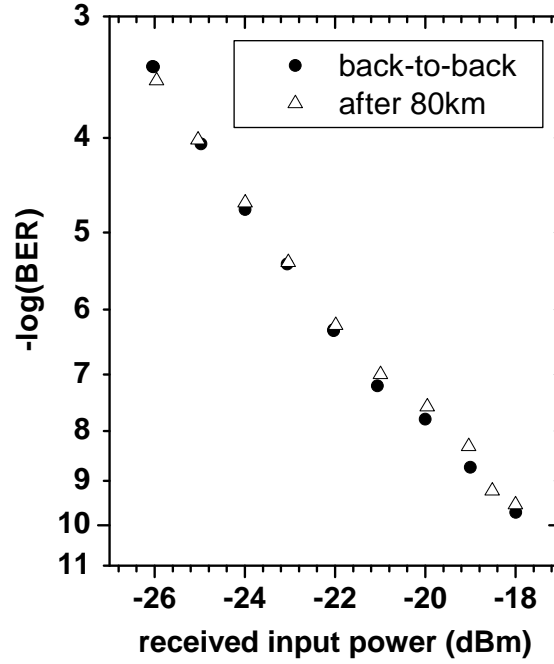


Figure 5.13: Measured bit-error rate as a function of the received power at 160 Gbit/s in a back-to-back configuration and after 80 km transmission.

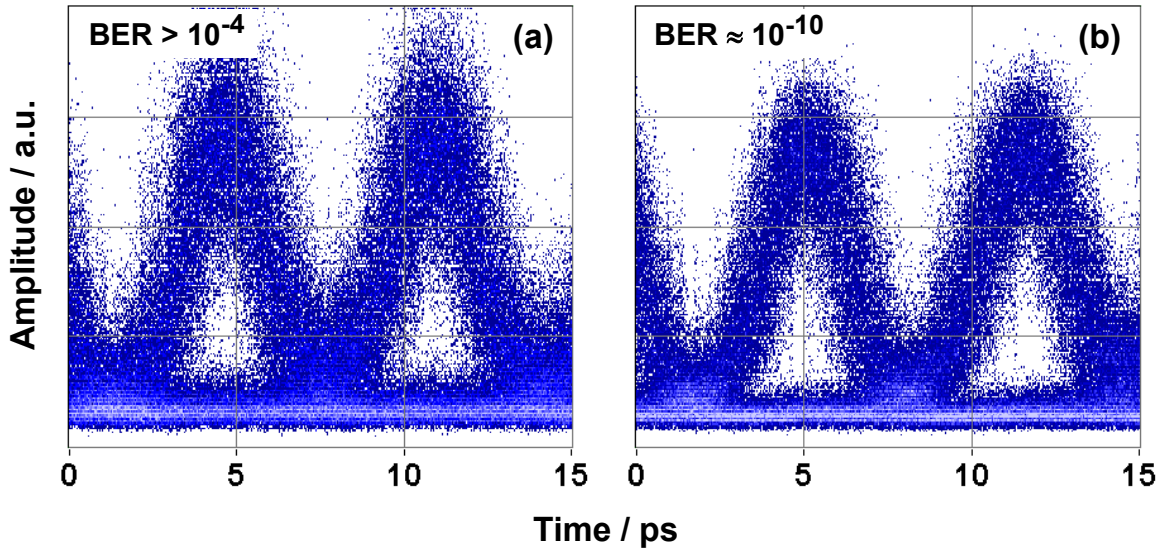


Figure 5.14: Measured optical eye diagrams at 160 Gbit/s for a received input power of -26 dBm (a) and -18 dBm (b).

back-to-back configuration, i.e. when the 160 Gbit/s receiver was directly connected to the 160 Gbit/s transmitter. The circular symbols show the BER performance when the data signal was transmitted over the 80 km fiber link. The plot shows that the



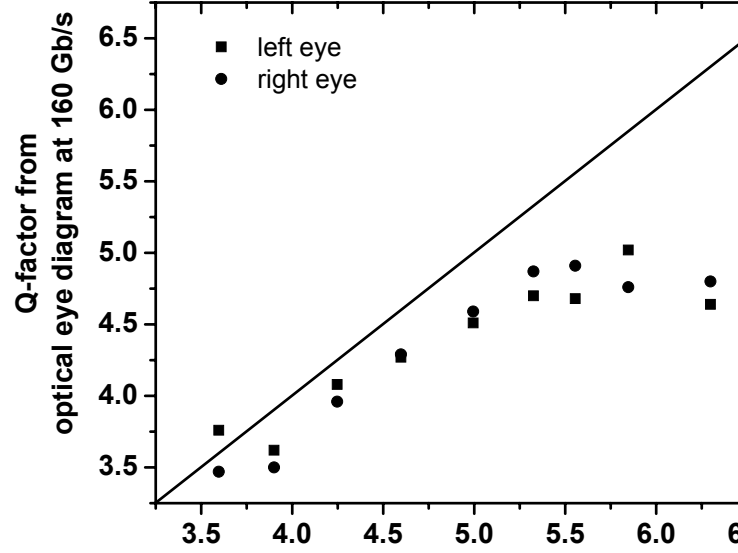


Figure 5.15:  $Q$ -factor of the left (squares) and right (circles) channel eye diagram measured with the optical sampling system at 160 Gbit/s as a function of the  $Q$ -factor calculated from the measured BER.

BER increases with decreasing received power, i.e. decreasing signal-to-noise ratio at the receiver. Error free transmission ( $\text{BER} < 10^{-9}$ ) was achieved for a received power of approximately -19 dBm in the back-to-back configuration as well as after the fiber transmission. This means that the fiber transmission did not induce a penalty.

Fig. 5.14 shows as an example two 160 Gbit/s eye diagrams measured by the NOLM based optical sampling system. Due to the high timing resolution of the optical sampling gate, the individual channels of the optical data signal are clearly resolved. Due to the optical clock recovery, eye monitoring was possible at the output of the link with a large persistence time of 1 s. The two eye diagrams were recorded for received optical powers of -26 dBm and -18 dBm, which corresponded to bit-error rates of  $> 10^{-4}$  and  $10^{-10}$ , respectively (see Fig. 5.13). It can be seen that the vertical eye opening decreased with decreasing received power and increasing bit-error rate.

Next, the  $Q$ -factor  $Q_{eye}$  was derived from the optical eye diagrams using the procedure described in Sec 2.4. Simultaneously, the measured bit-error rate was converted into a  $Q$ -factor  $Q_{BER}$  using Eq. (2.58).

Fig. 5.15 shows  $Q_{eye}$  as a function of  $Q_{BER}$ . Since each recorded eye diagram covered the eyes of two adjacent OTDM channels, the plot shows two sets of data for the left and right eye. Ideally, the  $Q$ -factor should be the same for both eyes. The difference between the left and the right eye is an indication of the limited precision of the 160 Gbit/s transmitter as well as the eye diagram evaluation. Assuming no signal degradation by the optical demultiplexer inside the 160 Gbit/s receiver and assuming no influence of the optical sampling system on the  $Q$ -factor measurement,

all measured values of  $Q_{eye}$  should be found on the solid line representing the 1:1 correlation between the two axes.

**Conclusion:** It can be seen that in general the measured Q-values from the eye diagram are lower than the corresponding Q-values calculated from the bit-error rate measurements. Still, a good correlation can be seen for low Q-values up to about 4.5. For Q-values larger than 5.0 however, the measured Q-values from the eye diagrams saturate.

This result is attributed mainly to two effects. The first deteriorating effect was the timing jitter of the measured eye diagrams. Since for the RZ data format, the mark contour line was very narrow, measured data points from the flanks leaked into the vertical histogram centered at the peak amplitude position of the eye diagram. The higher the timing jitter of the eye diagram, the more data points leaked into the histogram and broadened the measured mark level distribution. The result of this was that all derived Q-values were lower than expected.

Secondly, due to the transmission loss inside the optical sampling gate and the subsequent amplification in the O/E-receiver block of the sampling system, the signal-to-noise ratio of the data signal under investigation was degraded by the sampling system itself. This led to the observed saturation in measured Q-values for data signals with good SNR.

### 5.3.2 Fiber Nonlinearity

In high-speed fiber-optic transmission systems (40 Gb/s and above), the maximum fiber input power which allows for error-free transmission is limited due to the nonlinearity of the fiber for single channel transmission. The nonlinearity gives rise to mainly two nonlinear effects known as intra-channel cross-phase modulation (IXPM) and intra-channel four-wave mixing (IFWM) [92,93]. While IXPM results in an increase of the jitter of the data signal, IFWM is responsible for the generation of so-called "ghost pulses". IFWM has been studied extensively using simulations [94,95]. However, experimental investigation of IFWM has been limited to bit-rates of 40 Gbit/s up to now [92,96] due to the limited bandwidth of photodetectors and electrical sampling oscilloscopes. This section describes the first experimental and numerical investigation of the generation and dynamics of ghost pulses due to IFWM at a data rate of 160 Gbit/s using the optical sampling system [38].

**Set-up:** The experimental set-up is depicted in Fig. 5.16. For these experiments, the optical pulse source inside the 160 Gbit/s transmitter was replaced by a passively mode-locked solid state laser (MSSL) ("ERGO PGL" by Gigatera, Switzerland). An isolator was placed at the output of the MSSL to reduce instabilities of the laser due to back-reflections from fiber connectors. Also, a short piece of dispersion compensating fiber (DCF) was inserted after the isolator to compensate the almost linear chirp of the MSSL laser pulses. The transmitter was set to "M00010" to generate a quasi 160 Gbit/s optical data signal as described in the Appendix (Sec. A.1).

The data signal was then amplified and launched into 80 km of non-zero dispersion shifted fiber (NZDSF) ("TeraLight Ultra" by Alcatel). At the output of the fiber



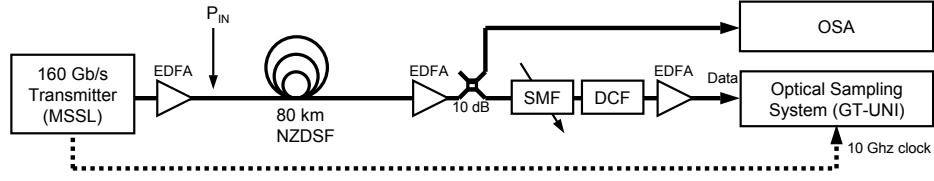


Figure 5.16: *Experimental set-up for the investigation of fiber nonlinearities using the optical sampling system.*

link, the signal was amplified again to an average output power of +0.0 dBm and split using a 10 dB coupler. The low power branch of the coupler was connected to an optical spectrum analyzer (OSA) with 0.01 nm resolution bandwidth. The high power output of the coupler was fed into a dispersion compensation stage which consisted of a variable amount of standard single mode fiber (SMF) and a fixed amount of dispersion compensating fiber (DCF). The SMF was used to adjust precisely the dispersion compensation of the transmission link. To achieve full chromatic dispersion compensation for this link, a total SMF length of 600 m was inserted. The pulse width of the RZ data signal was 1.6 ps (FWHM) at the input and at the output of the fiber link, as measured by an autocorrelator for a 10 Gbit/s data signal with low link input power. The dispersion compensated data signal was amplified again to compensate for the losses inside the SMF and DCF modules. Finally, the optical eye diagrams of the data signal were measured with the GT-UNI based optical sampling system. This time, the GT-UNI was operated with PMF2.

For these measurements, a direct 10 GHz RF clock line extraction at the data transmitter was used as described in Sec. 3.3.1. Due to the long length of the transmission link, the extraction of the clock before the fiber link caused a slow temporal drift of the measured eye diagrams with respect to the clock signal. However, since the acquisition time for one eye diagram was typically about 2 ms, the measurements were not hampered by this drift.

A manual polarization controller (not shown in Fig. 5.16) was placed at the input of the fiber link to compensate for polarization mode dispersion (PMD) by launching the data signal into one of the principle axes of the transmission link. The main contribution to the PMD of the link was found to arise from the birefringence of the DCF-modules, while the PMD of the transmission fiber itself was negligible. Therefore, the principal axes of the transmission span did not vary with time and the polarization controller could be adjusted once before the experiments.

In the measurements, the optical 160 Gbit/s eye diagrams at the output of the transmission link as well as the corresponding optical spectra were recorded as a function of the peak power  $P_{in}$  of the data signal at the input of the link as indicated in Fig. 5.16.

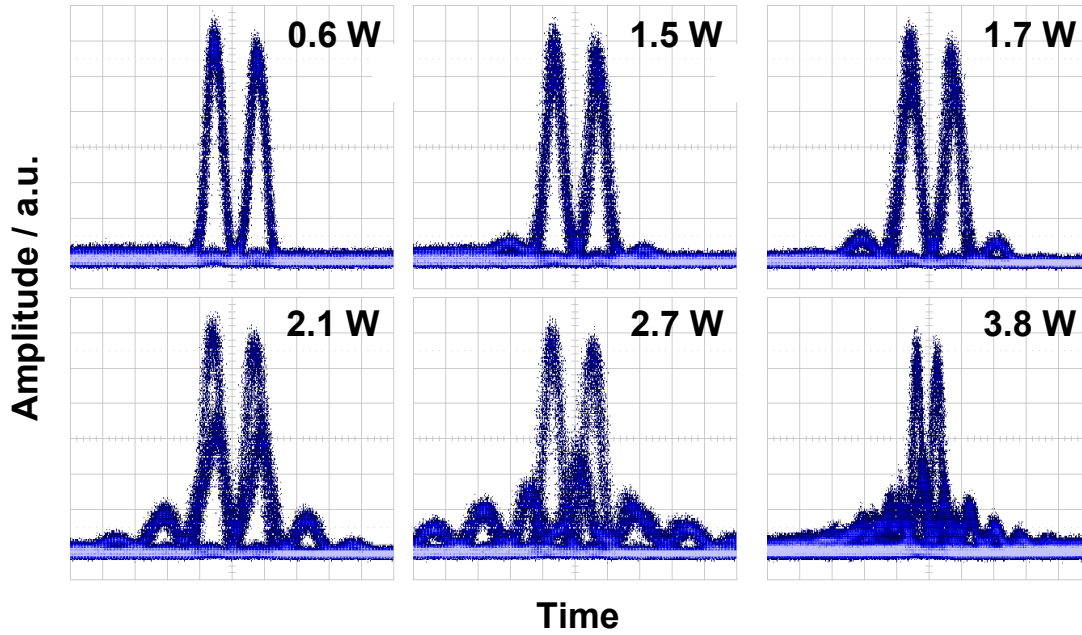


Figure 5.17: Eye diagrams of 2 channel data signal for different input peak powers. Each diagram shows a time segment of 49 ps, with the exception of the diagram for 3.8 W, which shows 98 ps.

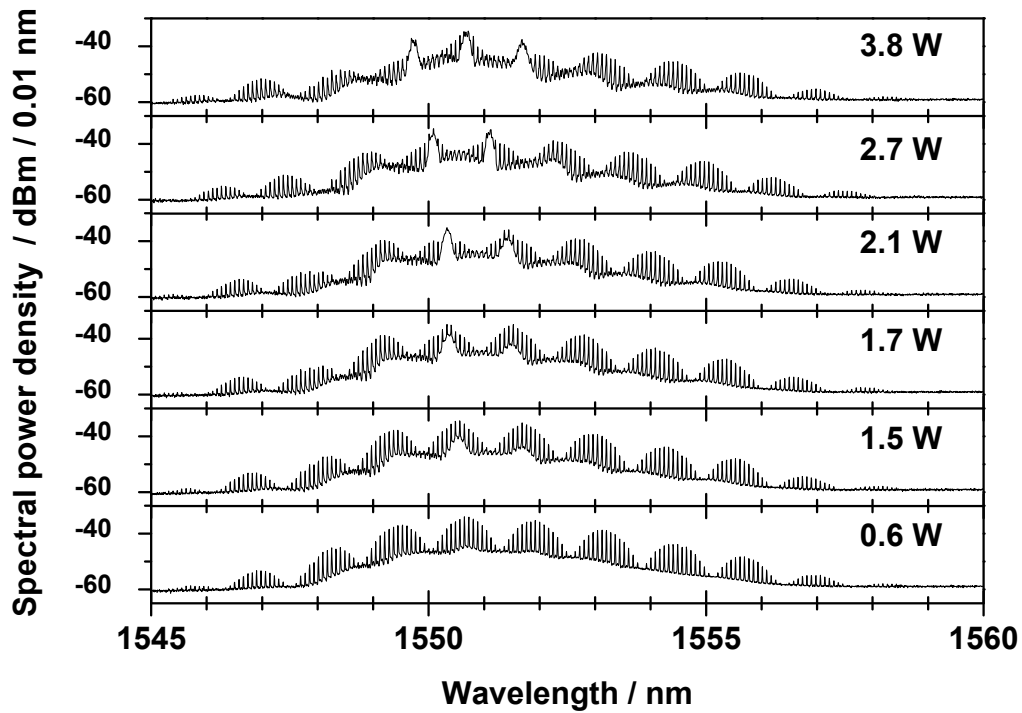


Figure 5.18: Optical spectra at the output of the NZDSF for different input peak powers.

**Experimental results:** Fig. 5.17 shows measured eye diagrams after the transmission link for different input peak powers  $P_{in}$ . It can be seen clearly, that with increasing peak power, part of the signal power was transferred to new positions in time due to intra-channel four-wave-mixing (IFWM). The newly generated signal components formed so called "ghost"-eyes and appeared before and after the actual data channels. When increasing the pulse peak power above 2 W, even higher order ghost-eyes were generated.

The optical spectra corresponding to the eye diagrams are shown in Fig. 5.18. For 0.6 W input peak power, the spectrum was clean and the modes of the data signal could be identified (sharp "spikes" with a spacing of 10 GHz). The superstructure on the modes was due to the specific type of 160 Gb/s data signal in which only 2 channels were turned on. With increasing peak power, certain additional spectral peaks were generated. These peaks were broader than the modes. While at 1.7 W input power only 2 peaks were present, a third peak appeared at 3.8 W. Finally, an overall shift of the dips in the spectrum by about 1 nm to shorter wavelengths could be observed. This is attributed to a slow drift of the relative optical phase between the 2 OTDM channels of the data signal, which will be addressed further later in this section.

**Phenomenological description of IFWM:** Fig. 5.19 shows schematically the generation of ghost pulses due to the nonlinearity and chromatic dispersion of the fiber. Fig. 5.19a) shows two vertical bars which represent two optical pulses with a certain temporal spacing and spectral distribution. When propagating through fiber with local dispersion, each wavelength component propagates at a different group velocity and thus the two pulses broaden in time. The temporally broadened pulses are represented by the two tilted bars in Fig. 5.19b). Now the fiber nonlinearity causes four-wave mixing between different spectral components of the two pulses, which results in the grey bars (Fig. 5.19c) ). These newly generated spectral components are converted to the grey vertical bars in Fig. 5.19d) when the signal is propagated through the dispersion compensating fiber at the end of the transmission link. From

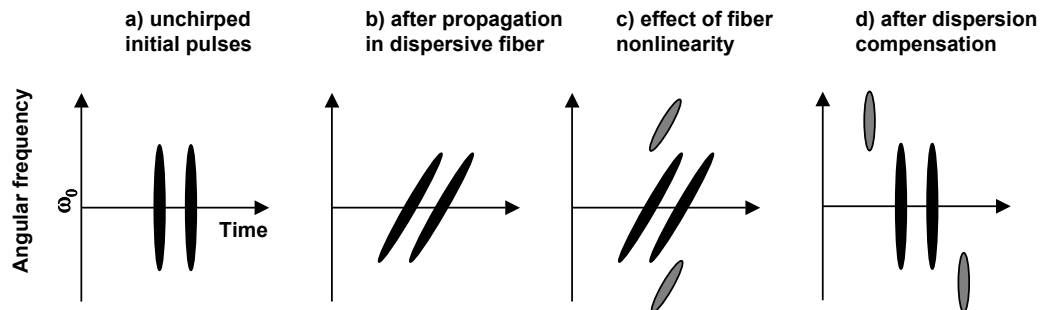


Figure 5.19: Schematic explanation of the generation of ghost pulses due to IFWM. Each line represents the optical pulse with a certain distribution of instantaneous wavelength over time at a position along the fiber.

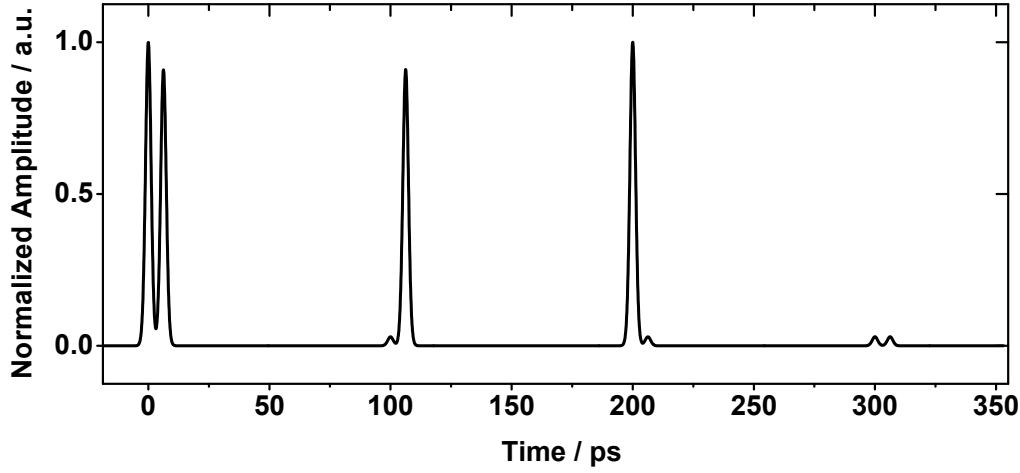


Figure 5.20: Train of pulses used for the numerical simulation. The plot shows the normalized amplitude  $|A|^2$  as a function of the time  $T$ .

Fig. 5.19 it can be seen that the newly generated spectral components lead to newly generated pulses – so called ”ghost pulses” – which appear temporally before and after the initial pulses.

**Numerical simulation:** Finally, the generation and dynamics of the ghost pulses was studied using a numerical simulation of the pulse propagation in an optical fiber. Details about the numerical simulation algorithm can be found in the Appendix (Sec. A.2). To simulate the 2-channel optical data signal, a bit-stream as shown in Fig. 5.20 was used. This bit stream contained four bit combinations (”1-1”, ”0-1”, ”1-0”, ”0-0”) which represented all possible bit combinations that were present in the experimental set-up. As can be seen from Fig. 5.20, a slight power asymmetry between the left and right channel of 9% was included in the simulation to account for an experimentally observed asymmetry in the optical multiplexer. The extinction of the data transmitter was assumed to be 15 dB. Therefore, the amplitude of the ”0”-bits is not zero but is 1/31 of the amplitude of the ”1”-bits.

The parameters used to simulate the transmission link of this experiment are listed

Table 5.1: Fiber parameters used in the numerical simulation of the nonlinearity investigation.

	$L$ / km	$\alpha \cdot L$ / dB	$D \cdot L$ / ps/nm	$S \cdot L$ / ps/nm <sup>2</sup>	$\gamma$ / (W km) <sup>-1</sup>
NZDSF	84.220	17.6	724	4.33	1.6
DCF	7.646	8.0	-734.87	-4.63	5.7
SMF	0.639	0.128	10.87	0.04	2
<b>Total</b>	<b>92.505</b>	<b>25.728</b>	<b>0.00</b>	<b>-0.26</b>	

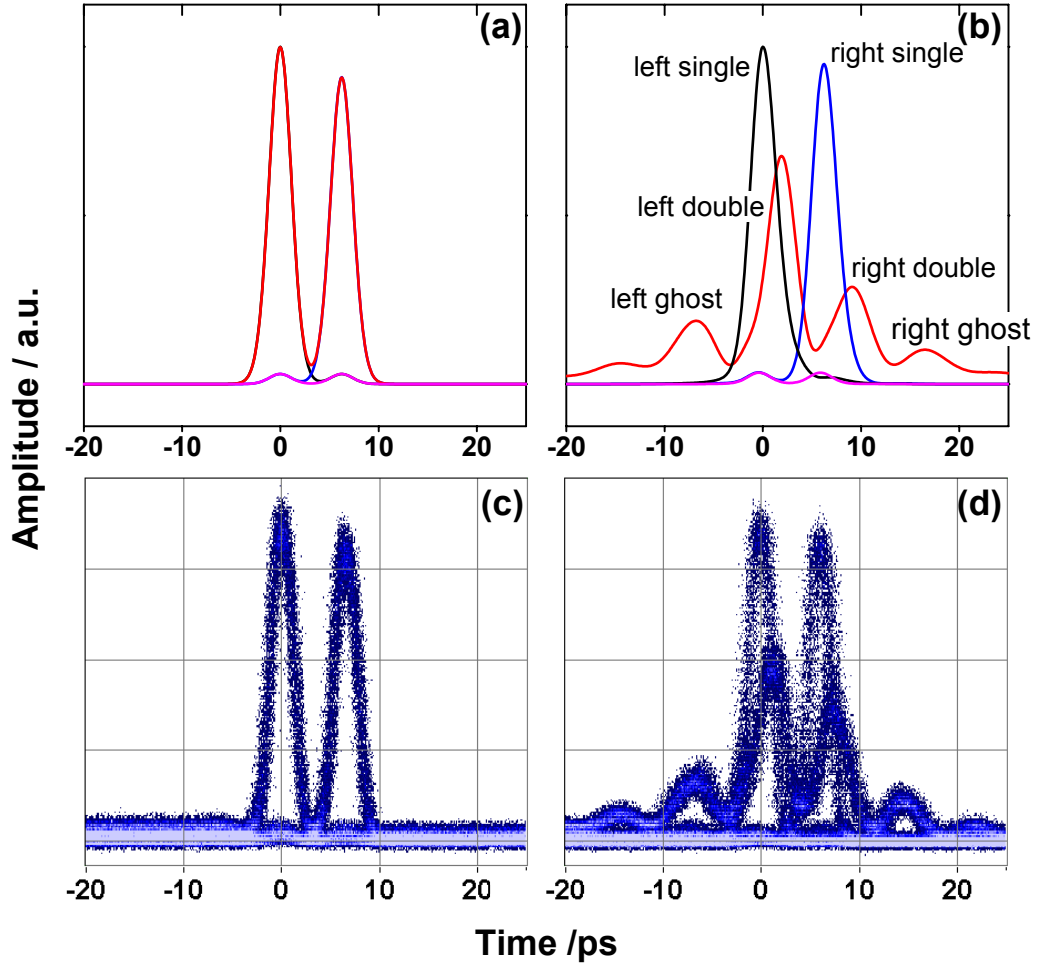


Figure 5.21: Simulated (a+b) and measured (c+d) eye diagrams after the fiber link for an input peak power of  $P_{in} = 0.6$  W (a+c) and  $P_{in} = 2.1$  W (b+d).

in Tab. 5.1. The values for the NZDSF and the DCF were taken from the manufacturer's data sheets and were specified with varying numerical precision as shown in the table. No tolerances were given for these data. The following standard values were assumed for the SMF:  $\alpha = 0.2$  dB/km,  $D = 17$  ps/nm km,  $S = 0.06$  ps/nm<sup>2</sup> km and  $\gamma = 2$  /W km. The table lists as columns the length  $L$  of each fiber together with the accumulated loss  $\alpha \cdot L$ , accumulated dispersion  $D \cdot L$ , accumulated dispersion slope  $S \cdot L$  and the nonlinearity coefficient  $\gamma$  of each fiber. The sum over the rows shows the total length of the transmission link (92.505 km) as well as the total loss (25.728 dB) and total accumulated dispersion. The total accumulated dispersion and dispersion slope are also often referred to as "residual dispersion"  $D_{res}$  and "residual dispersion slope"  $S_{res}$ . The length of the SMF (639 m) was chosen such that the residual dispersion of the transmission link was zero. However, the residual dispersion slope became  $S_{res} = -0.26$  ps/nm<sup>2</sup> in this case.

Fig. 5.21 shows the simulated eye diagrams (a+b) at the output of the fiber link together with the measured eye diagrams (c+d) for low and high input power into the

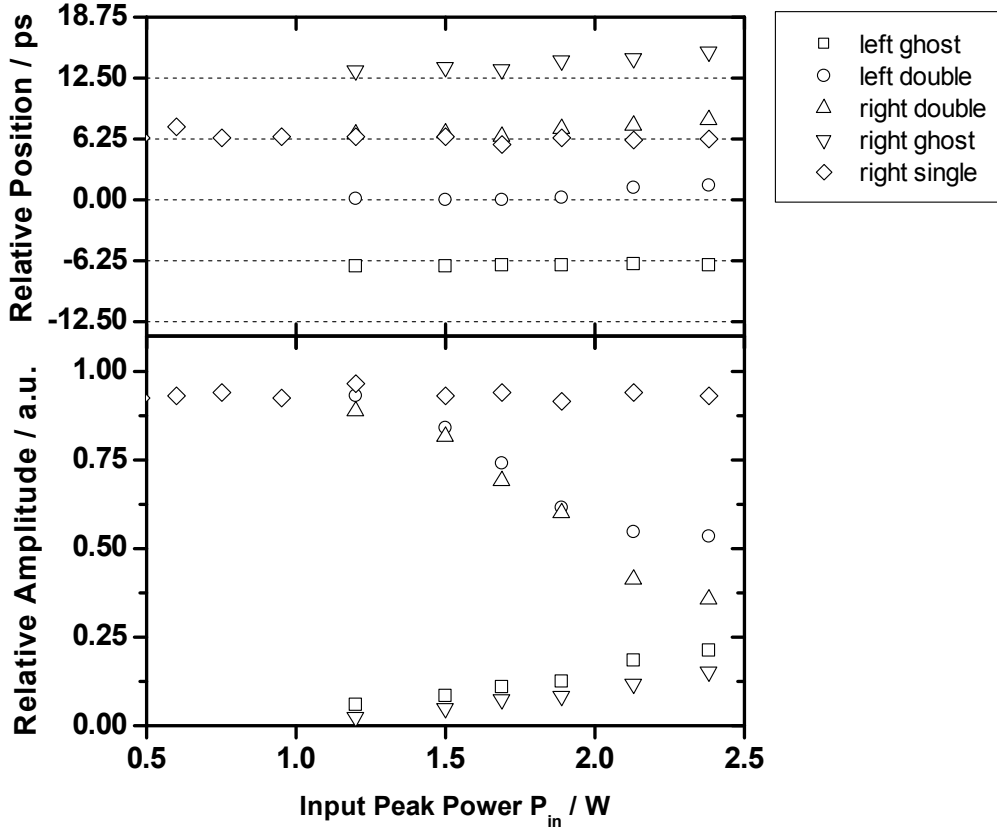


Figure 5.22: Relative amplitude and position of the peaks in the measured eye diagrams versus the input peak power.

fiber link. Since the simulated optical signal only consisted of eight individual pulses without timing jitter and amplitude noise, the simulated eye diagram represents the contour line of the measured eye diagrams.

The simulated eye diagram at the output of the link clearly shows the generation of ghost pulses due to IFWM. A number of peaks were identified and labelled as shown in Fig. 5.21b). In particular, the "1-0" and "0-1" bit combinations led to the "left (leading) single" and "right (trailing) single" peak, respectively. The "1-1" combination led to the "left double" and "right double" peak as well as the IFWM "ghost" peaks. These peaks were also present in the measured eye diagram (d) showing a good agreement between the simulation and the measurement.

**Evaluation of measured eye diagrams:** Next, the measured eye diagrams were evaluated. The evaluation concentrated on the amplitudes and temporal positions of the identified peaks in the eye diagram. Due to the complex structure of the measured eye diagrams, it was not possible to extract the contour line and determine the peak amplitudes and positions automatically. Therefore, the evaluation was done by looking at the measured eye diagram and manually pointing out the individual peaks. In order to make the measured data comparable, all derived values were

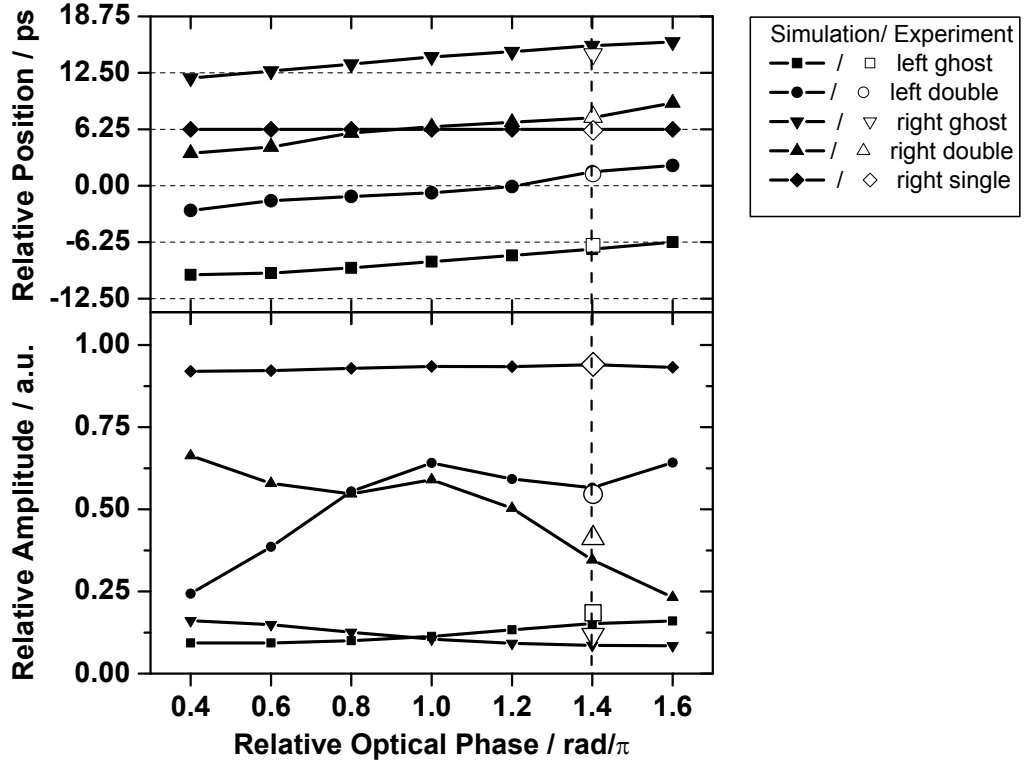


Figure 5.23: Relative amplitude and position versus the relative phase for  $P_{in} = 2.1 \text{ W}$  (solid: simulation; hollow: experiment).

normalized. The peak amplitudes were normalized to the peak amplitude of the "left single" peak. The peak positions were normalized to the position of the "left single" peak.

Fig. 5.22 shows the relative peak amplitudes as well as the relative temporal positions of all peaks of the measured eye diagrams as a function of the input peak power. It can be seen that the "ghost" peaks appeared for  $P_{in} > 1.2 \text{ W}$  and that their amplitudes increased with the input peak power. Simultaneously, the "double" peaks decreased, as energy was transferred from them to the "ghost" peaks. The "right single" peak stayed almost constant as it lost only little energy by IFWM with the adjacent zero bit (15 dB lower in power). An asymmetry was also found such that the "left" peaks were more intense than the "right" peaks. Regarding the temporal positions, only the "right single" peak was found on the 6.25 ps grid defined by the 160 Gbit/s data signal. The positions of the "double" peaks as well as the generated "ghost" peaks varied with increasing input powers and were not located on the 6.25 ps grid. Again, an asymmetric behavior was found such that the "right" peaks moved stronger than the "left" peaks.

It should be noted that the set of fiber parameters used in the numerical simulations was taken from the manufacturer's data and was not altered to fit the measured



eye diagrams. However, as the optical multiplexer inside the data transmitter was not phase stabilized, a relative optical phase difference between the adjacent optical pulses was introduced in the simulation (see Sec. A.2). It was thus interesting to investigate the influence of this relative optical phase on the resulting eye diagrams.

Fig. 5.23 shows simulation results for an input peak power of  $P_{in} = 2.1 \text{ W}$  versus relative optical phase  $\Delta\phi$  between the adjacent "left" and "right" pulses. It can be seen that depending on the relative phase, an amplitude asymmetry as well as a change in temporal position of the peaks appeared. In particular, the case of  $\Delta\phi = 1.0\pi$ , which corresponds to a carrier-suppressed RZ modulation format where the adjacent optical pulses have a relative phase shift of  $\pi$ , yielded an almost symmetric amplitude pattern. In that case the eye opening, which is given by the difference between the minimum of the single and double peaks and the maximum of the ghost peaks, was also maximized.

As shown in Fig. 5.23, the measurement at  $P_{in} = 2.1 \text{ W}$  (hollow symbols) was best reproduced using a relative phase of  $\Delta\phi = 1.4\pi$ . To reproduce the experimental data at other input powers, the relative phase had to be chosen appropriately for each measurement as explained in Sec. A.2. The reason for this was that the multiplexer inside the 160 Gbit/s transmitter was not phase stabilized and thus the relative optical phase was slowly drifting with time from measurement to measurement. This could also be noticed in the shift of the spectrum in Fig. 5.18.

It should be noted that the experimentally observed amplitude asymmetries in the eye diagrams were not due to the slight power asymmetry of the optical data pattern used. This was confirmed by simulations with a symmetric data pattern.

**Conclusion:** The high temporal resolution of the optical sampling system enabled for the first time the study of intra-channel four-wave mixing (IFWM) at 160 Gb/s. In a transmission system, IFWM will lead to an eye closure from both the mark and the space level as it generates "ghost pulses" in adjacent OTDM time slots (increase of the space level) and at the same time decreases the amplitude of adjacent "1-1" bits (decrease of the mark level). It was found that the relative optical phase between the adjacent OTDM-channels resulted in an asymmetric distortion of the eye diagram. A relative optical phase of  $\pi$  yielded the highest eye opening and thus the highest tolerance to IFWM.

### 5.3.3 Residual Dispersion

In a fiber optic transmission system, residual dispersion induces pulse broadening and, depending on the relation of pulse width and bit rate, pulse overlap which leads to interference noise at the receiver. The influence of chromatic dispersion has been experimentally investigated at a bit rate of 10 Gbit/s for an NRZ format data signal by optical sampling of asynchronous histograms only [97]. On the other hand, an optical sampling system has been successfully used to measure the effect of residual third order dispersion in a 160 Gbit/s fiber transmission [98]. This section describes for the first time the investigation of the eye diagram distortion at 160 Gbit/s due to residual chromatic dispersion in a fiber transmission link using an optical sampling system.



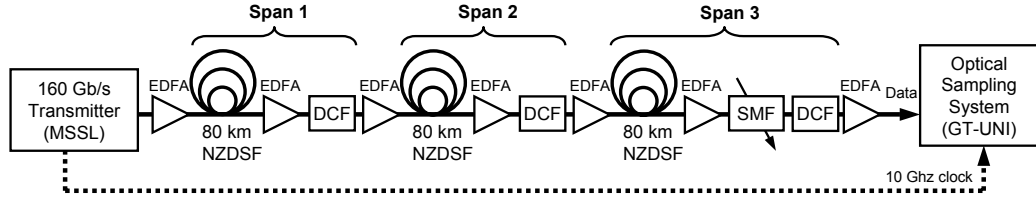


Figure 5.24: *Experimental set-up for the investigation of residual chromatic dispersion using the optical sampling system.*

**Set-up:** The experimental set-up is depicted in Fig. 5.24. It is similar to the set-up in the previous section. However, the transmission distance was increased and the total fiber link now consisted of three spans, each comprising 80 km NZDSF and DCF modules for coarse dispersion compensation. The amount of residual dispersion was varied by varying the length of the inserted SMF in front of the last DCF modules. The average input powers into the NZDSF and into each DCF module were +4.0 dBm and 0.0 dBm, respectively. This ensured that the influence of the fiber nonlinearity was negligible. The transmitter was set to "M00010" to generate a 2-channel 160 Gbit/s data signal. The GT-UNI based optical sampling system was used in this experiment, this time however with PMF1. The clock signal for the optical sampling system was tapped directly at the transmitter for reasons of simplicity. Due to the long length of the transmission link, the extraction of the clock before the fiber link caused a slow temporal drift of the measured eye diagrams with respect to the clock signal. However, since the acquisition time for one eye diagram was typically about 2 ms, the measurements were not hampered by this drift.

**Numerical simulation:** The measurements were accompanied by numerical simulations using the algorithm described in Sec. A.2. The parameters that were used to simulate the transmission link are summarized in Tab. 5.2. The values for the NZDSF and the DCF were taken from the manufacturer's data sheets and were specified with varying numerical precision as shown in the table. No tolerances were given for the data. The following standard values for were assumed for the SMF:  $\alpha = 0.2$  dB/km,  $D = 17$  ps/nm km,  $S = 0.06$  ps/nm<sup>2</sup> km and  $\gamma = 2$  /W km. The sum over the rows shows the total length of the transmission link (277.753 km) as well as the total loss (78.325 dB) and total accumulated dispersion (residual dispersion). The length of the SMF (1.123 m) was chosen such that the residual dispersion of the transmission link was almost zero. The residual dispersion slope became  $S_{res} = -0.063$  ps/nm<sup>2</sup> in this case.

When working with transmission links that exhibit residual chromatic dispersion, the initial chirp of the transmitter is an important parameter. In order to check whether the data signal at the input of the fiber link exhibited an initial chirp, the transmitter was first set to "U00000" and the autocorrelation trace and the optical spectrum of this 10 GHz pulse train were recorded at the input of the fiber link. The traces are shown in Fig. 5.25. From the spectrum a FWHM of  $\Delta\nu = 360$  GHz was

Table 5.2: Fiber parameters used in the numerical simulation of the chromatic dispersion investigation.

	$L$ / km	$\alpha \cdot L$ / dB	$D \cdot L$ / ps/nm	$S \cdot L$ / ps/nm <sup>2</sup>	$\gamma$ / (W km) <sup>-1</sup>
NZDSF 1	84.220	17.6	724	4.33	1.6
DCF 1	7.646	8.0	-734.87	-4.63	5.7
NZDSF 2	84.110	18.1	725	4.29	1.6
DCF 2	7.9	8.0	-729	-4.31	5.7
NZDSF 3	84.340	18.4	726	4.39	1.6
SMF	1.123	0.225	18.866	0.067	2
DCF 3	8.414	8.0	-730	-4.2	5.7
<b>Total</b>	<b>277.753</b>	<b>78.325</b>	<b>-0.004</b>	<b>-0.063</b>	

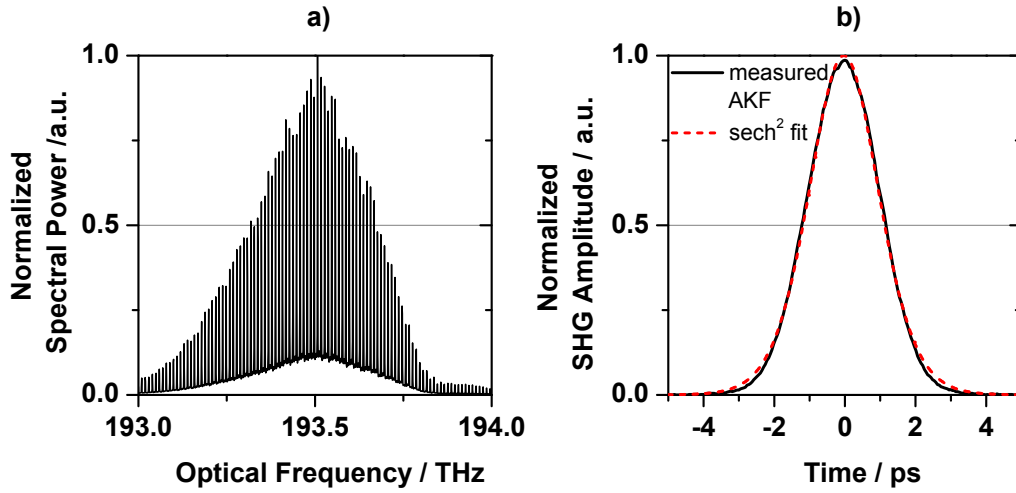


Figure 5.25: a) Optical spectrum and b) autocorrelation trace of 10 GHz pulse train from the transmitter at the input of the fiber link. The dashed line indicates the autocorrelation of a  $\text{sech}^2$  fit with 1.5 ps FWHM.

found while the autocorrelation trace yielded a FWHM of  $\tau = 1.5$  ps after deconvolution of assuming a  $\text{sech}^2$  pulse shape. The time bandwidth product thus became

$$\Delta\nu \cdot \tau = 0.54 = 1.7 \cdot \text{TL} \quad (5.1)$$

This was 1.7 times the transform limit (TL), which indicated that the data signal had an initial chirp. However, the measurement of the spectral width and the temporal width of the pulses does not yield the amount of chirp. Thus the chirp parameter was fit as described next.

The main parameter of interest in this experiment was the width  $\tau_{eye}$  (FWHM) of the eye diagrams. It was derived using the automated algorithm described in Sec. 2.4. In order to compare the measured and simulated FWHM values, it was first

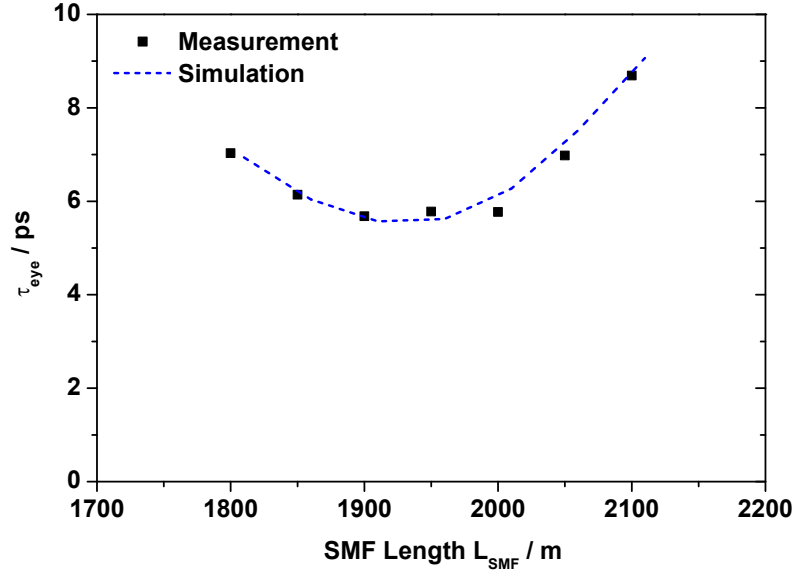


Figure 5.26: Full width at half maximum of the 1-channel eye diagrams as a function of the inserted SMF length. Experiment: solid squares; Simulation: dashed line. The following parameters were used in the simulation:  $\tau_{data} = 1.5$  ps,  $C = -0.37$ ,  $L_0 = 1950$  m,  $B = 60.8$  GHz.

necessary to fit the electrical detection bandwidth in the simulation (see Sec. A.2) to the actual temporal resolution of the optical sampling system. This was done by setting the transmitter to "M00000", i.e. by sending a 10 Gbit/s data signal over the transmission link. The result is shown in Fig. 5.26, where the FWHM of the measured eye diagrams is plotted versus the inserted SMF length. This measurement was now used to determine the electrical filter bandwidth as well as the chirp of the data signal by performing a numerical simulation of the eye diagrams and fitting the numerical to the measured results. Please note that in the experiments, minimum width of the eye diagrams was found at an SMF length around 1900-2000 m although from Tab. 5.2 it was expected around 1123 m. This deviation is attributed to tolerances in the given fiber data from the manufacturer. To compensate for this error, an offset in the SMF length was introduced, i.e. the length  $L_0$  at which the residual dispersion was zero was used as additional fit parameter in the simulation.

It can be seen from Fig. 5.26 that for a bandwidth of  $B = 60.8$  GHz of the optical sampling system and a chirp parameter of  $C = -0.37$  for the data signal and a zero dispersion length of  $L_0 = 1950$  m, the numerical simulation (dashed line) agreed very well with the measured data. Please note, that the minimum FWHM of the eye diagrams was limited by the temporal resolution (bandwidth) of the optical sampling system. The actual pulse width of the data signal as measured by an autocorrelator showed a minimum pulse width of 1.6 ps, which was almost equal to the input pulse width of  $\tau_{data} = 1.5$  ps.

The steepness of the FWHM curve was determined by the input pulse width of the data signal and the chirp parameter. In the simulation, the minimum FWHM

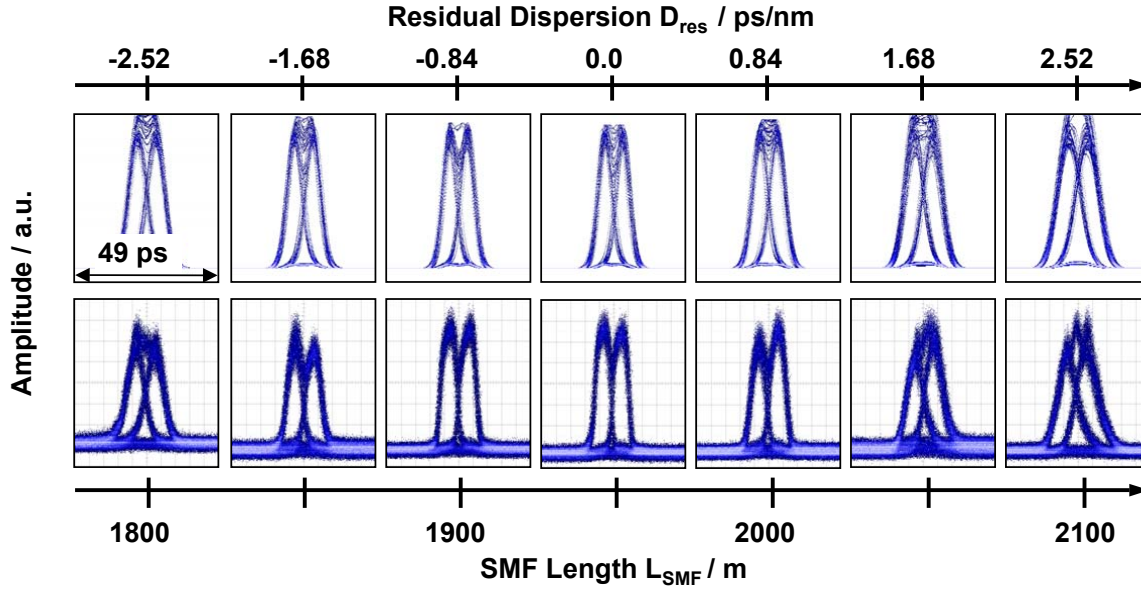


Figure 5.27: Measured (lower row) and simulated (upper row) eye diagrams of the 2-channel data signal as a function of the inserted SMF length. Each eye diagram depicts a time segment of 49 ps.

occurred around 1920 m and did not coincide with the zero dispersion length ( $L_0 = 1950$  m). This was a consequence of the initial chirp of the data signal that was best compensated by a residual negative dispersion.

**Results:** Having retrieved the filter and chirp parameters from the fit to 10 Gbit/s measurements, these values were used to perform numerical simulations for the 2-channel case. Fig. 5.27 compares the simulation results to the measured eye diagrams. Fairly good agreement between the experimental and the simulated data is achieved. However, a few distinct properties of the experimental eye diagrams were not reproduced in the simulation:

1. The measured eye diagrams showed an amplitude asymmetry between the left and right eye which was dependent on the sign of the residual dispersion. This asymmetry could only be reproduced in the simulation if different chirp parameters for the two adjacent OTDM-channels were used, which however could not be explained by the experimental conditions. Thus, the simulated eye diagrams were symmetric in amplitude.
2. The flanks of the experimental eyes were steeper than in the simulation. The reason for this was that the optical gating window was approximated by a Gaussian filter function. A more precise description of the actual shape of the gating window would most likely improve the agreement between experiment and simulation in this respect.

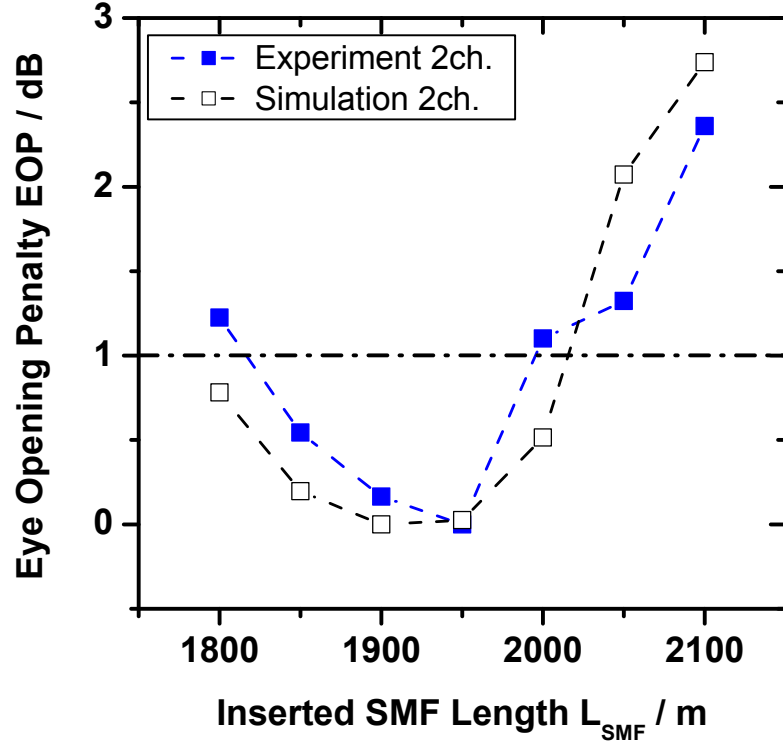


Figure 5.28: Eye opening penalty as a function of the inserted SMF length for the 2-channel test signal. Solid squares: Experimental data; open squares: Simulation results.

3. The smoother Gaussian flanks in the simulation cause a stronger overlap between the adjacent eyes and thus lead to stronger interference noise on the mark level in the simulation than observed in the experiment. However, it will be seen later, that this has only a minor effect on the eye opening penalty, which will be used as figure of merit for the signal distortion.

Please note that the statistical behavior of the interference pattern on the mark level is due to the timing jitter of the optical data signal. From the 10 Gbit/s measurements, a mean RMS timing jitter of 470 fs was derived. This value was then used in the simulation.

In order to estimate the system impairment due to the residual dispersion, the eye opening penalty (EOP) from the data shown in Fig. 5.27 was calculated. This was done by first deriving the eye opening (EO) for each measured eye diagram using the automatic evaluation algorithm described in Sec. 2.4. As each of the eye diagrams contained two eyes (called "left" and "right" eye), the eye opening was derived from each eye separately and then the average eye opening was calculated as

$$\overline{EO} = \frac{1}{2}(EO_{left} + EO_{right}) \quad (5.2)$$

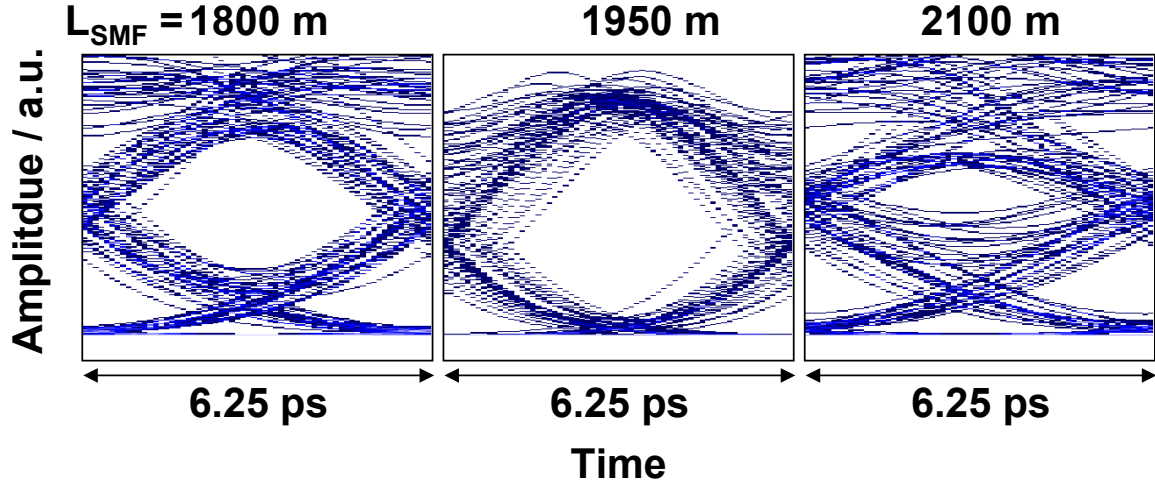


Figure 5.29: Simulated eye diagrams for three inserted SMF lengths. The optical data signal was a 160 Gbit/s PRBS signal. Each diagram shows a time segment of one bit period, i.e. 6.25 ps.

Then, the average eye opening of the two eyes was used to calculate the eye opening penalty as described by Eq. (2.55). The results are shown in Fig. 5.28. The curves show a parabolic shape with a minimum around  $L_{SMF} = 1920$  m. As expected, this minimum coincides with the minimum of the FWHM of the eyes as shown in Fig. 5.26 because the highest eye opening occurs when the eyes have the minimum width and thus the least temporal overlap. For positive and negative residual dispersion, the EOP increases because the broadening of the pulses closes the eyes by an increase of the space level due to the temporal overlapping of the adjacent channels.

It is common to take an eye opening penalty of 1 dB as figure of merit for the tolerance of the system to residual dispersion. Under this assumption, the experimental curve showed a dispersion tolerance (i.e. a 1 dB EOP width) of 180 m SMF length while the simulation yielded a slightly larger tolerance of 240 m SMF length. This corresponds to 3.0 ps/nm and 4.0 ps/nm of residual dispersion tolerance for the experimental and simulated data, respectively. The difference between the experimental and simulated tolerances was mainly due to the asymmetry of the flanks observed in the experimental eyes which were not reproduced by the simulation. The smoother experimental flanks led to a faster eye closure than in the simulations.

Although the numerical simulation did not fully reproduce the interference noise on the mark level for the 2-channel data signal, it still yielded good consistency with respect to the eye opening penalty. The reason is that the eye closure due to residual dispersion arises from the overlapping pulse tails. This overlap increases the maximum space level but leaves the minimum mark level almost uninfluenced. However, the 2-channel data signal differs from a full 16-channel OTDM signal in that each eye is only closed from one side and not from both sides. Therefore, in order to derive a system tolerance for a 160 Gbit/s OTDM system, a numerical simulation was performed using the same set of parameters as before, but using a full 16-channel 160 Gbit/s PRBS

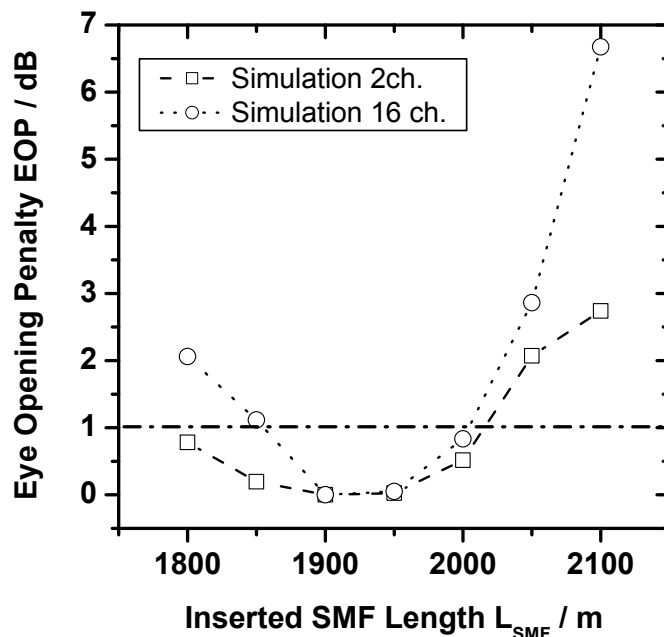


Figure 5.30: Eye opening penalty as a function of the inserted SMF length for the 2-channel and 16-channel test signal (Simulation).

sequence of 128 bits.

Three examples of resulting eye diagrams are shown in Fig. 5.29. When comparing these results with the simulated eye diagrams in Fig. 5.27, it can be seen that the PRBS-eyes exhibited a faster eye closure due to the overlap of broadened eyes from both sides. Also, the aforementioned asymmetry due to the chirp of the data signal is evident as the eye diagram at 2100 m was less open than the one at 1800 m.

Fig. 5.30 compares the eye opening penalty for the 2-channel and the 16-channel (PRBS) case. As expected, the 16-channel curve yielded a smaller dispersion tolerance due to a faster eye closure both for positive and negative residual dispersion. The 1 dB tolerance was 150 m SMF length which equals to 2.5 ps/nm.

**Conclusion:** Residual dispersion leads to a broadening of the eye diagram. Taking into account the initial chirp of the optical test signal used in the experiments, the broadening was reproduced quantitatively by numerical simulations in the 10 Gbit/s case. It was found, that the fiber link under investigation had zero residual dispersion if additional 1950 m of SMF were inserted. The chirp of the data signal induced an asymmetric broadening as function of the residual dispersion.

In the 2-channel experiment, the broadening of the eye diagrams led to interference noise on the mark level. The interference noise depended on the steepness of the flanks of the optical gating window of the sampling system as well as on the timing jitter of the optical data signal. However, the interference noise showed a minor influence on the eye opening penalty as the main contribution to the eye closure was due to a leakage of optical power into the "space" level by the tails of neighboring pulses.

Simulations of a 160 Gbit/s PRBS sequence showed a 1 dB EOP tolerance of 2.5 ps/nm. It should be noted however, that this tolerance depends on the actual bandwidth which the data signal is detected with. The optical eye monitor used in the experiments discussed in this section had an optical bandwidth of 61 GHz which was lower than the optimum bandwidth to detect a 160 Gbit/s data signal. Thus it can be expected that for an optimum detection bandwidth the dispersion tolerance is slightly larger.



## Chapter 6

# Summary and Conclusion

**Summary:** The objective of this work was to develop a measurement system which is capable of analyzing optical data signals with high temporal resolution. The particular target was the measurement of eye diagrams of optical data signals at data rates of 160 Gbit/s and above. The aim was to enable the analysis of distortions of such data signals in fiber optic transmission systems using optical eye diagrams.

To reach this goal, the optical sampling technique was employed. The optical sampling system was based on five building blocks, namely the clock recovery, clock processing, sampling pulse source, sampling gate and opto/electrical detector. By sampling the data signal under investigation in the optical domain using an all-optical sampling gate, the bandwidth of the system exceeded 250 GHz and allowed the measurement of waveforms and eye diagrams of optical data signals up to a data rate of 320 Gbit/s.

Different sampling gates were studied in this work, because these gates determine the temporal resolution of the optical sampling system. The nonlinear optical loop mirror (NOLM) was an interferometric gate based on the nonlinearity of a fiber while the gain-transparent ultrafast nonlinear interferometer (GT-UNI) was based on a semiconductor optical amplifier (SOA). In addition, a third sampling gate based on the Kerr effect in a fiber was also used.

The NOLM based optical sampling system had the highest temporal resolution of 1.5 ps corresponding to an optical bandwidth of 294 GHz. The GT-UNI based system reached a slightly lower optical bandwidth of 257 GHz. The optical bandwidth of the system with the Kerr gate was 210 GHz. This value was limited by the pulse width of the sampling pulses used. It can be expected that an optical bandwidth similar to the bandwidth of the NOLM gate is achieved if sampling pulses with the same short pulse width are used.

Both, the NOLM and the GT-UNI sampling gate were operated over a wavelength range of about 20 nm. The wavelength range of the Kerr sampling gate was not explicitly investigated but it can be assumed that it is similar to the NOLM gate because the same nonlinear medium and nonlinear effect were used.

The timing jitter of the sampling system is determined by the timing jitter of the clock recovery and of the sampling pulse source which controls the sampling gate. The optical clock recovery was realized in a very stable way using a phase-locked loop (PLL) configuration. The PLL incorporated an all-optical gate which acted as

ultrafast optical phase comparator between the optical data signal and an optical local oscillator operated at 10 GHz. The sampling pulse source was a hybrid mode-locked semiconductor laser with an external cavity. Depending on the type of sampling gate, two different pulse sources were used, which emitted either at a wavelength of 1310 nm or 1550 nm.

Due to the low timing jitter of the pulse sources, the sampling system allowed to measure eye diagrams at a data rate of 160 Gbit/s using both the NOLM and the GT-UNI sampling gate. The timing jitter of the sampling pulse source #1 used to control the GT-UNI gate was even low enough to measure the eye diagram of a 320 Gbit/s data signal. This was the first measurement of an eye diagram at such a high bit rate using a semiconductor based sampling system. In the case of the random sampling system set-up, the timing jitter of the optical sampling system is determined by the timing jitter of the clock recovery and the oscilloscope timebase. The timing jitter of the oscilloscope timebase was 200 fs so that it can be expected that the measurement of a 320 Gbit/s eye diagram will be possible with this system as well.

The optical sampling system was applied to analyze qualitatively and quantitatively the signal distortions that a 160 Gbit/s optical data signal suffers upon passage through fiber transmission links. The investigation of the signal distortion by signal-to-noise ratio (SNR) reduction was performed using derived Q-factors from the measured eye diagrams with the NOLM based sampling system and comparing them with measured bit-error rates. A good correlation was found for Q-values below 5.0. For higher Q-values, the Q-factor of the measured eye diagrams saturated due to the SNR degradation of the data signal by the sampling system itself.

As an example of degradations due to fiber nonlinearities the effect of intra-channel four-wave mixing (IFWM) was investigated at 160 Gbit/s using the GT-UNI based sampling system. For the first time, the system allowed to verify experimentally the generation of ghost pulses at a data rate of 160 Gbit/s. The analysis of the dynamics of the generated ghost pulses was supported by numerical simulations. For the simulations, a split step Fourier algorithm was implemented to solve the nonlinear propagation equation for optical pulses in fibers. The simulations showed good agreement with the measured data and indicated in particular that the amplitude and temporal position of the generated ghost pulses are strongly dependent on the relative optical phase between adjacent pulses in the data signal.

The effect of residual chromatic dispersion in a 160 Gbit/s transmission system was investigated using the GT-UNI based sampling system. These measurements were also accompanied by numerical simulations. It was shown that the dispersion induced broadening of the eye diagrams led to interference noise on the mark level. The interference noise depended on the steepness of the flanks of the optical gating window of the sampling system as well as on the timing jitter of the optical data signal. However, the interference noise showed a minor influence on the eye opening penalty as the main contribution to the eye closure was due to an increase of the space level by the tails of neighboring eyes.

The random sampling system was used to investigate the jitter performance of two different optical transmitters. Due to the low timing jitter of the random sampling system, it was possible to visualize the different performance of two transmitters, which showed 460 fs and 230 fs of timing jitter, respectively.

**Conclusion:** The optical sampling system developed in this work extends the detection bandwidth of conventional photodetectors and oscilloscopes up to a factor of five. Several configurations of the optical sampling system were realized. In particular, different optical sampling gates were investigated since the gating windows of these gates determine the optical bandwidth of the sampling system. The fiber based gate (nonlinear optical loop mirror, NOLM) showed the shortest gating window (1.5 ps) and thus yielded the highest optical bandwidth (294 GHz). However, its wavelength range was limited by the dispersion slope of the highly nonlinear fiber (HNLF) which caused walk-off in the gate. The SOA based gate (gain-transparent ultrafast nonlinear interferometer, GT-UNI) showed a very high linearity (50 dB) and a large wavelength range (20 nm). However, the usable gating window width was limited to 1.8 ps by the differential operation scheme. It also exhibited a fairly high insertion loss which degraded the signal-to-noise ratio of the data signal under investigation. Thus the preference for one or the other sampling gate depends on the application. If the data signal wavelength is fixed, then the fiber based gate will perform best. If a comparison between different wavelengths or a large dynamic range is needed, the gain-transparent SOA based gate should be chosen.

The realized optical sampling system was successfully applied to measure eye diagrams and waveforms of optical data signals at a bit rate of 160 Gbit/s and 320 Gbit/s. Before, this was impossible due to the limited bandwidth of conventional electrical sampling systems. In contrast to most other work in this field, the optical sampling system in this work included an optical clock recovery. This allowed for the application of the system in fiber transmission experiments. In particular, the degradation of 160 Gbit/s optical data signals due to amplifier noise, fiber nonlinearity and chromatic dispersion was investigated qualitatively and quantitatively. For the first time, this was done using eye diagrams that were sampled in the optical domain.

Regarding the optimum set-up of the sampling system, the experiments with the random sampling system were very encouraging. The measured eye diagrams showed negligible noise on the baseline. This is attributed to the fact that the sampling pulse source in this set-up was directly operated at a Megahertz repetition rate. In the conventional set-up, the imperfect pulse suppression of the unwanted sampling pulses broadens the baseline because the amplitude of each individual optical sample is superimposed by signal which is unintentionally gated by the suppressed sampling pulses. As compared to the conventional sampling set-up, the random sampling system also required less components and was thus easier to handle. However, it required the use of a special oscilloscope firmware to measure the sampling times of the optical samples from the arrival times of the sampling pulses. The random sampling set-up is preferable if the jitter of the oscilloscope timebase (200 fs) is tolerable in the particular application. It can easily be combined with the optical clock recovery developed in this work to form a complete optical sampling system. The random sampling system was operated in combination with the Kerr gate. By compression of the sampling pulses it can be expected that the same good performance as with the NOLM sampling gate can be achieved with this gate. In that case, the Kerr gate will be preferable because experiments showed that the contrast of the gating window is larger for the Kerr gate than for the NOLM gate.



# Bibliography

- [1] G. P. Agrawal, *Fiber-Optic Communication Systems*, 3rd ed., ser. Wiley Series in Microwave and Optical Engineering, K. Chang, Ed. New York: John Wiley and Sons, Inc., 2002.
- [2] *Datasheet of C5680 Streak Camera*, Hamamatsu Photonics K.K., 2003.
- [3] *Datasheet of Pulse Check Autocorrelator*, APE GmbH, 2003.
- [4] *Datasheet of 86116B 65 GHz Optical / 80 GHz Electrical Plug-In Module*, Agilent Technologies, Inc., 2002.
- [5] *Datasheet of 80E06 70+ GHz Sampling Head*, Tektronix, Inc., 2003.
- [6] *Datasheet of XPDV2020R Photodetector*, U2T Photonics AG, 2003.
- [7] *ITU-T G.671 Transmission Characteristics of Optical Components and Subsystems*, International Telecommunication Union (ITU), 2002.
- [8] T. Yamamoto, E. Yoshida, K. R. Tamura, K. Yonenaga, and M. Nakazawa, "640-Gbit/s optical TDM transmission over 92 km through a dispersion-managed fiber consisting of single-mode fiber and "reverse dispersion fiber"', *IEEE Photon. Technol. Lett.*, vol. 12, no. 3, pp. 353–355, 2000.
- [9] M. Nakazawa, T. Yamamoto, and K. Tamura, "1.28 Tbit/s-70 km OTDM transmission using third- and fourth-order simultaneous dispersion compensation with a phase modulator," *Electron. Lett.*, vol. 36, no. 24, pp. 2027–2029, 23 Nov 2000.
- [10] U. Feiste, R. Ludwig, C. Schubert, J. Berger, C. Schmidt, H. G. Weber, A. Munk, B. Schmauss, B. Buchhold, D. Briggmann, F. Kueppers, and F. Rumpf, "160 Gbit/s transmission over 116 km field-installed fiber using 160 Gbit/s OTDM and 40 Gbit/s ETDM," *Electron. Lett.*, vol. 37, no. 7, pp. 443–445, March 2001.
- [11] H. Weber, R. Ludwig, C. Schmidt, C. Schubert, J. Berger, E. Hilliger, M. Kroh, V. Marembert, C. Boerner, S. Ferber, and H. Ehrke, "160 Gbit/s TDM-transmission technology," in *Proc. 28th Eur. Conf. on Opt. Comm. (ECOC'02)*, 2002, invited paper 2.1.1.
- [12] H. Weber and R. Ludwig, "Ultrafast OTDM transmission technology with advanced optical devices," in *Proc. Of the 9th International Workshop on Femtosecond Technology (FST 2002)*. Tsukuba, Japan: The Femtosecond Technology Research Association (FESTA), 2002, plenary talk 1.

- [13] C. Schmidt, F. Futami, S. Watanabe, T. Yamamoto, C. Schubert, J. Berger, M. Kroh, H.-J. Ehrke, E. Dietrich, C. Börner, R. Ludwig, and H. G. Weber, "Complete optical sampling system with broad gap-free spectral range for 160 Gbit/s and 320 Gbit/s and its application in a transmission system," in *Opt. Fiber Commun. Conf. Techn. Dig.*, Anaheim, USA, March 2002, pp. 528–530, paper ThU1.
- [14] R.L.Jungerman, G. Lee, O. Baccafusca, Y. Yaneko, N. Itagaki, R. Shioda, A. Harada, Y. Nihei, and G. Sucha, "1-THz bandwidth C- and L-Band optical sampling with a bit rate agile timebase," *IEEE Photon. Technol. Lett.*, vol. 14, no. 8, pp. 1148–1150, August 2002.
- [15] M. Westlund, H. Sunnerud, M. Karlsson, and P. Andrekson, "Software-synchronized all-optical sampling," in *OSA Trends in Optics and Photonics (TOPS) Vol. 86, Optical Fiber Commun. Conf., Technical Digest, Postconference Edition*, Atlanta, Georgia (USA), March 23–28 2003, pp. 409–410, paper WP6.
- [16] —, "160 Gb/s optical data pattern monitoring using a software-synchronized all-optical sampling system," in *Proc. 29th Eur. Conf. on Opt. Comm. (ECOC'03)*, Rimini (Italy), September 21–25 2003, pp. 48–49, paper Mo3.6.2.
- [17] N. Yamada, S. Nogiwa, and H. Ohta, "Measuring eye diagram of 640 Gb/s OTDM signal with optical sampling system by using wavelength-tunable soliton pulse," in *Proc. 29th Eur. Conf. on Opt. Comm. (ECOC'03)*, Rimini (Italy), September 21–25 2003, paper Mo4.6.5.
- [18] T. Miyazaki, H. Sotobayashi, and W. Chujo, "Optical sampling and demultiplexing of 80 Gb/s OTDM signals with optically recovered clock by injection mode-locked laser diode," in *Proc. 28th Eur. Conf. on Opt. Comm. (ECOC'02)*, Copenhagen, Denmark, 2002, paper 2.1.6.
- [19] M. Shirane, Y. Hashimoto, H. Kurita, H. Yamada, and H. Yokoyama, "Optical sampling measurement with all-optical clock recovery using mode-locked diode lasers," in *OSA Trends in Optics and Photonics (TOPS) Vol. 54, Optical Fiber Commun. Conf., Technical Digest, Postconference Edition*. Washington DC: Optical Society of America, 2001, p. MG2.
- [20] T. Miyazaki and F. Kubota, "Simultaneous demultiplexing and clock recovery for 160 Gb/s OTDM signal using a symmetric Mach-Zehnder switch in electrooptic feedback loop," *IEEE Photon. Technol. Lett.*, vol. 15, no. 7, pp. 1008–1010, July 2003.
- [21] I. Kang and M. Yan, "Simple setup for simultaneous optical clock recovery and ultra-short sampling pulse generation," *Electron. Lett.*, vol. 38, no. 20, pp. 1199–1200, 26th September 2002.
- [22] I. Kang and C. Dorrer, "Optical sampling source-free simultaneous eye-diagram monitoring and clock recovery up to 160 Gb/s," in *Proc. 29th Eur. Conf. on Opt.*

- Comm. (ECOC'03)*, Rimini (Italy), 21-25 September 2003, pp. 292–293, paper Tu4.2.4.
- [23] H. Ohta, S. Nogiwa, N. Oda, and H. Chiba, “Highly sensitive optical sampling system using timing-jitter-reduced gain-switched optical pulse,” *Electron. Lett.*, vol. 33, no. 25, pp. 2142–2144, December 1997.
- [24] H. Ohta, S. Nogiwa, and H. Chiba, “Highly sensitive optical sampling system with 100 GHz bandwidth,” in *Proc. 24th Europ. Conf. Opt. Commun.*, Madrid (Spain), September 20-24 1998, pp. 503–504.
- [25] S. Nogiwa, H. Ohta, K. Kawaguchi, and Y. Endo, “Improvement of sensitivity in optical sampling system,” *Electron. Lett.*, vol. 35, no. 11, pp. 917–918, 27th May 1999.
- [26] H. Ohta, S. Nogiwa, Y. Kawaguchi, and Y. Endo, “Measurement of 200 Gbit/s optical eye diagram by optical sampling with gain-switched optical pulse,” *Electron. Lett.*, vol. 36, no. 8, pp. 737–739, 13th April 2000.
- [27] S. Nogiwa, Y. Kawaguchi, H. Ohta, and Y. Endo, “Highly sensitive and time-resolving optical sampling system using thin PPLN crystal,” *Electron. Lett.*, vol. 36, no. 20, pp. 1727–1728, 28th September 2000.
- [28] A. Otani, T. Otsubo, and H. Watanabe, “A turn-key-ready optical sampling oscilloscope by using electro-absorption modulators,” in *Proc. 25th Europ. Conf. Opt. Commun.*, 1999, pp. 374–375, paper P3.2.
- [29] H. Takara, S. Kawanishi, and M. Saruwatari, “Optical signal eye diagram measurement with subpicosecond resolution using optical sampling,” *Electron. Lett.*, vol. 32, no. 15, pp. 1399–1400, 18 July 1996.
- [30] H. Takara, S. Kawanishi, A. Yokoo, S. Tomaru, T. Kitoh, and M. Saruwatari, “100 Gbit/s optical signal eye-diagram measurement with optical sampling using organic nonlinear optical crystal,” *Electron. Lett.*, vol. 32, no. 24, pp. 2256–2258, 21 November 1996.
- [31] J. Li, J. Hansryd, P. Hedekvist, P. Andrekson, and S. Knudsen, “300-Gb/s eye-diagram measurement by optical sampling using fiber-based parametric amplification,” *IEEE Photon. Technol. Lett.*, vol. 13, no. 9, pp. 987–989, September 2001.
- [32] J. Li, M. Westlund, H. Sunnerud, B.-E. Olsson, M. Karlsson, and P. Andrekson, “0.5 Tbit/s eye-diagram measurement by optical sampling using XPM-induced wavelength shifting in highly nonlinear fiber,” in *Proc. 29th Eur. Conf. on Opt. Comm. (ECOC'03)*, Rimini (Italy), September 21-25 2003, pp. 136–137, paper Mo4.6.4.
- [33] H. Ohta, N. Banjo, N. Yamada, S. Nogiwa, and Y. Yanagisawa, “Measuring eye diagram of 320 Gbit/s optical signal by optical sampling using passively

- modelocked fibre laser,” *Electron. Lett.*, vol. 37, no. 25, pp. 1541–1542, December 2001.
- [34] S. Nogiwa, N. Yamada, and H. Ohta, “Broad wavelength-bandwidth optical sampling system using wavelength-tunable soliton pulses,” in *OSA Trends in Optics and Photonics (TOPS) Vol. 55, Optical Fiber Commun. Conf., Technical Digest, Postconference Edition*, Anaheim, CA (USA), March 17-22 2002, pp. 533–534.
  - [35] N. Yamada, H. Ohta, and S. Nogiwa, “Jitter-free optical sampling system using passively modelocked fibre laser,” *Electron. Lett.*, vol. 38, no. 18, pp. 1044–1045, 29th August 2002.
  - [36] C. Schubert, C. Schmidt, C. Börner, E. Dietrich, S. Ferber, R. Ludwig, and H. Weber, “A gain-transparent ultrafast-nonlinear interferometer (gt-uni) in a 160 gb/s optical sampling system,” in *Techn. Dig. of Optical Amplifiers and their Applications, OAA*, 2002, paper OTuD5.
  - [37] C. Schmidt, C. Schubert, S. Watanabe, F. Futami, R. Ludwig, and H. Weber, “320 gb/s all-optical eye diagram sampling using gain-transparent ultrafast nonlinear interferometer (gt-uni),” in *Proc. 28th Eur. Conf. on Opt. Comm. (ECOC’02)*, Copenhagen, Denmark, 2002, paper 2.1.3.
  - [38] C. Schmidt, C. Schubert, C. Börner, C. Weinert, H. Bülow, E. Lach, and H. Weber, “Investigation of intra-channel four-wave mixing at 160 Gb/s using an optical sampling system,” in *Proc. 29th Eur. Conf. on Opt. Comm. (ECOC’03)*, Rimini, Italy, September 21-25 2003, pp. 990–991, paper Th2.5.2.
  - [39] M. Shirane, Y. Hashimoto, H. Yamada, and H. Yokoyama, “A compact optical sampling measurement system using mode-locked laser-diode modules,” *IEEE Photon. Technol. Lett.*, vol. 12, no. 11, pp. 1537–1539, November 2000.
  - [40] C. Dorrer, D. Kilper, H. Stuart, and G. Raybon, “Ultra-sensitive optical sampling by coherent-linear detection,” in *OSA Trends in Optics and Photonics (TOPS) Vol. 55, Optical Fiber Commun. Conf., Technical Digest, Postconference Edition*, Anaheim, CA (USA), March 17-22 2002, pp. FD5–1 – FD5–3, postdeadline paper FD5.
  - [41] I. Kang and K. Dreyer, “Sensitive 320 Gb/s eye diagram measurements via optical sampling with semiconductor optical amplifier-ultrafast nonlinear interferometer,” *Electron. Lett.*, vol. 39, no. 14, pp. 1081–1082, 10th July 2003.
  - [42] I. Shake, R. Kasahara, H. Takara, M. Ishii, Y. Inoue, T. Ohara, Y. Hibino, and S. Kawanishi, “WDM signal monitoring utilizing asynchronous sampling and wavelength selection based on thermo-optic switch and AWG,” in *Proc. 29th Eur. Conf. on Opt. Comm. (ECOC’03)*, Rimini (Italy), September 21-25 2003, pp. 780–781, paper We4.P112.
  - [43] I. Shake, H. Takara, and S. Kawanishi, “Simple Q factor monitoring for BER estimation using openend eye diagrams captured by high-speed asynchronous



- electrooptical sampling,” *IEEE Photon. Technol. Lett.*, vol. 15, no. 4, pp. 620–622, April 2003.
- [44] I. Shake and H. Takara, “Chromatic dispersion dependence of asynchronous amplitude histogram evaluation of NRZ signal,” *J. Lightwave Technol.*, vol. 21, no. 10, pp. 2154–2161, October 2003.
- [45] S. Diez, “All-optical signal processing by gain-transparent semiconductor switches,” Ph.D. dissertation, Technical University Berlin, 2000.
- [46] K. J. Blow, N. J. Doran, and B. P. Nelson, “Demonstration of the nonlinear fiber loop mirror as ultrafast all-optical demultiplexer,” *Electron. Lett.*, vol. 26, no. 14, pp. 962–964, 5 July 1990.
- [47] M. Jinno, “Nonlinear sagnac interferometer switch and its applications,” *IEEE J. Quantum Electron.*, vol. 28, pp. 875–882, 1992.
- [48] S. Bigo, O. Leclerc, and E. Desurvire, “All-optical fiber signal processing and regeneration for soliton communications,” *IEEE J. Quantum Electron.*, vol. 3, pp. 1208–1223, 1997.
- [49] N. S. Patel, K. A. Rauschenbach, and K. L. Hall, “40 Gb/s demultiplexing using an ultrafast nonlinear interferometer (UNI),” *IEEE Photon. Technol. Lett.*, vol. 8, no. 12, pp. 1695–1697, December 1996.
- [50] H. Packard, *Fiber Optics Handbook*, 3rd ed., C. Hentschel, Ed. Boeblingen, Germany: Hewlett Packard GmbH, 1989.
- [51] C. Schubert, L. Schares, C. Schmidt, G. Guekos, and H. Weber, “Phase dynamics in gain-transparent semiconductor optical amplifiers,” in *Proc. 29th Eur. Conf. on Opt. Comm. (ECOC’03)*, Rimini, Italy, September 21–25 2003, pp. 1062–1063, paper Th3.5.2.
- [52] L. Schares, C. Schubert, C. Schmidt, H. Weber, L. Occhi, and G. Guekos, “Phase dynamics of semiconductor optical amplifiers at 10 to 40 ghz,” *IEEE J. Quantum Electron.*, vol. 39, no. 11, pp. 1394–1408, November 2003.
- [53] C. Schubert, S. Diez, J. Berger, R. Ludwig, U. Feiste, H. G. Weber, G. Toptchiyski, K. Petermann, and V. Krajinovic, “160 Gb/s all-optical demultiplexing using a gain-transparent Ultrafast-Nonlinear Interferometer (GT-UNI),” *IEEE Photon. Technol. Lett.*, vol. 13, no. 5, pp. 475–477, May 2001.
- [54] C. Schubert, “Interferometric gates for all-optical signal processing,” Ph.D. dissertation, Fakultät II (Mathematik und Naturwissenschaften), Technical University Berlin, 2004.
- [55] R. Ludwig, S. Diez, and H. G. Weber, “A novel all-optical switch for demultiplexing in otdm-systems demonstrated in a 640 Gbit/s WDM/TDM experiment,” in *OFC’98*, San Jose, USA, 1998, p. paper PD22.

- [56] S. Diez, R. Ludwig, and H. G. Weber, "All-optical switch for TDM and WDM/TDM systems demonstrated in a 640 Gbit/s demultiplexing experiment," *Electron. Lett.*, vol. 34, pp. 803–804, 1998.
- [57] T. Okuno, M. Onishi, T. Kashiwada, S. Ishikawa, and M. Nishimura, "Silica-based functional fibers with enhanced nonlinearity and their applications," *IEEE J. Quantum Electron.*, vol. 5, no. 5, pp. 1385–1391, September/October 1999.
- [58] S. Watanabe and F. Futami, "All-optical signal processing using highly nonlinear optical fibers," *IEICE Trans. Commun.*, vol. E84-B, no. 5, pp. 1179–1189, May 2001.
- [59] G. P. Agrawal, *Nonlinear Fiber Optics*, 3rd ed. London, UK: Academic Press, 2001.
- [60] F. Futami, Y. Takushima, and K. Kikuchi, "Generation of wideband and flat supercontinuum over a 280-nm spectral range from a dispersion-flattened optical fiber with normal group-velocity dispersion," *IEICE Trans. Commun.*, vol. E82-B, no. 8, pp. 1265–1272, August 1999.
- [61] R. Ludwig, S. Diez, A. Ehrhardt, L. Küller, W. Pieper, and H. G. Weber, "A tunable femtosecond modelocked semiconductor laser for applications in OTDM systems," *IEICE Trans. Electron.*, vol. E81-C, no. 2, pp. 140–145, 1998, (J52).
- [62] R. Ludwig and A. Ehrhardt, "Turn-key-ready wavelength-, repetition rate- and pulsewidth- tunable femtosecond hybrid modelocked semiconductor laser," *Electron. Lett.*, vol. 31, pp. 1165–1167, 1995.
- [63] E. L. Portnoy and A. V. Chelnokov, "Characteristics of heterostructure lasers with a saturable absorber fabricated by deep ion implantation," *Sov. Tech. Phys. Lett.*, vol. 15, pp. 432–433, 1989.
- [64] L. Jiang, M. Grein, E. Ippen, C. McNeilage, J. Searls, and H. Yokoyama, "Quantum-limited noise performance of a mode-locked laser diode," *Optics Lett.*, vol. 27, no. 1, pp. 49–51, January 1 2002.
- [65] F. Futami, Y. Takushima, and K. Kikuchi, "Generation of 10 GHz, 200 fs fourier-transform-limited optical pulse train from modelocked semiconductor laser at 1.55  $\mu\text{m}$  by pulse compression using dispersion-flattened fibre with normal group-velocity dispersion," *Electron. Lett.*, vol. 34, no. 22, pp. 2129–2130, 29th October 1998.
- [66] Y. Takushima and K. Kikuchi, "10-GHz, over 20-channel multiwavelength pulse source by slicing super-continuum spectrum generated in normal-dispersion fiber," *IEEE Photon. Technol. Lett.*, vol. 11, no. 3, pp. 322–324, March 1999.
- [67] *Datasheet of 86107A Precision Timebase Reference Module*, Agilent Technologies, Inc., 2003.

- [68] D. V. der Linde, "Characterization of the noise in continuously operating mode-locked lasers," *Appl. Phys. B*, vol. 39, pp. 201–217, 1986.
- [69] M. Kroh, L. Küller, R. Ludwig, C. Schmidt, and H. Weber, "Investigations on phase noise in a semiconductor mode-locked laser," in *OSA Trends in Optics and Photonics (TOPS) Vol. 86, Optical Fiber Commun. Conf., Technical Digest, Postconference Edition*. Washington, DC: Optical Society of America, March 23–28 2003, pp. 673–674.
- [70] D. Scherer, "Entwicklungsprinzipien und Prüfmethode für HF- und Mikrowellengeneratoren mit niedrigem Phasenrauschen," *Nachrichten Elektronik*, vol. 35, no. 8, p. 283ff, 1981.
- [71] T. Yamamoto, U. Feiste, J. Berger, C. Schubert, C. Schmidt, R. Ludwig, and H. G. Weber, "160 Gbit/s demultiplexer with clock recovery using SOA-based interferometric switches and its application to 120 km fiber transmission," in *Proc. 27th Eur. Conf. on Opt. Comm. (ECOC'01)*, Amsterdam, The Netherlands, Sep. 30 - Oct. 4 2001, pp. 192–193.
- [72] O. Kamatani and S. Kawanishi, "Ultrahigh-speed clock recovery with phase lock loop based on four-wave mixing in a traveling-wave laser diode amplifier," *J. Lightwave Technol.*, vol. 14, no. 8, pp. 1757–1767, 1996.
- [73] D. Tong, B. Mikkelsen, G. Raybon, T. Nielsen, K. Dreyer, and J. Johnson, "Optoelectronic phase-locked loop with balanced photodetection for clock-recovery in high-speed optical time-division-multiplexed systems," *IEEE Photon. Technol. Lett.*, vol. 12, pp. 1064–1066, 2000.
- [74] C. Boerner, C. Schubert, C. Schmidt, E. Hilliger, V. Marembert, J. Berger, S. Ferber, E. Dietrich, R. Ludwig, B. Schmauss, and H. Weber, "160 Gbit/s clock recovery with electro-optical PLL using a bidirectionally operated electroabsorption modulator as phase comparator," *Electron. Lett.*, vol. 39, no. 14, pp. 1071–1073, 10th July 2003.
- [75] T. Yamamoto, L. Oxenløwe, C. Schmidt, C. Schubert, E. Hilliger, U. Feiste, J. Berger, R. Ludwig, and H. Weber, "Clock recovery from 160 Gbit/s data signals using phase-locked loop with interferometric optical switch based on semiconductor optical amplifier," *Electron. Lett.*, vol. 37, no. 8, pp. 509–510, April 2001.
- [76] L. Oxenlowe, C. Schubert, C. Schmidt, E. Hilliger, J. Berger, U. Feiste, R. Ludwig, and H. G. Weber, "Optical clock recovery employing an optical PLL using cross-phase modulation in a sagnac-interferometer," in *Conf. on Lasers and Electro-Optics (CLEO) Tech. Dig.*, Baltimore, USA, May 6–11 2001, paper CThU2.
- [77] M. Eiselt, W. Pieper, and H. G. Weber, "All-optical demultiplexing with a semiconductor laser amplifier in a loop mirror," *Electron. Lett.*, vol. 29, pp. 1167–1169, 1993.

- [78] Z. Xiang, P. Ye, K. Guan, and J. Lin, "Theory of ultrahigh-speed clock extraction with phase locked loop based on a terahertz optical asymmetric demultiplexer," *Opt. Commun.*, vol. 159, pp. 53–57, 1999.
- [79] T. Yamamoto, C. Schubert, C. Schmidt, L. Oxenløwe, U. Feiste, and H. Weber, "A semiconductor laser amplifier in a loop mirror as a phase comparator in PLL-based clock recovery for 160 Gb/s data signals," in *Techn. Dig. of Optical Amplifiers and their Applications, OAA*, 2001, paper OTuC2.
- [80] E. Hölzer and D. Thierbach, *Nachrichtenübertragung*. Berlin: Springer, 1966.
- [81] K. Miya, *Satellite Communications Technology*. Tokyo: KDD Engineering and Consulting, 1981.
- [82] S. Diez, R. Ludwig, and H. G. Weber, "Gain-transparent SOA-switch for high-bitrate OTDM Add/Drop multiplexing," *IEEE Photon. Technol. Lett.*, vol. 11, no. 1, pp. 60–62, Jan. 1999.
- [83] S. Diez, U. Feiste, R. Ludwig, and H. G. Weber, "Characterization of an all-optical gain-transparent SLALOM switch," in *Optical Amplifiers and their Applications, OAA '98, Technical Digest*, Vail, USA, July 1998, pp. 151–154, paper TuD9.
- [84] M. N. Islam, *Ultrafast All-Optical Switching Devices*, ser. Photonic Switching and Interconnects, A. Marrakchi, Ed. New York: Marcel Dekker, 1994.
- [85] C. Schubert, R. Ludwig, S. Watanabe, F. Futami, C. Schmidt, J. Berger, C. Boerner, S. Ferber, and H. Weber, "160 Gbit/s wavelength converter with 3R-regenerating capability," *Electron. Lett.*, vol. 38, no. 16, pp. 903–904, 1st August 2002.
- [86] M. Westlund, H. Sunnerud, M. Karlsson, J. Hansryd, J. Li, P. Hedekvist, and P. Andrekson, "All-optical synchronous Q-measurements for ultra-high speed transmission systems," in *OSA Trends in Optics and Photonics (TOPS) Vol. 55, Optical Fiber Commun. Conf., Technical Digest, Postconference Edition*, Anaheim, CA (USA), March 17-22 2002, pp. 530–531, paper ThU2.
- [87] I. Shake, H. Takara, S. Kawanishi, and Y. Yamabayashi, "Optical signal quality monitoring method based on optical sampling," *Electron. Lett.*, vol. 34, no. 22, pp. 2152–2154, 28th October 1998.
- [88] I. Shake, E. Otani, H. Takara, K. Uchiyama, Y. Yamabayashi, and T. Morioka, "Bit rate flexible quality monitoring of 10 to 160 Gb/s optical signals based on optical sampling technique," *Electron. Lett.*, vol. 36, no. 25, pp. 2087–2088, 7th December 2000.
- [89] I. Shake, H. Takara, and T. Morioka, "Determination of the origin of BER degradation utilizing asynchronous amplitude histograms," in *Proc. 4th Pacific Rim Conference on Lasers and Electro-Optics (CLEO/Pacific Rim 2001)*, 15-19 July 2001, pp. II560–II561, paper ThB2-2.

- [90] I. Shake and H. Takara, "Averaged Q-factor method using amplitude histogram evaluation for transparent monitoring of optical signal-to-noise ratio degradation in optical transmission system," *J. Lightwave Technol.*, vol. 20, no. 8, pp. 1367–1373, August 2002.
- [91] C. Schmidt, C. Schubert, J. Berger, M. Kroh, H. Ehrke, E. Dietrich, C. Börner, R. Luwig, H. Weber, F. Futami, S. Watanabe, and T. Yamamoto, "Optical q-factor monitoring at 160 gb/s using an optical sampling system in an 80 km transmission experiment," in *OSA Trends in Optics and Photonics (TOPS) Vol. 73, Conference on Lasers and Electro-Optics, OSA Technical Digest, Postconference Edition*. Washington DC: Optical Society of America, 2002, pp. 579–580.
- [92] R. Essiambre, B. Mikkelsen, and G. Raybon, "Intra-channel cross-phase modulation and four-wave mixing in high-speed TDM systems," *Electron. Lett.*, vol. 35, no. 18, pp. 1576–1578, 1999.
- [93] P. Mamyshev and N. Maysheva, "Pulse-overlapped dispersion-managed data transmission and intrachannel four-wave mixing," *Opt. Lett.*, vol. 24, no. 21, pp. 1454–1456, 1999.
- [94] P. Johannisson, D. Anderson, A. Berntson, and J. Mårtensson, "Generation and dynamics of ghost pulses in strongly dispersion-managed fiber-optic communication systems," *Opt. Lett.*, vol. 26, no. 16, pp. 1227–1229, 2001.
- [95] A. Mecozzi, C. Clausen, and M. Shtaif, "Analysis of intrachannel nonlinear effects in highly dispersed optical pulse transmission," *IEEE Photon. Technol. Lett.*, vol. 12, no. 4, pp. 392–394, 2000.
- [96] R. Killey, V. Mikhailov, S. Appathurai, and P. Bayvel, "Investigation of nonlinear distortion in 40-Gb/s transmission with higher order mode fiber dispersion compensators," *J. Lightwave Technol.*, vol. 20, no. 12, pp. 2282–2289, 2002.
- [97] I. Shake, H. Takara, K. Uchiyama, and Y. Yamabayashi, "Quality monitoring of optical signals influenced by chromatic dispersion in a transmission fiber using averaged Q-factor evaluation," *IEEE Photon. Technol. Lett.*, vol. 13, no. 4, pp. 385–387, April 2001.
- [98] E. Hellström, H. Sunnerud, M. Westlund, and M. Karlsson, "Third-order dispersion compensation using a phase modulator," *J. Lightwave Technol.*, vol. 21, no. 5, pp. 1188–1197, May 2003.



# Appendix A

## A.1 Set-up of the Optical Transmitter

This section describes the experimental set-up of the optical transmitter that was used in all experiments. The schematic set-up is shown in Fig.A.1.

In order to generate the high bit rate data signals, 1.5 ps optical pulses were generated using a tunable mode-locked semiconductor laser (TMLL) [61]. The laser was operated at a repetition rate of 9.953 28 GHz, which was generated using a fixed frequency oscillator (OSC) with low phase noise. The electrical signal from the oscillator was also used to drive a pulse pattern generator (PPG). The PPG generated a 10 Gbit/s pseudo random bit sequence (PRBS) with a word length of  $2^7 - 1$  which was encoded to the optical pulses from the TMLL using a Lithiumniobate Mach-Zehnder modulator (MOD). The optical signal was amplified before and after the modulator by Erbium doped amplifiers (EDFA).

The optical 10 Gbit/s data signal was multiplexed to 160 Gbit/s using a passive fiber delay line multiplexer. The multiplexer consisted of four stages, in which the optical signal was split, delayed in the lower branch and recombined again. The delay  $\Delta t$  in each stage was chosen as

$$\Delta t = \frac{2^7 - 1}{2} \cdot T_{Bit,in} \quad (\text{A.1})$$

Here,  $T_{Bit,in}$  is the bit spacing at the input of the stage. Thus, the bit rate of the data signal was doubled by each stage while maintaining its PRBS nature for word length of  $2^7 - 1$ . A beam shutter was placed in the upper branch of each stage in order to select the desired output branch. Each shutter also included a polarization controller

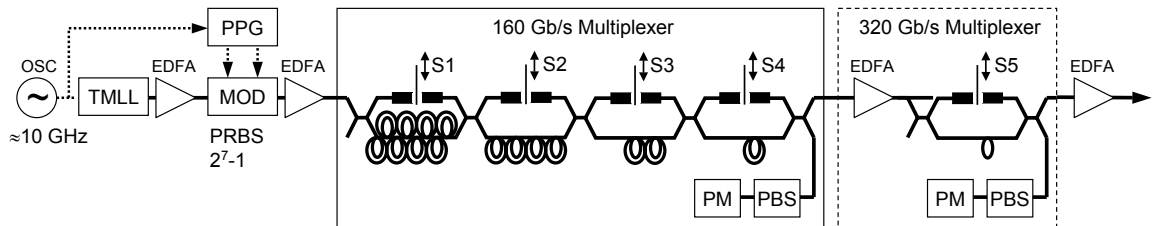


Figure A.1: Schematic set-up of the 320 Gbit/s data transmitter.

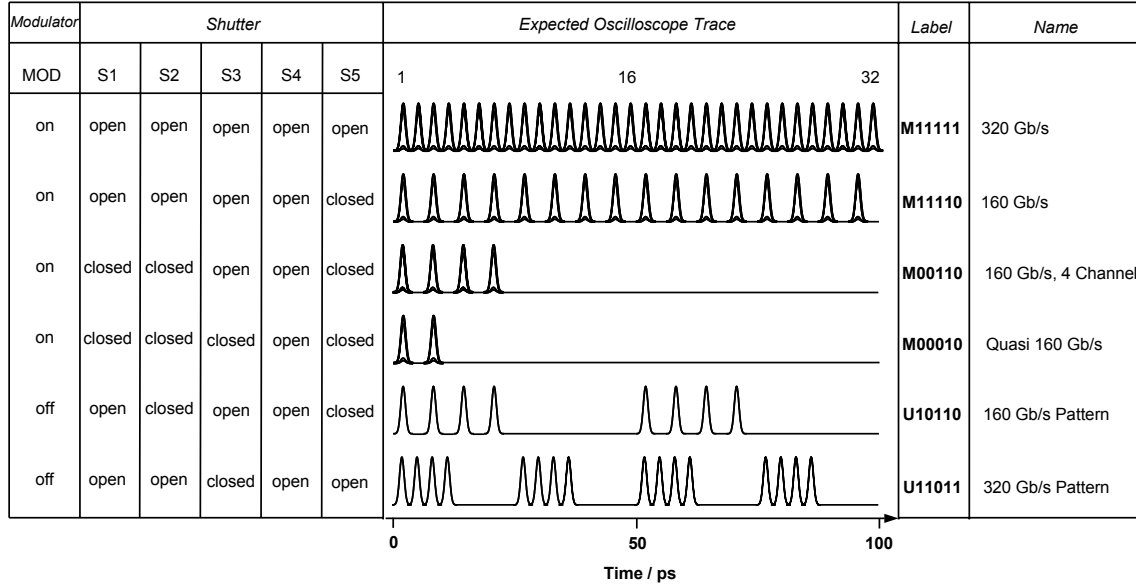


Figure A.2: Examples of expected oscilloscope traces for various transmitter settings together with corresponding labels and name definitions.

(not shown) which was used to match the output polarization of the upper branch to the output polarization of the lower branch thus ensuring a single polarization output signal. The polarization controllers were adjusted by monitoring the average output power of the multiplexer with a power meter (PM) after a polarization beam splitter (PBS) and adjusting for minimum signal on the PM. In order to balance the output amplitudes of the upper and lower branches, variable attenuators were inserted into each lower branch (not shown).

For some experiments, the 160 Gbit/s data signal was amplified and multiplexed to 320 Gbit/s in a second multiplexer consisting of only one delay stage. This multiplexer was set up and adjusted in the same way as described above.

Finally, the multiplexed output signal of the multiplexer(s) was amplified using an EDFA.

In the experiments reported in this work, the data transmitter was operated in a number of different modes. First, by turning the modulator off, the output signal became an unmodulated pulse train. Secondly, by opening and closing the beam shutters in the individual stages, different output signals could be generated. Fig. A.2 lists a few examples of transmitter settings together with the corresponding labels that were used throughout this work.

In the center of the figure, the expected oscilloscope traces of the generated signal amplitude versus time is shown. The time axes of all signals are plotted modulo 100 ps. When the modulator was turned off, each OTDM channel (1-32) was displayed as optical pulse. By blocking individual stages in the multiplexer, certain pulse patterns were generated as depicted in the two lower rows of the figure ("160 Gbit/s Pattern", "320 Gbit/s Pattern"). This was used for the waveform measurements reported in Sec. 5.1. In contrast, when the modulator was turned on, each OTDM channel was



displayed as an eye diagram as indicated in the upper rows of the figure ("320 Gbit/s", "160 Gbit/s"). Again, by blocking individual stages of the multiplexer, certain special eye patterns were generated as shown in the middle of the figure ("160 Gbit/s 4 Channel", "Quasi 160 Gbit/s"). These modes were used for all other experiments.

## A.2 Numerical Simulation of Pulse Propagation in an Optical Fiber

The analysis of the measured eye diagrams was supported by numerical simulations. In these simulations, the propagation equation for optical pulses in nonlinear and dispersive fibers was solved using a split-step Fourier algorithm. For this purpose, a simulation software was written with National Instruments' LabVIEW programming language. The implementation of the split-step Fourier algorithm is taken from [59]. The format of the simulated eye diagram was compatible to the evaluation software described in Sec. 2.4 thus making it easy to evaluate the simulated data in the same way as the experimental data. This section describes the main equations and relations that were used in the simulation software.

In order to simulate the propagation of picosecond pulses over optical single-mode fibers, it is common to start with the propagation equation in the case of the slowly varying envelope (SVE) approximation. It reads as follows ( $i = \sqrt{-1}$ ):

$$\frac{\partial A}{\partial z} = -\frac{\alpha}{2}A - \frac{i\beta_2}{2}\frac{\partial^2 A}{\partial T^2} + \frac{\beta_3}{6}\frac{\partial^3 A}{\partial T^3} + i\gamma|A|^2A \quad (\text{A.2})$$

Here,  $A = A(z, T)$  is the slowly varying complex envelope of the electrical field with  $z$  being the spatial coordinate along the fiber and  $T$  being the time in a reference frame moving with the pulse at its group velocity  $v_g$ :

$$T = t - \frac{z}{v_g} \quad (\text{A.3})$$

The complex field envelope  $A(z, T)$  is normalized such that

$$P = |A|^2 \quad (\text{A.4})$$

where  $P$  is the optical power of the signal.

In Eq. (A.2),  $\alpha$  is the absorption coefficient and is given in units of  $m^{-1}$ .  $\beta_2$  and  $\beta_3$  account for dispersion and third order dispersion and are given in units of  $s^2/m$  and  $s^3/m$ , respectively. Higher order dispersion terms are neglected.  $\gamma$  is the nonlinearity coefficient of the fiber and is given in units of  $W^{-1} km^{-1}$ .

Eq. (A.2) describes the pulse propagation of pulses which have a width of more than a few hundred femtoseconds and includes absorption, dispersion and fiber nonlinearity. It does not include polarization effects.

Introducing two operators  $\hat{D}$  and  $\hat{N}$  the propagation equation can be formally rewritten as

$$\frac{\partial A}{\partial z} = (\hat{D} + \hat{N}) A \quad (\text{A.5})$$

with

$$\hat{D} = -\frac{\alpha}{2} - \frac{i\beta_2}{2} \frac{\partial^2}{\partial T^2} + \frac{\beta_3}{6} \frac{\partial^3}{\partial T^3} \quad (\text{A.6})$$

$$\hat{N} = i\gamma|A|^2 \quad (\text{A.7})$$

Thus the differential operator  $\hat{D}$  contains the terms that relate to dispersion and absorption while the nonlinear operator  $\hat{N}$  accounts for the fiber nonlinearity.

In general, dispersion and nonlinearity act together along the length of the fiber. The idea behind the split-step Fourier method is to obtain an approximate solution of the propagation equation over the distance  $L$  by assuming that in propagating the field over a small distance  $h$ , the dispersive and nonlinear effects can be pretended to act independently. In particular, in the symmetrized split-step method, this means that the propagation of the optical field from  $z$  to  $z+h$  was carried out in three steps. First, the nonlinearity was disregarded and the optical field was propagated over half the distance  $h/2$ . Then the nonlinearity was pretended to act alone at the middle of the segment  $h$  and finally the optical field was propagated over the second half of the segment again disregarding the nonlinearity. Mathematically, this means

$$A(z+h, T) \approx \exp\left(\frac{h}{2}\hat{D}\right) \exp\left(\int_z^{z+h} \hat{N}(z')dz'\right) \exp\left(\frac{h}{2}\hat{D}\right) A(z, T) \quad (\text{A.8})$$

Please note that the integral over the nonlinear operator in Eq. (A.8) ranges from  $z$  to  $z+h$ . This means that the nonlinear effects of the whole segment length  $h$  are applied at the middle of the segment.

To solve Eq. (A.8), it is useful to perform the dispersive propagation in the frequency domain. The dispersive operator  $\hat{D}$  in the frequency domain becomes

$$\hat{D}(i\omega) = -\frac{\alpha}{2} + \frac{i\beta_2\omega^2}{2} - \frac{i\beta_3\omega^3}{6} \quad (\text{A.9})$$

with

$$\omega = 2\pi\nu \quad (\text{A.10})$$

The advantage of using the dispersive operator in the frequency domain is that it does not contain any differentiation but is simply a number. Thus it is straightforward to calculate the complex field after half the segment length using the Fourier transform  $\mathcal{F}[\cdot]$  and its inverse:

$$A(z + \frac{h}{2}, T) = \mathcal{F}^{-1} \left[ \exp\left(\frac{h}{2}\hat{D}(i\omega)\right) \mathcal{F}[A(z, T)] \right] \quad (\text{A.11})$$

Then the nonlinearity was calculated in the time domain by approximating the integral over the nonlinear operator following the trapezoidal rule:

$$\int_z^{z+h} \hat{N}(z') dz' \approx \frac{h}{2} [\hat{N}(z) + \hat{N}(z+h)] \quad (\text{A.12})$$

The issue in solving Eq. (A.12) is that in order to know the nonlinear operator at the end of the segment  $\hat{N}(z+h)$ , also the optical field  $A(z+h, T)$  at the end of the segment needs to be known. However,  $A(z+h, T)$  is not yet known at the midpoint  $z+h/2$  of the segment, since the field has not yet propagated the whole segment. Therefore, an iterative procedure has to be used. First,  $\hat{N}(z+h)$  in Eq. (A.12) is replaced by  $\hat{N}(z+h/2)$  and Eq. (A.8) is used to calculate a first estimate of the optical field  $A(z+h, T)$ . This is then in turn used to calculate a new value of  $\hat{N}(z+h)$  which is now used in Eq. (A.12). This iteration was rather time consuming but converged rather quickly, so that two iteration steps were enough to reach sufficient accuracy in the simulation.

This way, the propagation of the optical field was calculated for each segment  $h$  of the whole propagation distance  $L$ .

### Data Signal

As the data signal was composed of secant hyperbolic shaped optical pulses, the complex field envelope at the input of the fiber link was described by

$$A(0, T) = \sum_i A_i \operatorname{sech} \left( \frac{T - T_i}{T_0} \right) \exp \left( i \left[ \phi_i - \frac{C(T - T_i)^2}{2T_0^2} \right] \right) \quad (\text{A.13})$$

where  $C$  is the chirp parameter and  $T_0$  is the  $1/e$ -width of the pulse, which is related to its full width at half maximum (FWHM) by

$$\text{FWHM} = 1.763 T_0 \quad (\text{A.14})$$

Eq. (A.13) describes the data signal as the superposition of a number of pulses with secant hyperbolic shapes having the field amplitudes  $A_i$  and the temporal locations  $T_i$ . Since in the experiments the data signal was generated by the modulation of a pulse train with a Lithiumniobate amplitude modulator, the extinction of the data signal was limited to  $\sim 15$  dB. This was accounted for in the simulation by setting the power of space level pulses to be  $1/31$  of the mark level pulses.

The parameter  $\phi_i$  describes the optical phase offset of the individual pulses. This parameter is the same for all data pulses in one OTDM-channel but is in general different between the individual OTDM-channels. If for example a 2-channel 160 Gbit/s OTDM data signal is considered (transmitter set to "M00010" generating an eye diagram with two adjacent eyes), all pulses in the left channel have the same phase offset  $\phi^{\text{left}}$  while all the pulses in the right channel have another phase offset  $\phi^{\text{right}}$ . The difference between these two phase offsets is called relative optical phase  $\Delta\phi$ .

Please note that in the experiments a passive fiber delay line multiplexer was used to generate the 160 Gbit/s data signal. The fiber delays in this multiplexer were not stabilized in phase and thus the relative optical phase between the individual OTDM-channels was slowly drifting with time due to temperature changes. Therefore, the

relative optical phase was fixed for one single eye diagram measurement (which was taken within a few milliseconds) but was changing from measurement to measurement. This effect was accounted for in the simulations by keeping the relative optical phase a variable parameter.

### Fiber Parameters

Following Eq. (A.2), the optical fiber is described by the four parameters  $\alpha$ ,  $\beta_2$ ,  $\beta_3$  and  $\gamma$ . However, fiber manufacturers usually specify the properties of a fiber using the dispersion parameter  $D$  in [ps/(nm km)], dispersion slope  $S$  in [ps/(nm<sup>2</sup> km)] and loss  $\alpha_{dB}$  in [dB/km]. The following equations summarize the relation between these parameters.

$$\beta_2 = -\frac{\lambda^2}{2\pi c} D \quad (\text{A.15})$$

$$\beta_3 = \left(\frac{\lambda^2}{2\pi c}\right)^2 \left(S - \frac{4\pi c}{\lambda^3} \beta_2\right) \quad (\text{A.16})$$

$$\alpha_{dB} = 10 \log(e^\alpha) \quad (\text{A.17})$$

$$\alpha = \alpha_{dB}/4.343 \quad (\text{A.18})$$

# Appendix B

## List of Symbols and Abbreviations

### Mathematical Symbols

$*$	convolution
$\mathcal{F}[\cdot]$	Fourier transform
$\mathcal{F}^{-1}[\cdot]$	inverse Fourier transform

### Roman Symbols

$A$	normalized signal amplitude $[\sqrt{W}]$
$A^{el}(\tau)$	amplitude of sample in electrical sampling [-]
$A^{opt}(\tau)$	amplitude of sample in optical sampling [-]
$A_{1/2}$	half of peak amplitude [-]
$A_{base}$	baseline amplitude [-]
$A_{eff}$	effective area of the fiber [m <sup>2</sup> ]
$A_{min/max}$	minimum/maximum signal amplitude [-]
$A_{peak}$	peak amplitude [-]
$A_{split}$	split amplitude between mark and space region [-]
$A_c$	split amplitude of vertical histogram [-]
$A_i$	amplitude of $i$ -th pulse in simulated pulse train [-]
$\bar{A}_{mark/space}(n)$	mean amplitude in $n$ -th time interval in mark/space region [-]
$AN$	amplitude noise [-]
$B$	optical bandwidth of sampling system [Hz]
$BER$	bit error ratio [-]
$C$	chirp parameter [-]
$d$	number of sub-rate channels in a multiplexed data signal [-]
$D$	dispersion of the fiber [s/m <sup>2</sup> ]
$D_{res}$	dispersion of the fiber [s/m]
$\hat{D}$	dispersion operator in the time domain [1/m]
$\hat{\hat{D}}$	dispersion operator in the frequency domain [1/m]
$E(t)$	complex electrical field as a function of time [V/m]
$E^{G,opt}(t - \tau)$	gated electrical field in optical sampling [V/m]
$EO$	eye opening [-]
$EOP$	eye opening penalty [dB]

$ER$	extinction ratio [dB]
$F'(t)$	overall time domain filter function of electrical sampling [-]
$F^{el}(t)$	time domain filter function of low pass filter in electrical sampling [-]
$f_{a/b}$	integration limits in phase noise measurement [Hz]
$f_{A/D-Clock}$	clock frequency of the A/D converter [Hz]
$f_{A/D-Trigger}$	trigger frequency of the A/D converter [Hz]
$f_{clock}$	extracted clock frequency [Hz]
$f_{Laser}$	repetition frequency of the laser inside the sampling pulse source [Hz]
$f_{MOD}$	repetition frequency of the modulator inside the sampling pulse source [Hz]
$f_c, f_0$	RF carrier frequency [Hz]
$f_G$	gating frequency [Hz]
$f_m$	frequency offset from the RF carrier [Hz]
$f_S$	repetition frequency of the data signal [Hz]
$G^{el}(t - \tau)$	time domain gating function of electrical sampling gate [-]
$G^{opt}(t - \tau)$	time domain gating function of optical sampling gate [-]
$h$	segment length in split step Fourier algorithm [m]
$H^{el}(t)$	time domain filter function of low pass filter in optical sampling [-]
$\underline{H}$	eye diagram matrix containing frequencies of occurrence [-]
$\underline{H}_{mark/space}$	matrix containing frequencies of occurrence in mark/space region [-]
$h_{mn}$	number of times by which measured data points fell into m-th amplitude interval and n-th time interval [-]
$H_{(n)}$	horizontal histogram [-]
$h_n$	n-th element of horizontal histogram [-]
$i$	index [-]
$k$	number of samples [-]
$k'$	number of samples with reduced sampling rate [-]
$\ell$	geometrical length of the refractive medium [m]
$\ell_{opt}$	optical path length in the interferometer branch [m]
$L$	length of the fiber [m]
$L(f_m)$	single side band phase noise [dBc/Hz]
$L_{SMF}$	length of SMF inserted for fine tuning of the dispersion compensation [m]
$L_0$	fiber length required for 100 % dispersion compensation [m]
$m$	running index, integer number [-]
$M$	number of amplitude intervals in eye diagram [-]
$M$	reduction factor of sampling pulses [-]
$m_{low/high}$	index of the lowest/highest amplitude level in the horizontal histogram [-]
$m_{split}$	split index between mark and space region [-]
$n$	running index, integer number [-]
$n$	refractive index of the material [-]
$N$	number of temporal intervals in eye diagram [-]
$N$	stretch factor of the sampled image [-]
$\hat{N}$	nonlinearity operator in the time domain [1/m]
$n_c$	split index of horizontal histogram [-]
$P(t)$	optical power as a function of time [W]
$P_{in}$	optical peak power of the pulses at the input of the fiber link [W]
$P_{in}(t)$	optical power at the input of the interferometer [W]

$P_{out}(t)$	optical power at the output of the interferometer [W]
$\bar{P}_{out}(t)$	optical power at the complementary output of the interferometer [W]
$P_{rec}$	received average optical power [dBm]
$P_S$	average optical power of the sampling pulses [W]
$Q$	Q-factor [-]
$Q_{BER}$	Q-factor calculated from measured bit error ratio [-]
$Q_{Eye}$	Q-factor derived from eye diagram [-]
$R$	bit rate [1/s]
$S$	dispersion slope of the fiber [s/m <sup>3</sup> ]
$S_{res}$	residual dispersion slope of the fiber [s/m <sup>2</sup> ]
$S^{D,el}(t)$	detected signal amplitude in electrical sampling [-]
$S^{D,opt}(t - \tau)$	detected signal amplitude in optical sampling [-]
$S^{F,el}(t)$	filtered signal amplitude in electrical sampling [-]
$S^{G,el}(t - \tau)$	gated signal amplitude in electrical sampling [-]
$S^{H,opt}(t - \tau)$	filtered signal amplitude in optical sampling [-]
$T$	retarded time in the numerical simulation [s]
$t$	retarded time [s]
$T(t)$	transmittance of the sampling gate [-]
$T_\Delta$	period of the sampled image [s]
$t_{1/2,left/right}$	temporal position of half peak amplitude at the left/right flank [s]
$T_{bit}$	duration of one bit slot [s]
$t_{min/max}$	minimum/maximum time in eye diagram [s]
$t_{peak}$	temporal position of peak amplitude [s]
$T_0$	1/e-width of pulses in simulated pulse train [s]
$t_c$	time corresponding to split index of horizontal histogram [s]
$T_G$	period of the gating function [s]
$T_i$	temporal position of $i$ -th pulse in simulated pulse train [s]
$T_S$	period of the data signal [s]
$v_g$	group velocity [m/s]
$V_p$	peak voltage of the electrical sample [V]
$V_{(m)}$	vertical histogram [-]
$v_m$	$m$ -th element of horizontal histogram [-]
$z$	spatial coordinate along the fiber in the simulation [m]

### Greek Symbols

$\alpha$	absorption coefficient of the fiber in the simulation [1/m]
$\beta_2$	dispersion coefficient of the fiber in the simulation [s <sup>2</sup> /m]
$\beta_3$	third order dispersion coefficient of the fiber in the simulation [s <sup>3</sup> /m]
$\delta\nu$	spectral width (FWHM) of optical pulse [Hz]
$\Delta\Phi(t)$	optical phase change in the nonlinear element [rad]
$\Delta\phi$	relative optical phase between adjacent OTDM-channels [rad]
$\Delta\Phi_{1,2}(t)$	optical phase change in branch 1/2 of the interferometer [rad]
$\Delta\Phi_{max}$	maximum induced phase change in the nonlinear element [rad]
$\Delta\tau$	time step between the samples [s]
$\Delta\tau'$	time step between the samples with reduced sampling rate [s]

$\Delta A$	width of amplitude interval in eye diagram [-]
$\Delta f$	frequency offset between signal frequency and gating frequency [Hz]
$\Delta t$	time delay between the control pulses in the two interferometer branches [s]
$\Delta t$	width of temporal interval in eye diagram [s]
$\eta'$	conversion factor [1/W]
$\eta$	conversion factor [V <sup>2</sup> /(W m <sup>2</sup> )]
$\gamma$	nonlinearity coefficient of the fiber [1/(W m)]
$\mu_{0/1}$	mean amplitude of space/mark level [-]
$\nu$	optical frequency of the optical pulse [Hz]
$\omega$	optical (angular) frequency [rad/s]
$\omega_0$	optical (angular) frequency of the optical pulse [rad/s]
$\phi(t)$	optical phase of the optical pulse as a function of time [rad]
$\phi^{left/right}$	optical phase of left/right pulse in simulated 2-channel pulse train [rad]
$\phi_i$	optical phase of $i$ -th pulse in simulated pulse train [rad]
$\tau$	temporal width (FWHM) of optical pulse [s]
$\tau_{Eye}$	width (FWHM) of eye diagram [s]
$\tau_{GW,GT-UNI}$	width (FWHM) of gating window of GT-UNI sampling gate [s]
$\tau_{GW,Kerr}$	width (FWHM) of gating window of Kerr sampling gate [s]
$\tau_{GW,NOLM}$	width (FWHM) of gating window of NOLM sampling gate [s]
$\tau_{GW}$	width (FWHM) of gating window [s]
$\tau_{data}$	width (FWHM) of the optical pulses in the data signal [s]
$\tau_{meas}$	measured width (FWHM) [s]
$\tau_{probe}$	width (FWHM) of probe pulses [s]
$\tau_{RMS}$	root mean square value of timing jitter [s]
$\tau_{SP}$	width (FWHM) of sampling pulse [s]
$\varphi_{RMS}$	root mean square value of timing jitter [rad]
$\xi$	conversion factor [m <sup>2</sup> /V <sup>2</sup> ]

## Abbreviations

APD	avalanche photodiode
AKF	autocorrelation function
AM	amplitude modulation
AR	anti reflection
ASE	amplified spontaneous emission
ATT	attenuator
BER	bit error ratio
BERT	bit error ratio test set
C-band	central wavelength band (1525-1565 nm)
CE	clock extraction
CIRC	circulator
CS-SSB-AM	carrier-suppressed single sideband amplitude modulation
cw	continuous wave
DC	direct current
DCF	dispersion compensating fiber
DFB	distributed feedback



---

DFG	difference frequency generation
DGD	differential group delay
EAM	electroabsorption modulator
EDFA	Erbium doped fiber amplifier
EDFL	Erbium doped fiber laser
FILT	optical filter
FL	fiber laser
FWHM	full width at half maximum
FWM	four-wave mixing
GT	gain-transparent
GT-UNI	gain-transparent ultrafast nonlinear interferometer
GW	gating window
HBT	hetero bipolar transistor
HNLF	highly nonlinear fiber
IFWM	intra-channel four-wave mixing
IXPM	intra-channel cross-phase modulation
L-band	long wavelength band (1568-1610 nm)
LiNbO <sub>3</sub>	Lithiumniobate
ML EDFL	mode locked Erbium doped fiber laser
MLLD	mode locked laser diode
MMIC	monolithic microwave integrated circuit
MSSL	mode locked solid state laser
MZI	Mach-Zehnder interferometer
NOLM	nonlinear optical loop mirror
NRZ	non return-to-zero
NZDSF	non-zero dispersion shifted fiber
O/E	opto/electrical
OD	optical delay line
OSA	optical spectrum analyzer
OTDM	optical time division multiplexing
PBS	polarization beam splitter
PC	polarization controller
PD	photodetector
PLL	phase locked loop
PMD	polarization mode dispersion
PMF	polarization maintaining fiber
POL	polarizer
PPLN	periodically poled Lithiumniobate
PRBS	pseudo random binary sequence
RF	radio frequency
RMS	root-mean square
RZ	return-to-zero
S-band	short wavelength band (1450-1530 nm)
SFG	sum frequency generation
SHG	second-harmonic generation
SLALOM	semiconductor amplifier in a loop mirror

SMF	standard single mode fiber
SNR	signal-to-noise ratio
SOA	semiconductor optical amplifier
SPM	self-phase modulation
SSB	single side band
SVE	slowly varying envelope
TDM	time division multiplexing
TMLL	tunable mode locked laser
UNI	ultrafast nonlinear interferometer
VCO	voltage controlled oscillator
WDM	wavelength division multiplexing
XPM	cross-phase modulation

# Appendix C

## Publications by the Author

### First author papers

1. C. Schmidt, S. Diez, R. Ludwig, and H. G. Weber. Picosecond pulse train switching by four-wave mixing in semiconductor-laser amplifiers. In *Photonics in Switching '97, OSA Technical Digest Series*, volume 10, pages 197–200, Stockholm, Sweden, 1997.
2. C. Schmidt, S. Diez, R. Ludwig, and H. G. Weber. Switching window of picosecond pulse switching using four-wave mixing in semiconductor-optical amplifiers. In *Optical Amplifiers and their Applications, OAA '97, Technical Digest*, pages 220–223, Victoria B.C., Canada, 1997.
3. C. Schmidt, E. Dietrich, S. Diez, H. J. Ehrke, U. Feiste, L. Küller, R. Ludwig, and H. G. Weber. Mode-locked semiconductor lasers and their applications for optical signal processing. In *Conf. on Lasers and Electro-Optics (CLEO) Tech. Dig.*, pages 348–349, May 1999. paper CThA3-invited.
4. C. Schmidt, F. Futami, S. Watanabe, T. Yamamoto, C. Schubert, J. Berger, M. Kroh, H.-J. Ehrke, E. Dietrich, C. Börner, R. Ludwig, and H. G. Weber. Complete optical sampling system with broad gap-free spectral range for 160 Gbit/s and 320 Gbit/s and its application in a transmission system. In *Opt. Fiber Commun. Conf. Techn. Dig.*, pages 528–530, Anaheim, USA, March 2002. paper ThU1.
5. C. Schmidt, C. Schubert, J. Berger, M. Kroh, H.-J. Ehrke, E. Dietrich, C. Börner, R. Ludwig, H.G. Weber, F. Futami, S. Watanabe, and T. Yamamoto. Optical Q-factor monitoring at 160 Gb/s using an optical sampling system in an 80 km transmission experiment. In *OSA Trends in Optics and Photonics (TOPS) Vol. 73, Conference on Lasers and Electro-Optics, OSA Technical Digest, Postconference Edition*, pages 579–580, Washington DC, 2002. Optical Society of America.
6. C. Schmidt, C. Schubert, S. Watanabe, F. Futami, R. Ludwig, and H.G. Weber. 320 Gb/s all-optical eye diagram sampling using gain-transparent ultrafast nonlinear interferometer (GT-UNI). In *Proc. 28th Eur. Conf. on Opt. Comm. (ECOC'02)*, Copenhagen, Denmark, 2002. paper 2.1.3.
7. C. Schmidt, C. Schubert, C. Börner, C.M. Weinert, H. Bülow, E. Lach, and H.G. Weber. Investigation of intra-channel four-wave mixing at 160 Gb/s using an optical sampling system. In *Proc. 29th Eur. Conf. on Opt. Comm. (ECOC'03)*, Rimini, Italy, September 21–25 2003. paper Th2.5.2.

### Other full papers and letters

1. K. Obermann, S. Kindt, D. Breuer, K. Petermann, C. Schmidt, S. Diez, and H. G. Weber. Noise characteristics of semiconductor-optical amplifiers used for wavelength conversion via cross-gain and cross-phase modulation. *Photon. Technol. Lett.*, 9:312–314, 1997.

2. S. Diez, C. Schmidt, R. Ludwig, H. G. Weber, K. Obermann, S. Kindt, I. Koltchanov, and K. Petermann. Four-wave mixing in semiconductor optical amplifiers for frequency conversion and fast optical switching. *IEEE J. Sel. Topics Quant. Electron., Nonlinear Devices for All-Optical Signal Processing*, 3(5):1131–1145, 1997. (invited).
3. S. Diez, C. Schmidt, R. Ludwig, H. G. Weber, P. Doussi re, and T. Ducellier. Effect of birefringence in a bulk semiconductor optical amplifier on four-wave mixing. *IEEE Photon. Technol. Lett.*, 10(2):212–214, February 1998.
4. S. Diez, C. Schmidt, D. Hoffmann, C. Bornholdt, B. Sartorius, H. G. Weber, L. Jiang, and A. Krotkus. Simultaneous sampling of optical pulse intensities and wavelengths by four-wave mixing in a semiconductor-optical amplifier. *Appl. Phys. Lett.*, 73(26):3821–3823, 28th December 1998.
5. U. Feiste, R. Ludwig, C. Schmidt, E. Dietrich, S. Diez, H.-J. Ehrke, E. Patzak, H. G. Weber, and T. Merker. 80-Gb/s transmission over 106-km standard-fiber using optical phase conjugation in a sagnac-interferometer. *IEEE Photon. Technol. Lett.*, 11(8):1063–1065, August 1999.
6. S. Diez, R. Ludwig, C. Schmidt, U. Feiste, and H.G. Weber. 160-Gb/s optical sampling by gain-transparent four-wave mixing in a semiconductor optical amplifier. *IEEE Photon. Technol. Lett.*, 11(11):1402–1404, November 1999.
7. U. Feiste, R. Ludwig, S. Diez, C. Schmidt, H.J. Ehrke, H.G. Weber, and F. K ppers. Unrepeated 80 Gbit/s RZ single channel transmission over 160 km of standard fibre at 1.55  $\mu\text{m}$  with large wavelength tolerance. *Electron. Lett.*, 36(6):561–563, 2000.
8. S. Diez, C. Schubert, R. Ludwig, H.-J. Ehrke, U. Feiste, C. Schmidt, and H. G. Weber. 160 Gbit/s all-optical demultiplexer using hybrid gain-transparent SOA Mach-Zehnder interferometer. *Electron. Lett.*, 36(17):1484–1486, August 2000.
9. R. Ludwig, U. Feiste, S. Diez, C. Schubert, C. Schmidt, H. J. Ehrke, and H. G. Weber. Unrepeated 160 Gbit/s RZ single-channel transmission over 160 km of standard fiber at 1.55  $\mu\text{m}$  with hybrid MZI optical demultiplexer. *Electron. Lett.*, 36(16):1405–1406, July 2000.
10. G. Toptchiyski, S. Randel, K. Petermann, S. Diez, E. Hilliger, C. Schmidt, C. Schubert, R. Ludwig, and H. G. Weber. Analysis of switching windows in a gain-transparent-SLALOM configuration. *J. Lightwave Technol.*, pages 2188–2195, Oktober 2000.
11. L. A. Jiang, E. P. Ippen, U. Feiste, S. Diez, E. Hilliger, C. Schmidt, and H. G. Weber. Sampling pulses with semiconductor optical amplifiers. *IEEE J. Quantum Electron.*, 37(1):118–126, January 2001.
12. S. Diez, E. Hilliger, M. Kroh, C. Schmidt, C. Schubert, H. G. Weber, L. Occhi, L. Schares, G. Guekos, and L. K. Oxenl we. Optimization of SOA-based Sagnac-Interferometer switches for demultiplexing to 10 and 40 Gb/s. *Opt. Commun.*, 189:241–249, March 2001.
13. U. Feiste, R. Ludwig, C. Schubert, J. Berger, C. Schmidt, H. G. Weber, A. Munk, B. Schmauss, B. Buchhold, D. Briggmann, F. Kueppers, and F. Rumpf. 160 Gbit/s transmission over 116 km field-installed fiber using 160 Gbit/s OTDM and 40 Gbit/s ETDM. *Electron. Lett.*, 37(7):443–445, March 2001.
14. T. Yamamoto, L. K. Oxenl we, C. Schmidt, C. Schubert, E. Hilliger, U. Feiste, J. Berger, R. Ludwig, and H. G. Weber. Clock recovery from 160 Gbit/s data signals using phase-locked loop with interferometric optical switch based on semiconductor optical amplifier. *Electron. Lett.*, 37(8):509–510, April 2001.
15. M. Gunkel, F. K ppers, J. Berger, U. Feiste, R. Ludwig, C. Schubert, C. Schmidt, and H. G. Weber. Unrepeated 40 Gbit/s RZ transmission over 252 km SMF using Raman amplification. *Electron. Lett.*, 37(10):646–648, 10 May 2001.

16. C.M. Weinert, J. Berger, U. Feiste, E. Hilliger, B. Konrad, M. Kroh, R. Ludwig, K. Petermann, C. Schmidt, C. Schubert, H.G. Weber, and T. Yamamoto. High bit rate OTDM-transmission on standard fibre. *Int. J. Electron. Commun. (AEÜ)*, 55(5):349–353, 2001.
17. U. Feiste, R. Ludwig, C. Schubert, J. Berger, C. Schmidt, H. G. Weber, B. Schmauss, A. Munk, B. Buchhold, D. Briggmann, F. Kueppers, and F. Rumpf. 160 Gbit/s field transmission over 116 km standard single mode fibre using 160 Gbit/s OTDM and 40 Gbit/s ETDM demultiplexer. *Proc.-Optoelectron.*, 148(4):171–175, August 2001.
18. C. Schubert, J. Berger, U. Feiste, R. Ludwig, C. Schmidt, and H. G. Weber. 160 Gb/s polarization insensitive all-optical demultiplexing using a gain-transparent Ultrafast-Nonlinear Interferometer (GT-UNI). *IEEE Photon. Technol. Lett.*, 13(11):1200–1202, November 2001.
19. C. Schubert, J. Berger, S. Diez, H. J. Ehrke, R. Ludwig, U. Feiste, C. Schmidt, H. G. Weber, G. Toptchiyski, S. Randel, and K. Petermann. Comparison of interferometric all-optical switches for demultiplexing applications in high-speed OTDM systems. *J. Lightwave Technol.*, 20(4):618–624, April 2002.
20. C. Schubert, R. Ludwig, S. Watanabe, F. Futami, C. Schmidt, J. Berger, C. Boerner, S. Ferber, and H.G. Weber. 160 Gbit/s wavelength converter with 3R-regenerating capability. *Electron. Lett.*, 38(16):903–904, 1st August 2002.
21. C. Boerner, C. Schubert, C. Schmidt, E. Hilliger, V. Marembert, J. Berger, S. Ferber, E. Dietrich, R. Ludwig, B. Schmauss, and H.G. Weber. 160 Gbit/s clock recovery with electro-optical PLL using a bidirectionally operated electroabsorption modulator as phase comparator. *Electron. Lett.*, 39(14):1071–1073, 10th July 2003.
22. C. Schubert, C. Schmidt, S. Ferber, R. Ludwig, and H. G. Weber. Error-free all-optical add-drop multiplexing at 160 Gbit/s. *Electron. Lett.*, 39(14):1074–1076, 10th July 2003.
23. L. Schares, C. Schubert, C. Schmidt, H. G. Weber, L. Occhi, and G. Guekos. Phase dynamics of semiconductor optical amplifiers at 10 to 40 GHz. *IEEE J. Quantum Electron.*, 39(11):1394–1408, November 2003.

### Other conference contributions

1. S. Diez, C. Schmidt, R. Ludwig, H. G. Weber, S. Kindt, K. Obermann, I. Kolchanov, K. Petermann, T. Ducellier, and P. Doussi  re. Birefringence in polarization insensitive semiconductor-optical amplifiers: Influence on four-wave mixing. In *Optical Amplifiers and their Applications, OAA '97, Technical Digest*, pages 216–219, Victoria B.C., Canada, 1997.
2. U. Feiste, R. Ludwig, C. Schmidt, E. Dietrich, S. Diez, H. J. Ehrke, E. Patzak, and H. G. Weber. 80 Gbit/s transmission over 106 km standard-fiber using optical phase conjugation in a sagnac-interferometer. In *Proc. Optical Fiber Commun.*, pages 68–70, February 1999. paper FD3.
3. S. Diez, R. Ludwig, C. Schmidt, U. Feiste, and H. G. Weber. 160 Gbit/s optical sampling by a novel ultra-broadband switch based on four-wave mixing in a semiconductor optical amplifier. In *Proc. Optical Fiber Commun.*, February 1999. postdeadline paper PD38.
4. L. Jiang, E. P. Ippen, S. Diez, E. Hilliger, C. Schmidt, and H. G. Weber. Wavelength and intensity sampling of optical signals using semiconductor optical amplifiers. In *Conf. on Lasers and Electro-Optics (CLEO) Tech. Dig.*, pages 444–445, May 1999. paper CThL6.
5. R. Ludwig, S. Diez, U. Feiste, E. Hilliger, C. Schmidt, and H. G. Weber. Applications of SOA's for optical signal processing and OTDM. In *Techn. Dig. of Optical Amplifiers and their Applications, OAA '99*, pages 124–127, Nara, Japan, June 9–11 1999. paper ThC3.
6. E. Hilliger, S. Diez, H.-J. Ehrke, R. Ludwig, C. Schmidt, H. G. Weber, and J. Y. Emery. 80 Gbit/s all-optical demultiplexing using a hybrid Mach-Zehnder Interferometer switch with gain-clamped semiconductor optical amplifiers. In *Photonics in Switching*, pages 97–99, Santa Barbara, California, July 1999.

7. U. Feiste, R. Ludwig, S. Diez, C. Schmidt, H.J. Ehrke, H.G. Weber, and F. Küppers. Unrepeated 80 Gbit/s RZ single channel transmission over 160 km of standard fiber at 1.55  $\mu\text{m}$  with a large wavelength tolerance. In *Proc. 25th Optical Fiber Commun.*, Baltimore, MD, March 7-10 2000. paper TuD5.
8. G. Toptchiyski, K. Petermann, S. Diez, E. Hilliger, C. Schmidt, R. Ludwig, and H.G. Weber. Evaluation of switching windows for fast optically-controlled SOA switches. In *Proc. 25th Optical Fiber Commun.*, Baltimore, MD, March 7-10 2000. paper ThF4.
9. S. Diez, C. Schubert, R. Ludwig, H.-J. Ehrke, U. Feiste, C. Schmidt, and H. G. Weber. 160 Gb/s all-optical demultiplexer using a hybrid gain-transparent SOA Mach-Zehnder-Interferometer. In *Techn. Dig. of Optical Amplifiers and their Applications, OAA'00*, Quebec, Canada, July 2000. paper OWB6.
10. R. Ludwig, U. Feiste, S. Diez, C. Schubert, C. Schmidt, H. J. Ehrke, and H. G. Weber. Unrepeated 160 Gbit/s RZ single channel transmission over 160 km of standard fiber at 1.55  $\mu\text{m}$  with hybrid MZI optical DEMUX. In *Proc. 26th Europ. Conf. Opt. Commun.*, Munich, Germany, September 2000. paper 6.1.3.
11. U. Feiste, R. Ludwig, C. Schubert, J. Berger, S. Diez, C. Schmidt, H. G. Weber, A. Munk, and B. Schmauss. 160 Gbit/s transmission using 160 to 40 Gbit/s OTDM and 40 to 10 Gbit/s ETDM DEMUX-techniques. In *Proc. 26th Europ. Conf. Opt. Commun.*, September 2000. postdeadline paper PD 1.10.
12. U. Feiste, R. Ludwig, C. Schubert, J. Berger, C. Schmidt, H. G. Weber, A. Munk, B. Schmauss, B. Buchhold, D. Briggmann, F. Kueppers, and F. Rumpf. 160 Gbit/s transmission over 116 km field-installed fiber using 160 Gbit/s OTDM and 40 Gbit/s ETDM. In *OSA Trends in Optics and Photonics (TOPS), Optical Fiber Communication Conference Technical Digest*, volume 54. OSA, Washington DC, 2001. paper ThF3.
13. M. Gunkel, F. Küppers, J. Berger, U. Feiste, R. Ludwig, C. Schubert, C. Schmidt, and H. G. Weber. 40 Gbit/s RZ unrepeated transmission over 252 km SMF using Raman amplification. In *OSA Trends in Optics and Photonics (TOPS) Vol. 54, Optical Fiber Commun. Conf., Technical Digest, Postconference Edition*, Anaheim, CA, March 17-22 2001. paper TuU3.
14. C. M. Weinert, C. Schmidt, and H. G. Weber. Application of asynchronous amplitude histograms for performance monitoring of RZ signals. In *OSA Trends in Optics and Photonics (TOPS) Vol. 54, Optical Fiber Commun. Conf., Technical Digest, Postconference Edition*, Anaheim, CA, 2001. paper WDD41.
15. L. K. Oxenløwe, C. Schubert, C. Schmidt, E. Hilliger, J. Berger, U. Feiste, R. Ludwig, and H. G. Weber. Optical clock recovery employing an optical PLL using cross-phase modulation in a Sagnac-interferometer. In *Conf. on Lasers and Electro-Optics (CLEO) Tech. Dig.*, Baltimore, USA, May 6-11 2001. paper CThU2.
16. H. G. Weber, R. Ludwig, U. Feiste, C. Schmidt, E. Hilliger, C. Schubert, J. Berger, M. Kroh, and T. Yamamoto. Optical signal processing for high speed communication systems. In *Proc. 10th Europ. Conf. on Integrated Optics*, April 2001.
17. T. Yamamoto, C. Schubert, C. Schmidt, L.K. Oxenløwe, U. Feiste, and H.G. Weber. A semiconductor laser amplifier in a loop mirror as a phase comparator in PLL-based clock recovery for 160 Gb/s data signals. In *Techn. Dig. of Optical Amplifiers and their Applications, OAA*, 2001. paper OTuC2.
18. C. Schubert, J. Berger, U. Feiste, R. Ludwig, C. Schmidt, and H.G. Weber. 160 Gb/s polarization insensitive all-optical demultiplexing using a gain-transparent Ultrafast-Nonlinear Interferometer (GT-UNI). In *Techn. Dig. of Optical Amplifiers and their Applications, OAA*, 2001. paper OWA4.
19. T. Yamamoto, U. Feiste, J. Berger, C. Schubert, C. Schmidt, R. Ludwig, and H. G. Weber. 160 Gbit/s demultiplexer with clock recovery using SOA-based interferometric switches and its application to 120 km fiber transmission. In *Proc. 27th Eur. Conf. on Opt. Comm. (ECOC'01)*, pages 192–193, Amsterdam, The Netherlands, Sep. 30 - Oct. 4 2001.

20. T. Yamamoto, C. Schmidt, E. Dietrich, C. Schubert, J. Berger, R. Ludwig, and H. G. Weber. 40 GHz optical clock extraction from 160 Gbit/s data signals using PLL-based clock recovery. In *Opt. Fiber Commun. Conf. Techn. Dig.*, pages 86–87, Anaheim, USA, 2002. paper TuN5.
21. R. Ludwig, U. Feiste, C. Schmidt, C. Schubert, J. Berger, E. Hilliger, M. Kroh, T. Yamamoto, C. M. Weinert, and H.G. Weber. Enabling transmission at 160 Gbit/s. In *Opt. Fiber Commun. Conf. Techn. Dig.*, pages 1–2, Anaheim, CA, USA, March 17-22 2002. paper TuA1.
22. H.G. Weber, R. Ludwig, U. Feiste, C. Schmidt, C. Schubert, J. Berger, E. Hilliger, M. Kroh, and T. Yamamoto. High-speed all-optical signal processing in optical communications systems. In *OSA Trends in Optics and Photonics (TOPS) Vol. 73, Conference on Lasers and Electro-Optics, OSA Technical Digest, Postconference Edition*, page 610, Washington DC, 2002. Optical Society of America.
23. C. Schubert, C. Schmidt, C. Börner, E. Dietrich, S. Ferber, R. Ludwig, and H. G. Weber. A gain-transparent ultrafast-nonlinear interferometer (GT-UNI) in a 160 Gb/s optical sampling system. In *Techn. Dig. of Optical Amplifiers and their Applications, OAA*, 2002. paper OTuD5.
24. R. Ludwig, C. Schmidt, C. Schubert, J. Berger, E. Hilliger, M. Kroh, V. Marembert, C. Boerner, S. Ferber, H.-J. Ehrke, and H.G. Weber. Technologies for 160 Gbit/s transmission systems. In *7th Optoelectronics and Commun. Conf. (OECC) Techn. Dig.*, pages 18–19, Yokohama (Japan), July 2002. paper 9B1-1.
25. R. Ludwig, C. Schubert, S. Watanabe, F. Futami, C. Schmidt, J. Berger, C. Boerner, S. Ferber, and H.G. Weber. 160 Gb/s 3R-regenerating wavelength converter. In *7th Optoelectronics and Commun. Conf. (OECC) Techn. Dig.*, July 2002. Post-Deadline Paper 1-3.
26. C. Schubert, R. Ludwig, S. Watanabe, F. Futami, S. Ferber, J. Berger, C. Schmidt, and H. G. Weber. Improved performance of a 160 Gb/s fibre based all-optical switch using rectangular gating pulses. In *Proc. 28th Eur. Conf. on Opt. Comm. (ECOC'02)*, Copenhagen, Denmark, 2002. Paper 8.3.7.
27. H. G. Weber, R. Ludwig, C. Schmidt, C. Schubert, J. Berger, E. Hilliger, M. Kroh, V. Marembert, C. Boerner, S. Ferber, and H.J. Ehrke. 160 Gbit/s TDM-transmission technology. In *Proc. 28th Eur. Conf. on Opt. Comm. (ECOC'02)*, 2002. invited paper 2.1.1.
28. C. Boerner, C. Schubert, C. Schmidt, E. Hilliger, V. Marembert, J. Berger, S. Ferber, E. Dietrich, R. Ludwig, B. Schmauss, and H. G. Weber. 160 Gbit/s clock recovery with electro-optical PLL using a bidirectionally operated electroabsorption modulator as phase comparator. In *OSA Trends in Optics and Photonics (TOPS) Vol. 56, Optical Fiber Commun. Conf., Technical Digest, Postconference Edition*, pages 670–671, Atlanta (USA), March 23-28 2003.
29. C. Schubert, C. Schmidt, S. Ferber, R. Ludwig, and H. G. Weber. Error-free all-optical add-drop multiplexing at 160 Gbit/s. In *OSA Trends in Optics and Photonics (TOPS) Vol. 56, Optical Fiber Commun. Conf., Technical Digest, Postconference Edition*, Atlanta, Georgia, USA, March 23-28 2003. postdeadline paper PD17.
30. S. Watanabe, F. Futami, R. Okabe, Y. Takita, S. Ferber, R. Ludwig, C. Schubert, C. Schmidt, and H. G. Weber. 160 Gbit/s optical 3R-regenerator in a fiber transmission experiment. In *OSA Trends in Optics and Photonics (TOPS) Vol. 56, Optical Fiber Commun. Conf., Technical Digest, Postconference Edition*, Atlanta, Georgia, USA, March 23-28 2003. postdeadline paper PD16.
31. M. Kroh, L. Küller, R. Ludwig, C. Schmidt, and H.G. Weber. Investigations on phase noise in a semiconductor mode-locked laser. In *OSA Trends in Optics and Photonics (TOPS) Vol. 86, Optical Fiber Commun. Conf., Technical Digest, Postconference Edition*, pages 673–674, Washington, DC, March 23-28 2003. Optical Society of America.

32. A. Beling, H.-G. Bach, D. Schmidt, G.G. Mekonnen, R. Ludwig, S. Ferber, C. Schubert, C. Boerner, J. Berger, C. Schmidt, U. Troppenz, and H.G. Weber. Monolithically integrated balanced photodetector and its application in OTDM 160 Gbit/s DPSK transmission. In *Integrated Photonics Research (IPR)*, Washington, DC (USA), June 16-18 2003. postdeadline paper PDP4.
33. R. Ludwig, S. Ferber, C. Schubert, C. Boerner, A. Beling, H.-G. Bach, B. Schmauss, A. Wietfeld, J. Berger, C. Schmidt, and H.G. Weber. 160 Gbit/s DPSK transmission over 410 km dispersion-managed fiber. In *8th European Conference on Networks & Optical Communications*, pages 14–19, Vienna, Austria, July 1-3 2003.
34. C. Boerner, J. Berger, S. Ferber, E. Hilliger, V. Marembert, C. Schmidt, R. Ludwig, and H.G. Weber. 160 Gb/s clock recovery and demultiplexing using one single EAM. In *Proc. 29th Eur. Conf. on Opt. Comm. (ECOC'03)*, Rimini, Italy, September 21-25 2003. paper Th2.5.1.
35. C. Schubert, L. Schares, C. Schmidt, G. Guekos, and H.G. Weber. Phase dynamics in gain-transparent semiconductor optical amplifiers. In *Proc. 29th Eur. Conf. on Opt. Comm. (ECOC'03)*, Rimini, Italy, September 21-25 2003. paper Th3.5.2.
36. S. Ferber, R. Ludwig, C. Boerner, C. Schmidt-Langhorst, L. Molle, K. Habel, M. Rohde, and H.G. Weber. 160 Gb/s regenerating conversion node. In *OSA Trends in Optics and Photonics (TOPS) Vol. 57, Optical Fiber Commun. Conf., Technical Digest, Postconference Edition*, Los Angeles (USA), February 26th 2004. paper ThT2.

## Patents

1. Ch. Börner, J. Berger, and C. Schmidt. "Optoelektrischer Phasenregelkreis zur Rückgewinnung des Taktsignals in einem digitalen optischen Übertragungssystem" (Opto-electrical phase-locked loop for clock recovery in a digital optical transmission system). *German Patent DE 103 10 015.6*, 2003.



## Appendix D

### Acknowledgements

I would like to thank Prof. Dr. Hans-Joachim Eichler from the Technical University Berlin and Prof. Dr. Hans-Georg Weber from the Fraunhofer Institute for Telecommunications, Heinrich-Hertz-Institut, for giving me the opportunity to work on the topic of this dissertation. I was fortunate to perform this work as a member of the OTDM group led by Prof. Dr. Hans-Georg Weber at the Heinrich-Hertz-Institut. Prof. Weber has been a great supporter of my work in many respects. He has always been open for discussion which I appreciate very much. His personal style has been the basis for a markedly enjoyable working atmosphere.

The results that I was able to obtain throughout the work on this thesis would not have been possible without the support of many colleagues at the Heinrich-Hertz-Institute. I would like to thank in particular the former and present colleagues in the OTDM-group, Dr. Jörn Berger, Christof Börner, Erik Dietrich, Dr. Stefan Diez (now with the MPI of Molecular Cell Biology and Genetics, Dresden), Hans-Jürgen Ehrke, Dr. Uwe Feiste (now with Infineon Technologies AG, Berlin), Sebastian Ferber, Dr. Enno Hilliger, Herbert Knupke, Marcel Kroh, Lothar Küller, Dr. Reinhold Ludwig, Vincent Marembert and Colja Schubert. They all contribute to the success of our research group and each of them made a contribution to this thesis in one way or the other. I also like to thank Dr. Carl M. Weinert for his help with the numerical simulations. The student members Javad Ghanadi, Andre Grede and Patrick Franzke helped me a great deal by contributing their expertise in RF-electronics and by setting up electronic circuits.

I am especially grateful to Colja Schubert for many long nights in the laboratory as well as countless inspiring discussions. A lot of my experience I gained from working with Dr. Reinhold Ludwig and Dr. Stefan Diez whom I thank a lot.

In the course of this thesis I was fortunate to collaborate with a number of national and international researchers who worked as visiting scientists in the OTDM-group at the Heinrich-Hertz-Institute. I recall with great pleasure the fruitful experiments and the delighting atmosphere when working with Dr. Leaf Jiang from the Massachusetts Institute of Technology (USA), Dr. Leif Oxenløwe from Research Center COM (Denmark), Tsuyoshi Yamamoto from Fujitsu Laboratories (Japan), Laurent Schares from the ETH Zürich (Switzerland), Harald Rosenfeldt from Adaptif Photonics (formerly with the Technical University Hamburg-Harburg, Germany), Dr. Fumio Futami and Dr. Shigeki Watanabe from Fujitsu Laboratories (Japan).

Furthermore, I would like to express my thanks to Colja Schubert for his careful reading of the manuscript despite being pretty busy with finishing his own thesis. I also thank Prof. Dr. Gebhard von Oppen (TU Berlin) for his willingness to chair the examination committee.

Last but not least I wish to thank my parents Gisela and Hans-Christian Schmidt for their continuous love and encouragement and my wife Tanja for her love, patience and support.

This work was kindly supported by the Deutsche Forschungsgemeinschaft (DFG).

# Appendix E

## Curriculum Vitae

### Personal Details

Name: Carsten Schmidt-Langhorst, geb. Schmidt  
 Date of birth: 7. April 1972  
 Place of birth: Berlin, Germany  
 Nationality: German  
 Marital status: married to Tanja Langhorst since 2003

### Education

08/1978 – 07/1982 Erpelgrund-Schule (elementary school), Berlin-Reinickendorf  
 08/1982 – 07/1984 Evangelische Schule Frohnau (elementary school), Berlin-Reinickendorf  
 08/1984 – 06/1991 Evangelische Schule Frohnau (high school, Gymnasium), Berlin-Reinickendorf, degree: Abitur (A-levels)  
 10/1991 – 03/1997 Study of Physics at the Technical University of Berlin, degree: Diploma, Diploma thesis: *Investigations on the nonlinear behavior of semiconductor optical amplifiers using optical picosecond pulses*, carried out in the OTDM-group at the Heinrich-Hertz-Institut für Nachrichtentechnik Berlin GmbH

### Alternative Civilian Service

05/1997 – 05/1998 University Hospital Charité, Campus Virchow, Berlin

### Professional Experience

04/1996 – 03/1997 Heinrich-Hertz-Institut für Nachrichtentechnik Berlin GmbH, student staff at the Department of Optical Signal Processing (OTDM-group), research area: *Four-wave mixing among picosecond pulses in semiconductor-optical amplifiers*  
 since 06/1998 Fraunhofer Institute for Telecommunications, Heinrich-Hertz-Institut (formerly Heinrich-Hertz-Institut für Nachrichtentechnik Berlin GmbH), scientific staff at the Department of Optical Signal Processing (OTDM-group), research area: *Ultrafast all-optical sampling*